UNIVERSIDAD DE SEVILLA

DOCTORAL THESIS

Optimization of ^{10}Be and ^{26}Al detection with low-energy accelerator mass spectrometry

Author:
Grazia Scognamiglio

Supervisors:
Dr. Elena Chamizo
Dr. José María López Gutiérrez

A thesis submitted in fulfillment of the requirements
for the degree of Doctor of Science

2017

Contents

Abstract

The Spanish Accelerator for Radionuclides Analysis (SARA) is the 1 MV AMS facility hosted at the Centro Nacional de Aceleradores (CNA, Seville, Spain). As a multi-elemental system, SARA is capable to perform measurements over a wide mass range of the nuclear chart. In order to progressively improve its overall performance, several upgrades have been carried out since it started being operative in 2006. In 2014, SARA has been equipped with He as a stripper gas, which replaced the previously installed Ar, and with a high-resolution gas ionization chamber for the rare isotopes optimized for light ions detection.

The first development opened to a variety of studies concerning the stripping process at low energies and the behaviour of different radionuclides with the new stripper. The second one improved the detection of those ions suffering of interferences (e.g. ^{10}Be, affected by the ^{10}B presence) and allowed the application of the so-called passive absorber technique, for which an optimal resolution is essential.

The different processes and parameters of merit playing a role during the measurement of light ions as ^{10}Be and ^{26}Al have been investigated. The optimization work included: (i) the analysis of the overall efficiency and the causes of beam losses, and (ii) the identification and minimization of background events.

^{10}Be AMS measurements are affected by the intense interference of its isobar ^{10}B, for which dedicated suppression techniques have to be applied. The degrader and the passive absorber methods have been tested and analyzed at the SARA system. The degrader technique consisted in placing a thin silicon nitride foil in the beam path, before the electrostatic analyzer in the high-energy side of the facility. Emerging the isobars from

the membrane with different energies, they could be spatially separated by the following energy filter. The passive absorber technique consisted in positioning an absorber cell in front of the rare isotope gas ionization chamber with a proper thickness to remove ^{10}B interference and allow ^{10}Be to enter the chamber. The degrader technique is the most conventional and effective way to measure ^{10}Be through AMS, but is characterized by severe beam losses which reduce the measurement efficiency. Passive absorbers, on the other hand, are in principle suitable at SARA's low beam energy, but just with a proper absorber design and detecting system, for which further studies are required. In both cases, the overall efficiency has been quantitatively estimated and the background sources identified.

The difficulty of ^{26}Al measurement is due to the low Al^- currents which can be extracted from the samples. A detailed study has been performed in order to identify the optimal conditions to measure ^{26}Al at the upgraded SARA facility. The passive absorber technique has been successfully applied also to remove the disturbing ^{13}C during ^{26}Al detection when the 2+ charge state after the accelerator is selected. Even if the absorber design still needs to be improved, this technique, combined with the high transmission of the 2+ charge state through the accelerator, provided an improvement for ^{26}Al measurement efficiency.

Chapter 1

Introduction

1.1 The accelerator mass spectrometry technique: overview

Radioactive nuclides are very powerful tools in many dating and tracing applications, for which it is required to know their content in a sample. Direct radioactive decay measurements might seem the obvious method to detect radionuclides, but if they have a half-life above a few hundred years and their abundance is very low, it is difficult to obtain results with low statistical errors (of about 5%) with reasonable amounts of sample.

Mass spectrometry techniques are capable to determine the isotopic composition of the elements contained in a sample by taking advantage of the dependency of the ions trajectories in magnetic and/or electrostatic fields on their mass, energy and charge state. Since it is not related to the decay activity of the material, mass spectrometry well suits for long-life radionuclides measurements and whose presence in the general environment is very scarce.

Conventional mass spectrometry is based on three phases: (i) ionization of the sample and creation of an ion beam, (ii) passage of the particles through kinematic filters and subsequent spatial separation of the beam components and (iii) detection of the species

of interest. In many cases, this kind of mass spectrometers does not have a sufficient separation capability against some interfering species to allow unambiguous nuclide detection at natural concentration levels. Atomic and molecular isobars have small mass differences and their separation with certain conventional spectrometers is feasible only if the amount of the two species is comparable. However, the interferences abundances are often excessive and impede the detection of the radionuclide of interest. So far, only accelerator mass spectrometry (AMS) can perform isotope ratio measurements at levels that are in the range of 10^{-15} to 10^{-12} relative to the major isotope in the case of rare isotopes of natural elements, and offer very competitive detection limits in the case of anthropogenic elements such as Pu isotopes. Those low detection levels can be reached by a proper suppression of isobaric ions, equal mass molecules and ions with similar kinematic properties. A recap of the radionuclides commonly measured through the AMS technique is presented in Table 1.1.

The sensitivity of AMS to measure isotopic ratios down to 10^{-15} arises from three parts: (i) extraction of negative ions from the source, (ii) stripping process in the accelerator and (iii) use of specific nuclear detectors where information about the total energy or atomic number of the ions can be obtained.

The extraction of negatively charged ions from the source provides the desired interference suppression if the disturbing isobar does not form anions. For example, the isobar ^{14}N interference during ^{14}C measurements is eliminated already in the source, as ^{14}N does not form negative ions. Sophisticated techniques based on the specific energy loss characteristics of different elements have to be applied for those nuclear pairs which form negative ions (e.g. ^{10}Be/^{10}B or ^{36}Cl/^{36}S).

AMS facilities filter molecular isobars via the so-called stripping process, consisting in the change of the charge state of the initial anions to positive ions while passing through a medium with a proper atom thickness. In this phase, molecular species are dissociated by the repulsing Coulomb force introduced between the constituents of the molecules as soon as binding electrons are stripped off. The resulting molecular fragments and the studied nuclide have mass differences large enough to be discriminated in subsequent

Table 1.1: List of the most common isotopes investigated through the AMS technique, with their half-lives and isotopic ratios in environmental samples are reported [1]. Their interferences during measurement with conventional MS are reported.

Radionuclide	Half-life (years)	Isotopic ratio	MS interferences
^{10}Be	$1.51 \cdot 10^6$	^{10}Be/^{9}Be = 10^{-11} - 10^{-5}	$^{10}B^{1+}$, $^{9}Be^{1}H^{1+}$, $^{20}Ne^{2+}$
^{14}C	5370	^{14}C/^{12}C = 10^{-14} - 10^{-11}	$^{14}N^{1+}$, $^{13}C^{1}H^{1+}$, $^{12}C^{1}H_2^{1+}$, $^{28}Si^{2+}$
^{26}Al	$7.05 \cdot 10^5$	^{26}Al/^{27}Al = 10^{-14} - 10^{-8}	$^{26}Mg^{1+}$, $^{25}Mg^{1}H^{1+}$, $^{24}Mg^{1}H_2^{1+}$
^{32}Si	172	^{32}Si/^{28}Si = 10^{-15} - 10^{-12}	$^{32}S^{1+}$, $^{31}P^{1}H^{1+}$, $^{64}Ni^{2+}$
^{36}Cl	$3 \cdot 10^5$	^{36}Cl/^{35}Cl = 10^{-15} - 10^{-8}	$^{36}Cl^{1+}$, $^{35}Cl^{1}H^{1+}$, $^{72}Ge^{2+}$
^{41}Ca	$1.03 \cdot 10^5$	^{41}Ca/^{40}Cl = 10^{-14} - 10^{-11}	$^{41}K^{1+}$, $^{40}Ca^{1}H^{1+}$, $^{82}Se^{2+}$
^{53}Mn	$1.03 \cdot 10^5$	^{41}Ca/^{40}Cl = 10^{-14} - 10^{-11}	$^{53}Cr^{1+}$, $^{52}Cr^{1}H^{1+}$, $^{106}Pd^{2+}$
^{129}I	$1.57 \cdot 10^7$	^{129}I/^{127}I = 10^{-12} - 10^{-7}	$^{129}Xe^{1+}$, $^{127}I^{1}H_2^{1+}$, $^{128}Te^{1}H^{1+}$
^{236}U	$2.34 \cdot 10^7$	^{236}U/^{238}U = 10^{-12} - 10^{-6}	$^{235}U^{1}H^{1+}$
^{239}Pu	24110	10^6 atoms	$^{238}U^{1}H^{1+}$
^{240}Pu	6564	10^6 atoms	$^{238}U^{1}H_2^{1+}$

mass and energy filters.

The last step for interference suppression in AMS takes place in the detecting system, since the high energy of the beam ions allows the use of nuclear detectors, that can distinguish between species.

From its advent about 40 years ago, the AMS made important progresses, concerning both the variety of possible applications and the measurement technique itself. The literature offers several reviews [2, 3, 4, 5, 6, 7]. However, the fundamental principles presented in 1977 [8, 9] are still the basis of state-of-the-art AMS instrumentation. Currently, three companies produce accelerator systems and components for AMS purposes: High Voltage Engineering Europe (HVEE, Amersfoort, The Netherlands), National Electrostatics Corporation (NEC, Middleton, WI, USA) and Ionplus (Ionplus AG, Zurich, Switzerland). HVEE and NEC dominated the accelerator market for the first 30 years of AMS. Ionplus was founded in 2013 as a spin-off of the Laboratory of Ion Beam Physics of the Eidgenössische Technische Hochschule Zürich (ETH, Zurich, Switzerland) and is exclusively focused on compact systems, i.e. those facilities operating at terminal voltages below 1 MV.

A brief review of the progresses of the AMS technology in the last decade will be given in the following section.

1.2 The evolution of the AMS technology: low-energy facilities

During the first 20 years of AMS, the "golden rule" of the technique was to analyze 3+ and above charge states after the stripping process, because molecules become unstable and dissociate.

In the early 1980s, experiments with radiocarbon ions showed that the intensities of molecular beams in charge states below the 3+ exponentially decrease with the stripper thickness [2]. Systematic investigations concerning the stripping processes revealed that

the cross sections for dissociation of 14 u molecules (mainly $^{12}C^{1}H_2$ and $^{13}C^{1}H$) are sufficient to reduce their intensity up to 11 orders of magnitude at rather moderate stripper densities [10]. First experiments demonstrated that it was possible to achieve the $^{14}C/^{12}C$ atom ratios that are necessary for dating applications analyzing the 1+ charge state after the stripping process. This technology was then demonstrated to be competitive with traditional AMS using the 3+ or 4+ charge states [11].

The importance of this result lies in the fact that the maximal yield for the 1+ charge state can be reached at energies of about 500 keV, i.e. much lower than the energy required for higher charge states maximal yields. This principle set the fundamentals to the design of AMS systems with terminal voltages of 1 MV and below.

The first compact 600 kV AMS facility for ^{14}C was developed at ETH in collaboration with NEC in the early 2000s. Several modifications to the original setup were progressively made in order to broaden the practicality of the system to other radionuclides than ^{14}C and improve the overall performance. In 2005, HVEE designed a compact multi-elemental AMS facility based on a 1 MV Tandetron™ accelerator [12], which was installed at the Centro Nacional de Aceleradores (CNA, Seville, Spain) [13].

Since then, companies and research groups have oriented their efforts in the improvement of the compact AMS systems technology and in reducing more and more their sizes and, in consequence, the maximum voltage of the accelerator. The molecules and isobars suppression techniques have been constantly improved and the detectors optimized for the specific AMS purposes. Figure 1.1 illustrates the so-called “AMS Moore’s law” and shows the exponential decrease with time of the required ion energy to perform radiocarbon detection. In about 40 years, the needed energy for efficient radiocarbon measurements decreased by three orders of magnitude.

In the last years, the use of He gas as stripper has represented a significant advance for the low-energy AMS technology. Initially tested at 200 kV ^{14}C-dedicated facilities [14], it soon revealed its potential in multi-elemental instruments, where it provided considerable improvements for heavy ions measurement at terminal voltages below 600 kV [15]. Currently, He stripping is a fundamental element in the design of the next

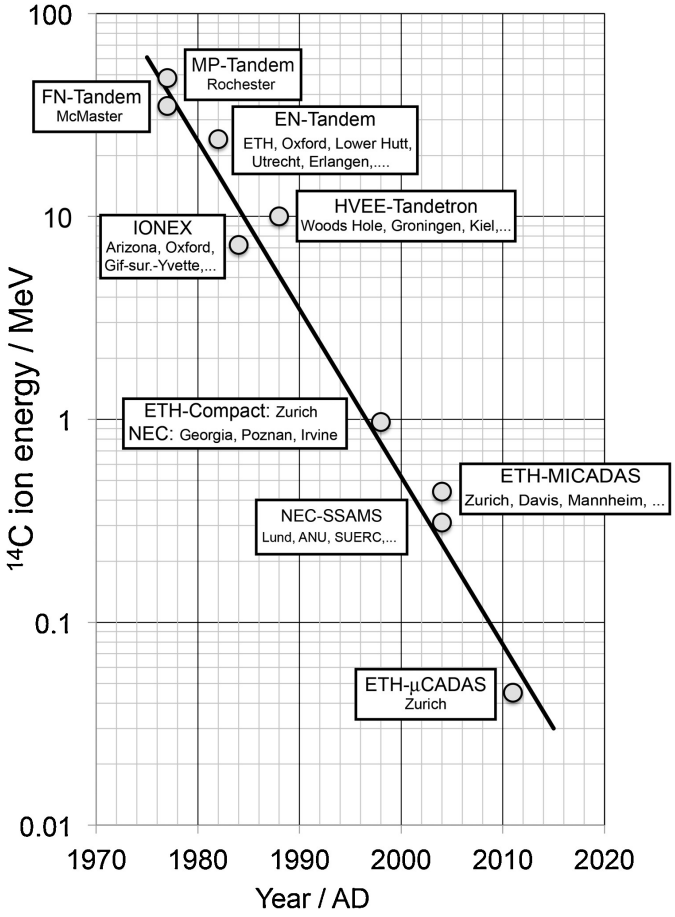

Figure 1.1: The so-called Moore's law for the AMS technology [7].

generation of multi-purpose AMS facilities operating at terminal voltages below 300 kV [16].

The advent of compact AMS facilities has had a strong impact on the research involving radionuclides studies, due to their smaller size, their lower maintenance costs and their ease of operation. All these advantages lead to a rapid and large diffusion worldwide of this technique (Figure 1.2).

1.3 Motivation and thesis outline

The work presented in this thesis has been carried out on the 1 MV AMS facility hosted at the CNA. Several technical modifications have been carried out to the original system since its installation in 2005 to improve its overall performance. In particular, two important upgrades were made in the last years and have motivated the work I present: the installation of He as stripper gas and of a high-resolution gas ionization chamber optimized for light ions detection at low beam energies. Studies and experiments have been conducted in order to characterize this modified system for light radionuclides such as ^{10}Be and ^{26}Al in diverse configurations.

As it was previously explained, the 1 MV AMS CNA facility was one of the first compact instruments operating worldwide and the first one designed and manufactured by HVEE. So far, the company has produced 14 instruments based on the same or a similar design [17]. However, most of those system use Ar as stripper gas, so the experimental information on the performance of He gas at such terminal voltages is very scarce. Therefore, the work conducted at the CNA during the last years gives an useful insight to the mechanisms governing the stripping process with He gas at low energies, and represents a reference for other laboratories hosting similar instruments.

The optimization of ^{10}Be and ^{26}Al measurements is of great interest within the AMS community since those light radionuclides have a large range of applications in Earth sciences. The challenge of measuring ^{10}Be is the elimination of the isobar ^{10}B (stable, 20% isotopic abundance). This is in contrast to ^{26}Al, where the isobar ^{26}Mg can be

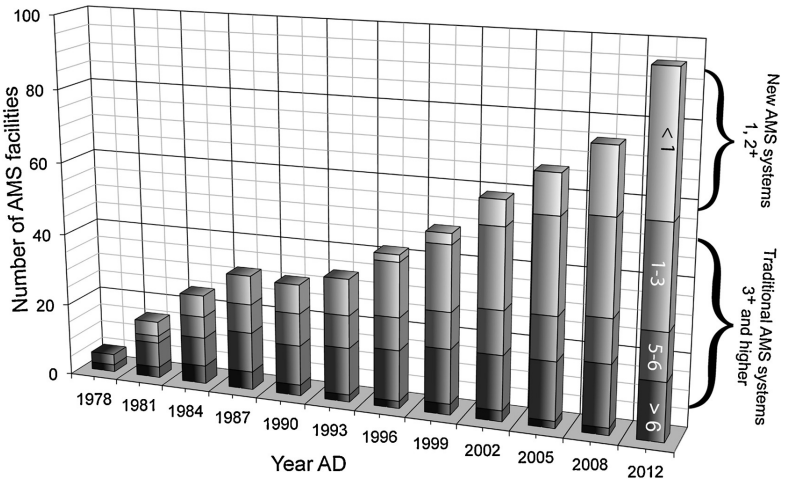

Figure 1.2: Evolution of number of AMS facilities over time [7]. The bottom segments present for the years 1978–2008 represent cyclotron AMS systems which have completely disappeared since 2008.

eliminated by analyzing Al^- after the ion source (since Mg does not form negative ions), but with a poor measurement efficiency. Several experiments were carried out in order to define the behaviour of these elements in the new stripper and to maximize the measurement efficiency when specific techniques are used. The sensitivity of the machine, i.e. the lowest detectable isotopic ratios in the samples, is affected by several mechanisms occurring along the different phases of the AMS process. During the optimization work, identifying the background sources was essential, in order to take measures and minimize their undesired contribution. Two methods were applied and analyzed for intense interferences suppression: the so-called degrader and absorber techniques. The first consists in placing a thin degrader foil (normally made of silicon nitride) in the beam path before an electrostatic or magnetic analyzer, so that ions with different atomic number emerge the membrane with different energies and can be discriminated by the following filter. In the second, an absorber cell is positioned in front of the rare isotope gas ionization chamber with such a thickness to stop the interference and allowing the radionuclide of interest to enter the detector.

This section was given with the main purpose of introducing the reader to the AMS

technique and to highlight the interest of this work in the context of compact facilities. The rest of the thesis consists of four chapters.

In Chapter 2, an overview of the CNA AMS facility will be given, with a recap of the modifications carried out since its installation in 2005. A deeper focus will concern the implementation of the He stripper and the new detector. The obtained figures of merit after the upgrades (transmission through the accelerator and detector resolution) will be presented and compared with the ones relative to the previous setup, where Ar gas was used as a stripper and non-optimized gas detector was used for the final identification of the isotopes of interest.

Chapter 3 will be dedicated to the description of the optimization procedure of ^{26}Al measurements with the upgraded facility, which consisted in a detailed analysis of the efficiency and the background of the different charge states at the exit of the accelerator. After showing the advantages and the issues related to the ^{26}Al measurements in the 2+ charge state (i.e. high stripping yield and the intensity of the $^{13}C^{1+}$ in the detector, respectively), the tests carried out with the passive absorber technique will be introduced, specifying the importance of a proper detecting system and the potential of such an interference suppression method at compact AMS facilities, where it is nowadays rather uncommon.

The optimization of ^{10}Be measurements will be described in Chapter 4. ^{10}Be AMS necessarily requires the application of sophisticated techniques in order to remove the isobaric ^{10}B interference. Two different approaches will be presented and compared: the degrader and the passive absorber techniques. Since the use of degraders provides an excellent ^{10}B suppression, but with considerable efficiency reduction, the different causes of ^{10}Be beam losses will be discussed, with the support of both experimental data and simulations. In the second part of the chapter, the results of a set of experiments will be given, demonstrating the feasibility of ^{10}Be detection with the passive absorber technique at beam energies below 2.5 MeV. The evolution of the absorber design along this work will be presented, since a preliminary study conducted at the CNA with a very simple setup was followed by tests with an improved absorber within a collaboration

with the AMS group of the University of Vienna.

Finally, the conclusive Chapter 5 will summarize the main results and achievements presented in the previous sections and provide an outlook for further studies at the CNA facility.

Chapter 2

The experimental setup: description and developments

2.1 Introduction

The Spanish Accelerator for Radionuclides Analysis (SARA, Figure 2.1) is the 1 MV AMS facility hosted at the Centro Nacional de Aceleradores (CNA), in Seville. SARA is the first compact AMS system designed and manufactured by High Voltage Engineering Europe (HVEE, Amersfoort, The Netherlands) [12, 13] and belongs to the first generation of low-energy AMS (LE-AMS) instruments working with electrostatic tandem accelerators with terminal voltages below 1 MV. It was the prototype that set the fundamentals of a series of 14 further 1 MV HVEE machines that are operative nowadays worldwide and some more to be installed [17].

As a multi-elemental facility, the SARA system has allowed the analysis of a great variety of radionuclides since its installation in February 2006. Besides ^{10}Be, ^{14}C and ^{26}Al, which passed the acceptance test, the CNA AMS group successfully investigated the possibility of carrying out measurements of other nuclides such as ^{41}Ca, ^{129}I and actinides (^{236}U, ^{237}Np, ^{239,240}Pu, ^{241,243}Am) [18, 19]. In 2012, ^{14}C measurements were moved to the Spanish MIni CArbon DAting System (Spanish MICADAS [20]), which is

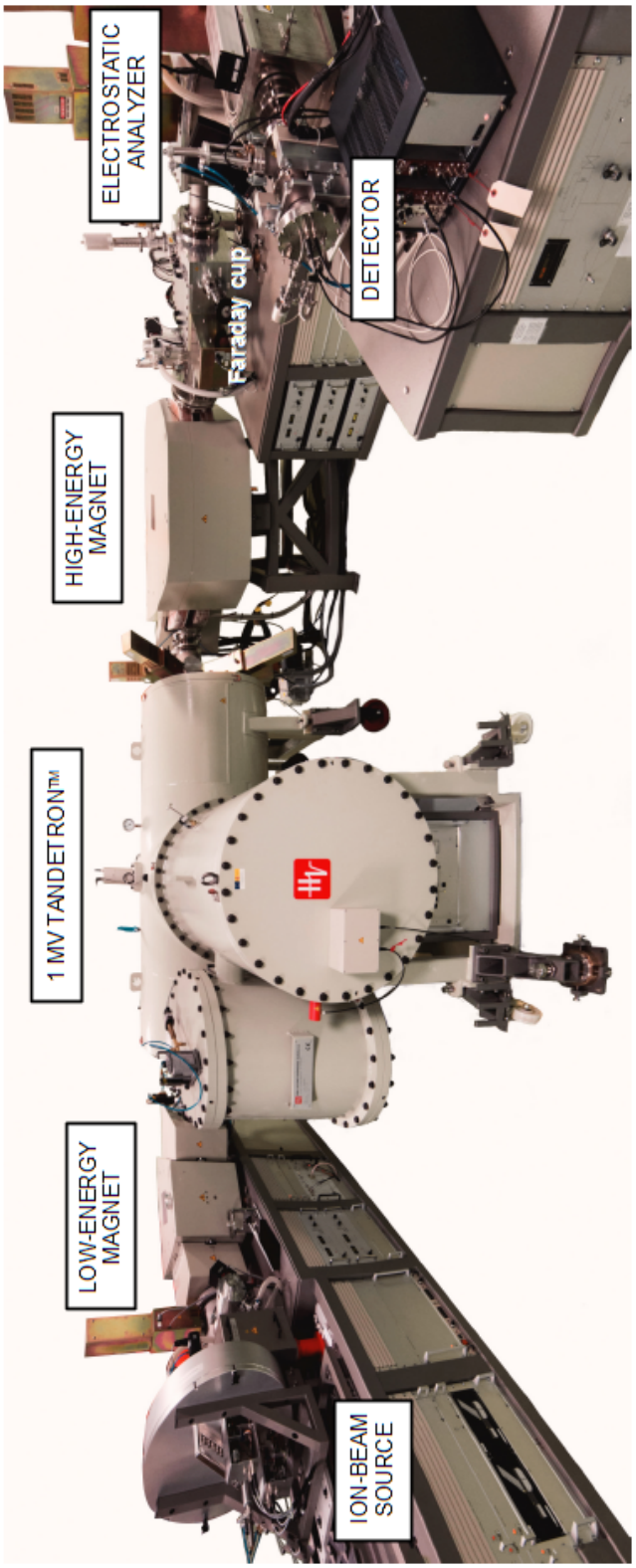

Figure 2.1: The 1 MV AMS facility installed at the CNA.

a facility dedicated to that radionuclide.

The isotopes measured with the SARA apparatus are presented in Table 2.1, where the half-lives, the isotopic ratios in the general environment and the machine sensitivities with the originally installed setup (i.e. equipped with an Ar stripper and a no-optimized rare isotope detector) are reported [19].

To progressively improve the SARA facility performance, several hardware and software modifications have been implemented in the last years. In the following sections, an overview of the facility will be given and the main changes to the original setup will be described.

2.2 The SARA facility

The layout of the SARA facility is shown in Figure 2.2. The apparatus has a compact design and occupies an area of just 3.8 x 6.3 m^2. It is constituted of an ion source, a 90º sector low-energy magnet (LE magnet), a 1 MV electrostatic tandem accelerator, a 90º sector high-energy magnet (HE magnet), a 120º electrostatic analyzer (ESA) and a detection system based on a gas ionization chamber.

The source generates a negative ion beam (X^-) through a Cs^+ sputtering process. The ions are selected on their masses by the 90º LE magnet before entering the 1 MV Tandetron™ accelerator where they are stripped to positive ions ($X^- \rightarrow X^{N+}$) passing through a stripping channel, i.e. a windowless gas cell. This is a key phase in the AMS technique as the stripping is responsible for molecular background suppression and also determines the measurement efficiency. Due to the charge reversal in the stripper, the ion beam is accelerated again towards ground potential and reaches the HE side of the facility. In order to select the mass m, the charge state q and the energy E of the investigated isotope, as well as to filter scattered molecular fragments with similar kinematic properties as the radionuclide of interest, a HE spectrometer consisting of a 90º deflection magnet (mE/q^2 filter) and a 120º electrostatic deflector (E/q filter) is following the accelerator. The geometric properties of SARA's deflectors are presented in Table

Table 2.1: Recap of the radionuclides investigated through the AMS technique at CNA with their half-lives and isotopic ratios in the general environment. The sensitivities achieved with the original SARA setup are also listed.

Radionuclide	Half-life (y)	Environmental isotopic ratio	Sensitivity [19]
^{10}Be	$1.51 \cdot 10^6$	$\frac{^{10}Be}{^{9}Be} = 10^{-11} - 10^{-5}$	$4 \cdot 10^{-14}$
^{14}C	5730	$\frac{^{14}C}{^{12}C} = 10^{-14} - 10^{-11}$	$2 - 4 \cdot 10^{-15}$
^{26}Al	$7.08 \cdot 10^5$	$\frac{^{26}Al}{^{27}Al} = 10^{-13} - 10^{-12}$	$3 \cdot 10^{-14}$
^{41}Ca[a]	$1.03 \cdot 10^5$	$\frac{^{41}Ca}{^{40}Ca} = 10^{-14} - 10^{-11}$	10^{-11}
^{129}I	$1.57 \cdot 10^7$	$\frac{^{129}I}{^{127}I} = 10^{-12} - 10^{-7}$	$2 \cdot 10^{-13}$
^{236}U	$2.34 \cdot 10^7$	$\frac{^{236}U}{^{238}U} = 10^{-12} - 10^{-6}$	$5 \cdot 10^{-11}$
^{239}Pu[b]	24110	-	10^6 atoms

[a] Samples with anthropogenic contamination are measured, with typical isotopic ratios of ^{41}Ca/^{40}Ca = $10^{-10} - 10^{-8}$.

[b] Anthropogenic radionuclide. The sensitivity is similar for ^{237}Np, ^{240}Pu and ^{243}Am.

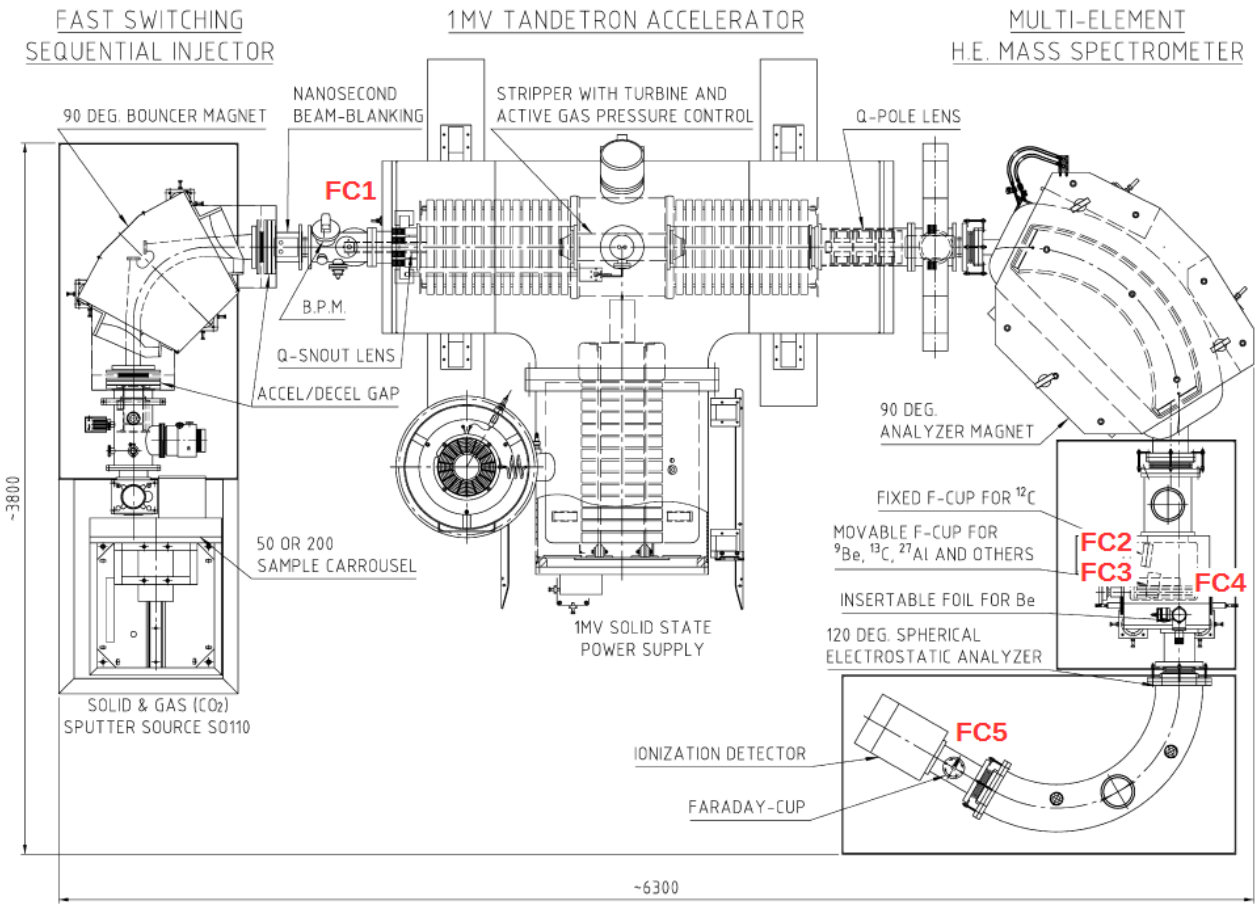

Figure 2.2: Schematic representation of the SARA facility [12].

2.2. Finally, the rare isotope is counted and identified in a $\Delta E - E_{res}$ gas ionization chamber, while the stable one is detected as a beam current in a Faraday cup set in an off-axis position before the electrostatic analyzer.

The original setup is described in detail in [21]. In the following subsections, an overview of each component and the upgrades realized during the years will be presented.

2.2.1 The ion source

Negative ions are produced from the samples[1] in a Cs^+ sputtering ion-source equipped with a a chamber with a capacity for 200 cathodes (i.e. the so-called carousel) with automated remote target loading. During routine measurements, ions usually outgo the source with an energy of 35 keV. The housing of the ion-source is at ground potential. An extraction cone adjusts the beam position to the following components of the facility LE side.

One common issue of sputtering sources is the so-called memory effect or cross-talk. During the Cs^+ sputtering process, negative ions and neutral species are extracted from the sample. Many of them leave the ion source guided by the electrostatic potentials, but others deposit on nearby surfaces (the source electrodes and insulators) or stay in the surrounding volume. To avoid the deposition of additional material on the neighbouring sample, exclusively the sample to be analyzed is transferred from the carousel to the inner of the source where the sputtering process takes place.

The source model SO-110 originally installed was replaced in 2012 by the upgraded version SO-110B [19, 22, 23]. The new source provided a better general operation, with reduced cross-contamination (particularly evident for volatile elements) thanks to a more efficient pumping of the volume where the sputtering takes place, and less frequent maintenance service, thanks to a more convenient design of the insulating parts. Furthermore, the geometry of the cathodes was adapted by our group to get a more efficient use of the sample material, as it is described in [19].

[1] Samples are also called cathodes, as they stay in the source at a positive potential.

Table 2.2: Geometric properties of SARA's kinematic filters.

Filter	Radius (cm)	Angle (°)	Resolutive power
LE magnet	40	90	680 $\frac{mm}{\Delta p/p}$
HE magnet	85	90	1300 $\frac{mm}{\Delta p/p}$
ESA	65	120	650 $\frac{mm}{\Delta p/p}$

2.2.2 The low-energy side

An Einzel lens focuses the divergent ion-beam leaving the source on the object position of the LE magnet, the first mass selective element in the beam path. In addition to the selective task, the LE magnet is equipped with the so-called bouncer, that adjusts the beam energy to allow the sequential injection in μs pulses of the rare and the abundant isotope into the accelerator without changing the magnetic field [24]. A Y-Steerer optimizes the vertical position of the beam to maximize its transport through the accelerator and serves as an ultra-fast beam blanking unit, defining with nanosecond precision the duration of the injection pulses [25].

The resolution of the magnetic filter can be selected by the closure of a pair of horizontal slits or the insertion of a 3 mm diameter aperture at its image position. The ion or molecule current extracted from the ion-source can be measured in a Faraday cup placed after the LE magnet (FC1).

2.2.3 The accelerator

SARA's accelerator is a Tandetron™ system and it is designed to work between 400 kV and 1000 kV. Its vertical section is schematically represented in Figure 2.3. The stripper channel is placed at its terminal and consists in a cylinder with 30 cm length and 6 mm diameter opened at its basis. A 400 L/s turbo-molecular pump recirculates

the stripping gas and ensures good vacuum conditions in the LE and HE acceleration tubes [26]. The bottle containing the stripping gas is connected to the middle of the channel, thus the gas thickness is maximum in this position and presents an exponential decrease toward the opposite ends (Figure 2.4). A vacuum sensor measures the gas pressure in the middle of the stripper channel. Experimentally measured pressures p [mbar] can be converted to mass thicknesses [μg cm^{-2}] assuming the gas as ideal and equally distributed along the channel with a pressure p/2 to take into account the pressure difference between the middle and the opposite ends of the channel:

$$\rho x = \left(\frac{M_{gas} L}{RT} \right) \frac{p}{2} \tag{2.1}$$

where M_{gas} [g mol^{-1}] is the stripping gas molar mass, L = 30 cm is the channel length, R = 83145 mbar cm^3 K^{-1} mol^{-1} is the gas constant and T = 300 K is the room temperature.

The originally installed Ar stripper gas was replaced by He in November 2014. A detailed description of the stripping process and the gas replacement will be discussed in Section 2.4.1.

The beam is focused on the middle of the stripper channel thanks to a Q-Snout lens located at the entrance of the LE acceleration tube, whereas at the exit of the HE acceleration tube a quadrupole triplet lens is installed to fulfill the ion-optics requirements of the HE spectrometer for every charge state [21].

Ions emerge from the the accelerator with an energy E [eV]:

$$E = \frac{m}{M} e(V_S + V_T) + qeV_T \tag{2.2}$$

where m is the rare isotope's mass, M is the mass of the anion extracted from the ion-source, V_S is the extraction voltage from the source and V_T is the accelerator terminal voltage (both in Volts), q is the selected charge state and e is the charge of the electron. The stripping energy E_{str} [eV] represents the energy calculated in the middle of the stripper channel and is given by:

$$E_{str} = \frac{m}{M} e(V_S + V_T) \tag{2.3}$$

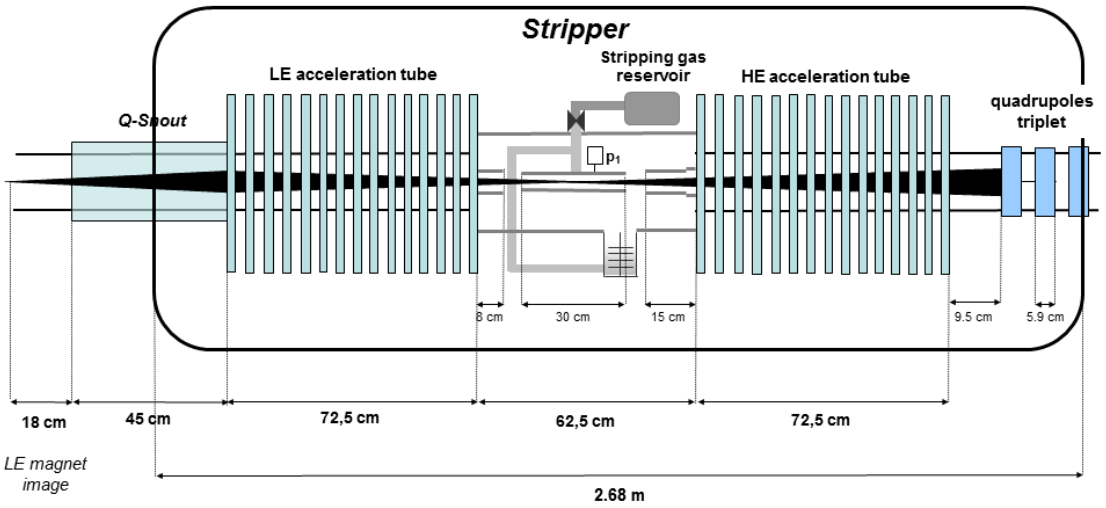

Figure 2.3: Schematic representation of the vertical section of SARA's accelerator [21].

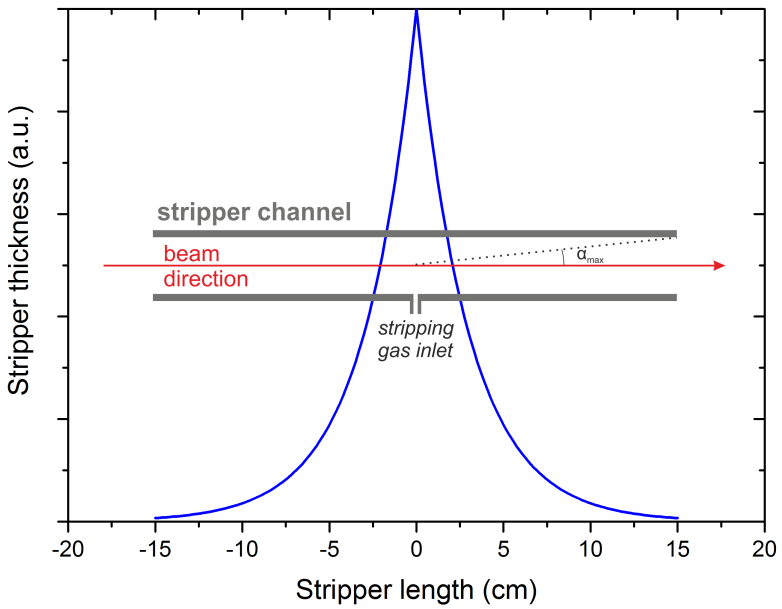

Figure 2.4: Gas thickness profile in the stripper channel. In the case of the SARA facility, the channel length is 30 cm, its width is 6 mm and α_{max} is 15 mrad.

2.2.4 The high-energy side

The HE spectrometer is based on a 90º HE magnet and a 120º ESA. The HE magnet is mainly responsible for the selection of one of the charge states available after the stripping process, whereas the ESA realizes an energy separation of the ions. The main characteristics of SARA's kinematic filters are summarized in Table 2.2.

At the exit of the accelerator, a HE Y-Steerer adjusts the beam position in the vertical direction. Four Faraday cups (FC2, FC3, FC4, FC5) are positioned along the HE side as shown in Figure 2.2. During the measurements, the stable or major isotope is measured as a beam current in the FC3, whose position can be adjusted along the image position of the HE magnet. A redesign of the printed circuitry boards associated to the FC3 and an upgraded version of the acquisition software improved the cup precision in 2013 [19]. The FC2 is used exclusively for the monitoring of the ^{12}C beam during ^{14}C measurements, whereas the retractable FC4 and FC5 Faraday cups are used for tuning purposes.

A holder for degrader foils is placed at the beam waist position between the HE magnet and the ESA, allowing an easy and fast insertion of the membranes in the beam path during ^{10}Be measurements. Degraders are indispensable to obtain a partial suppression of the isobaric ^{10}B interference, as it will be widely discussed in Chapter 4.

A system of slits and apertures allows the regulation of the beam dimensions and the optimization of the transmission against the background.

2.2.5 The rare isotope detection system

Rare isotopes are detected and counted in a gas ionization chamber (GIC) placed at the end of the beam line. Its design features are the followings.

The anode is split in two plates to give the opportunity of obtaining ΔE-E$_{res}$ information, about both the ion energy and position. A Frisch grid, placed in front of the anodes, removes the dependency of the position in the perpendicular plan from the induced signal on the electrodes. As entrance windows, extremely thin and homogeneous silicon nitride membranes ($Si_3N_{3.1}H_{0.06}$ [27]) are mounted, which minimize the energy loss and the

energy and angular straggling suffered by the beam after passing through them. Silicon nitride foil dimensions have to be chosen (i) to withstand the pressure difference of $10^3 - 10^4$ mbar between the inside of the detector and the beam line, which is at high vacuum (i.e. at the 10^{-7} mbar level), and (ii) to achieve a high beam acceptance. Typical thicknesses range between 30 and 100 nm, with an area not smaller than 3x3 mm^2. Ar and isobutane (C_4H_{10}) are the most common counting gases.

The signals from both anodes are independently processed in a conventional electronic chain constituted by a charge sensitive preamplifier, an amplifier, an analog to digital converter (ADC) and a multichannel analyser, before being displayed in a two-dimensional spectrum using the software MPA-NT [28].

In 2015, the GIC provided by HVEE was replaced by a new one designed and assembled by the Ion Beam Physics group at the Eidgenössische Technische Hochschule Zürich (ETH, Zürich, Switzerland). Although the numerous differences which will be described in Section 2.4.2, the main characteristics are common.

2.3 Measurements optimization

To find the optimal measurement conditions, two parameters need to be studied for each radionuclide: (i) the overall counting efficiency, which depends on the ion-source yield of the analyzed ion-beam on the LE side and the transmission of the charge state of interest to the detector, and (ii) the background level, representing the sensitivity of the system. An optimization work consists in searching for the specific settings that allow the highest counting efficiency and the lowest background.

2.3.1 The overall efficiency

The measurement yield of an AMS system is related to the negative ions extraction from the ion-source and the beam transmission through the whole facility (i.e. the so-called overall efficiency).

The production and extraction of negative ions from the Cs^+ sputtering ion-source depend on the following factors: (i) the type and concentration of the metallic matrix (e.g. Cu, Nb or Ag) used to dilute the samples, (ii) the ion-source operation conditions and (iii) the extracted chemical specie [29].

The overall efficiency ϵ of an AMS facility represents the transmission of the ions in their whole path, from the source to the detection system. It can be expressed as:

$$\epsilon = \epsilon_c \cdot \epsilon_o \cdot \epsilon_d \tag{2.4}$$

where ϵ_c is the yield of the studied charge state in the HE analyzer, ϵ_o the optical transmission through the different component of the facility and ϵ_d the counting efficiency of the detecting system. These parameters are summarized below.

(a) Charge state yield

The yield of positive charge states in a stripping process is determined by the charge exchange cross-sections for electron capture and ionization processes. Cross-sections are related to the beam atomic number and energy and to the ionization potential of the stripping material. The LE-AMS technology is based on the use of a gaseous stripper and the selection of charge states below the 3+ at the exit of the accelerator.

(b) Ion optical losses

Optical losses take place when the dimensions of the beam does not fulfill the angular acceptance of the different elements of the facility (e.g. the stripper channel or the detector entrance window). Furthermore, to optimize the system mass and/or energy resolution, the insertion of slits and apertures in the beam path is often required: if properly set, they considerably reduce the background events without affecting too much the overall efficiency.

(c) Detector counting efficiency

The efficiency of the detector is given by the charge collection efficiency in the active volume. According to the experience with SARA, i.e. with beam energies

ranging between 1 and 4 MeV, if the electronic noise levels are sufficiently low, good energy resolutions are achievable with a proper choice of the entrance windows and the counting gas, allowing the identification of the peaks in the spectra without ambiguity. SARA's detector efficiency is normally close to 100%, but it can be reduced by effects related to the acquisition electronics such as pile-up events or a high counting dead time.

In LE-AMS, ions pass through a gaseous stripper inside of the accelerator. The transmission T_{acc} for a selected charge state q at the exit of the tandem is defined as:

$$T_{acc} = \frac{I_{HE}}{q \cdot I_{LE}} \tag{2.5}$$

where I_{LE} and I_{HE} are the major isotope currents measured in the LE (in FC1) and HE (in FC3 or FC4) sides of the facility, respectively. At a given stripping energy, the transmission depends on the gas thickness and is maximum for a specific value $p = p_{eq}$ (Figure 2.5). At $p > p_{eq}$, assuming the ions subjected to single scattering processes, T_{acc} can be approximated to a decreasing exponential function of p [30]:

$$T_{acc} = \Psi_q \cdot e^{-\sigma p}, \tag{2.6}$$

where σ is the angular dispersion cross-section for angles above the maximum one that can be accepted by the HE acceleration tube and Ψ_q is the ionization yield relative to the q charge state. In the case of the SARA facility, the angular acceptance of the HE acceleration tube is about 15 mrad. The extrapolated transmission at $p = 0$ represents the ideal case where the beam does not suffer any scattering losses and corresponds to the charge state yield Ψ_q. Therefore, the transmission estimated through Formula 2.5 reflects both the selected charge state yield and the optical losses in the stripper channel.

Even if high transmissions are preferred since they affect the counting efficiency, sometimes the application of a higher stripping density ($p > p_{eq}$) with consequent transmission losses is necessary to remove molecular background (e.g. during ^{26}Al measurements in the 1+ charge state, as it will be discussed in Chapter 3). In other cases, vice versa, where molecules are not a concern (e.g. when the 3+ charge state or one above

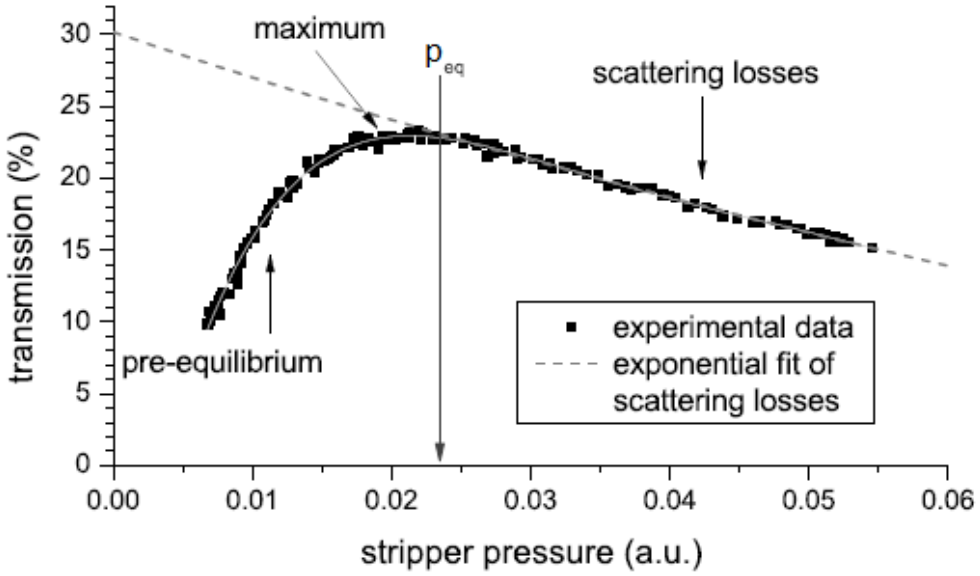

Figure 2.5: Dependency of the transmission on the stripper pressure. The exponential fit describes the beam losses caused by angular scattering in the stripping channel.

is selected), working at lower stripper mass thicknesses ($p < p_{eq}$) has the advantage of reducing the background caused by scattered ions in the accelerator tubes (e.g. for ^{236}U [31]).

The transmission through the HE spectrometer T_{HE} is quantified by measuring the isotopic ratio R_{meas} of standard samples with a nominal ratio R_{nom}:

$$T_{HE} = \frac{R_{meas}}{R_{nom}} \tag{2.7}$$

For ordinary measurements, T_{HE} gives an estimations of the optical losses in the HE side of the facility and the detector counting efficiency, and is normally above the 90%. However, in addition to the stripping process in the terminal of the accelerator, a post-stripping can be necessary in specific cases to remove isobaric interferences. For instance, ^{10}Be is commonly measured in LE-AMS systems by inserting a degrader silicon nitride foil in the beam path before an energy dispersive kinematic filter with the purpose of removing the intense ^{10}B beam. Being the energy loss in the degrader dependent on the

projectile's atomic number Z, ^{10}Be (Z = 4) and ^{10}B (Z =5) leave the foil with different residual energies and can be separated in terms of their energy. The degrader acts as an additional stripper, generating a distribution of charge states and enhancing the energy and angular dispersion of the beam. In this case, the yield of the selected charge state after the degrader, the losses in the kinematic filter and the detector counting efficiency are reflected in T_{HE}, which drastically reduces to 10-20% depending on the beam energy and the degrader material. The different contributions to efficiency reduction during ^{10}Be measurement with the degrader technique will be discussed in Chapter 4.

The overall efficiency ϵ through the system can be therefore expressed in terms of the experimentally measured T_{acc} and T_{HE}:

$$\epsilon = T_{acc} \cdot T_{HE} \tag{2.8}$$

2.3.2 The background

The background R_{tot} represents the minimum atomic ratio between the rare and the abundant isotope that can be measured with SARA for different radionuclides. R_{tot} results from the sum of several contributions [32]:

$$R_{tot} = R_{real} + R_{iso} + R_{mol,HE}(\delta) + R_{scat}(\delta^*) \tag{2.9}$$

where R_{real} represents the background generated by the radionuclide itself, R_{iso} represents the contribution of isobars, $R_{mol,HE}$ is the counting rate of molecules surviving the stripping process and R_{scat} is due to the scattering processes in the acceleration tubes.

R_{real} is caused by sample contamination or by memory effects in the ion-source. Isobars suppression (R_{iso}) requires specific techniques involving the chemical process to produce the samples or a physical separation in the spectrometer.

$R_{mol,HE}$ exponentially decreases with the stripper thickness δ, according to:

$$R_{mol,HE}(\delta) = \frac{N_{mol,LE}}{N_{ab}} e^{-\sigma_{mol} \cdot \delta} \tag{2.10}$$

where $N_{mol,LE}$ is the number of molecules before entering the stripper, N_{ab} is the abundant isotope rate and σ_{mol} is the cross section for molecular destruction. R_{scat}

depends on the areal density in the acceleration tubes δ^* that increases with δ:

$$R_{scat}(\delta^*) = \frac{N_{proj}}{N_{ab}}(1 - e^{-\sigma_{scat}\cdot\delta^*}) \tag{2.11}$$

where N_{proj} is the number of projectiles (atoms or molecules) entering the stripper. The explanation of such a behaviour is in the worsening of the vacuum conditions in the accelerator tubes, which generates background events by scattering and charge exchange processes. The dependence of $R_{mol,HE}$ and R_{scat} on the stripper thickness is shown in Figure 2.6 [32]. It is clear that particular attention needs to be paid in the choice of the stripper thickness for its important influence on the background. A study of blank samples[2] at different stripping pressures can give information about the background sources and a chance to reduce it.

2.4 Recent modifications and aims

The complexity of an AMS instrument arises from the necessity of obtaining an optimal beam transport from the source to the detector, while achieving a background suppression factor of up to 15 orders of magnitude in many cases. In this context, the stripping process and the rare isotope detection system play a fundamental role in the measurements optimization.

In 2015, a He stripper gas and a high-resolution GIC have been implemented at the SARA system. In the next two sections, these two items will be discussed more in detail with a special focus on the modifications conducted at the SARA facility.

2.4.1 Helium as a stripping gas

The stripping is one of the key processes in AMS as it is responsible for the entire dissociation of the molecular isobars and it determines the measurement efficiency.

In the stripper, the ion beam components experience charge exchange processes with the target atoms or molecules (ionization and electron capture processes), emerging

[2] A blank sample is made with material with nominally no content of the studied rare isotope.

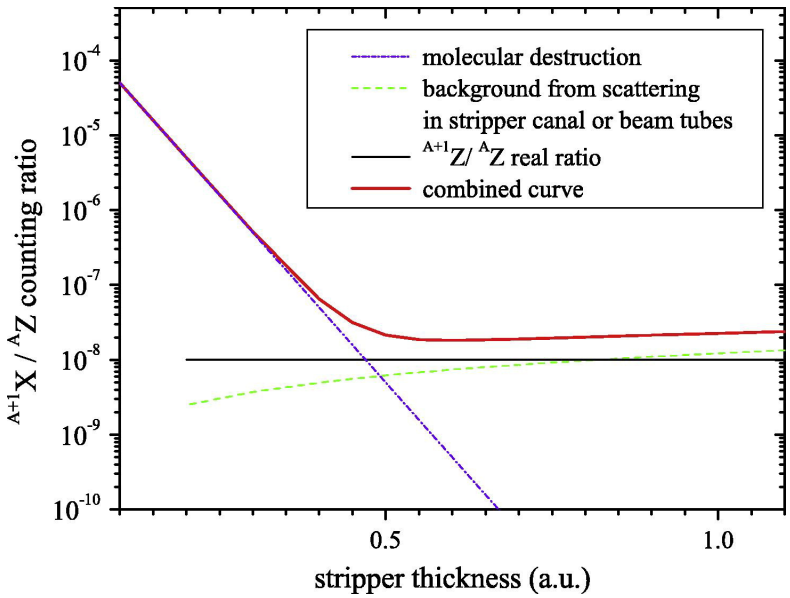

Figure 2.6: Dependency of the different contributions to the background on the stripper thickness [32].

from the accelerator in a distribution of positive charge states. The injected molecules are dissociated thereby by an appropriate selection of the charge state and the stripper pressure.

The fraction of the total incident particles that populates a given charge state after the stripping process gives the ionization yield. As multiple positive charge states are produced, a significant fraction of the beam is lost as the result of the selection of a given charge by the HE magnet. Further beam losses are due to the angular straggling that the beam suffers when passing through the target gas, so that many particles cannot be transmitted through the stripper channel. The fraction of lost particles defines the optical transmission through the accelerator which, multiplied by the stripping yield, gives the transmission for a given charge state according to Equation 2.6.

A critical parameter for the measurement performance of an AMS system is constituted by the stripper thickness, that needs to be high enough to assure an entire dissociation of molecular interferences, since for charge states below 3+ molecules might survive the stripping process [32]. For this reason, in many cases the stripper density has

to be set to such high values, that significant beam losses due to angular straggling are observable. Additionally, the thicker the stripper is, the higher is the presence of residual gas in the acceleration tubes that can cause additional scattering and charge exchange processes resulting in an increase of background events.

A high population yield for the available charge states and reduced losses in the stripping channel is convenient for AMS systems. All these processes depend on the nature of the gas target and several studies performed on facilities with terminal voltages below 600 kV showed the advantages of He stripping on different isotopes.

First experiments conducted on ^{14}C ions at the 200 kV MICADAS facility revealed a high population yield for the 1+ charge state and reduced angular scattering losses in He stripper compared to the heavier Ar or N_2 gases [14]. This is an effect of the lower atomic number of He nuclei (Z_{He} = 2, whereas Z_N = 7 and Z_{Ar} = 18). He stripping was also suitable in ^{14}C-dedicated facilities with lower terminal voltages or even without any acceleration stage (as in the cases of μCADAS [33] and myCADAS [34], where ions' energy is given exclusively by the source extraction voltage), allowing measurements at very low energies with transmissions of 40%.

Following the results obtained at the MICADAS, He stripping was tested on different isotopes at the multi-elemental 600 kV Tandy facility. As it is shown in Figure 2.7, for uranium ions at a stripping energy of 325 keV (300 kV terminal voltage), the mean charge state with He gas is higher than in other gaseous or solid strippers, resulting in a strongly populated 3+ charge state (i.e. three times higher compared to Ar). At the same time, about 20% of the beam is lost in the stripper channel compared to the 30% measured for heavier gases like Ar [15]. Actinides measurements benefit from He stripping also for terminal voltages between 1 and 2 MV, with a 3+ charge state yield of about 40% as it has been demonstrated at the Vienna Environmental Research Accelerator (VERA, Faculty of Physics, Vienna, with 3 MV maximum terminal voltage) [35].

He stripping provides interesting results at the Tandy also for light elements as beryllium and aluminium [37]. An unexpected behaviour is observable for beryllium in the 2+ charge state for stripping energies between 90 and 200 keV (terminal voltages V_T

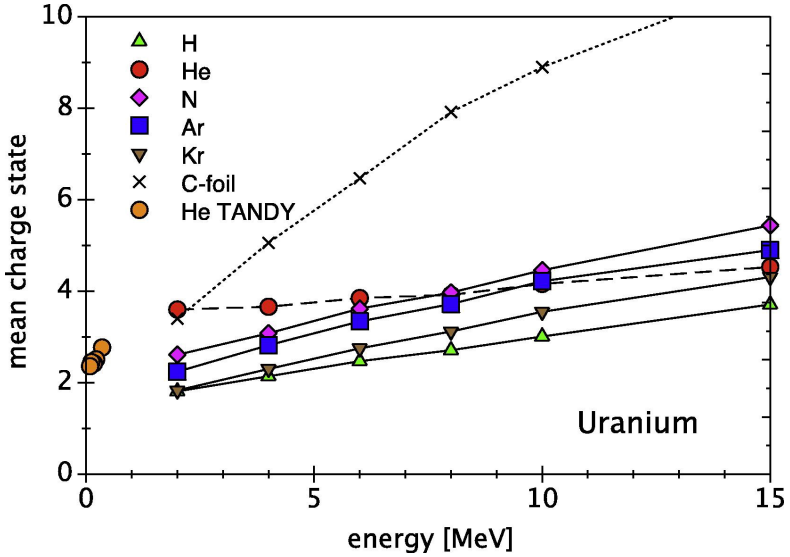

Figure 2.7: Mean charge state of uranium ions as a function of energy for various stripper media [15, 36].

between 200 and 500 kV): a local transmission maximum of 37% appears at about 120 keV (V_T about 300 kV), as it is shown in Figure 2.8. This is unusual, because the mean charge state ordinarily increases with the beam energy. In the energy range between 300 keV and 600 keV (V_T between 300 and 600 kV), maximal transmissions of 50-60% for Al in the 2+ charge state have been reported. But the very high presence of the $^{13}C^{1+}$ m/q ambiguity makes it necessary its suppression by additional techniques, as the introduction of passive absorbers before the detector, as it will be discussed in Chapter 3.

The reported advantages of He stripping at different AMS systems has encouraged its application to the SARA facility. The conversion to the new stripper has needed the opening of the accelerator, as the stripper gas bottle is located inside the terminal housing. Being gas dependent, the vacuum gauge placed in the middle of the stripper channel has been recalibrated to show reliable pressure readings for He.

So far, there are no experimental data available for terminal voltages between 600 kV and 1 MV, which are accessible with the SARA facility. Therefore, all the obtained information on the CNA instrument is key for a better understanding of the stripping

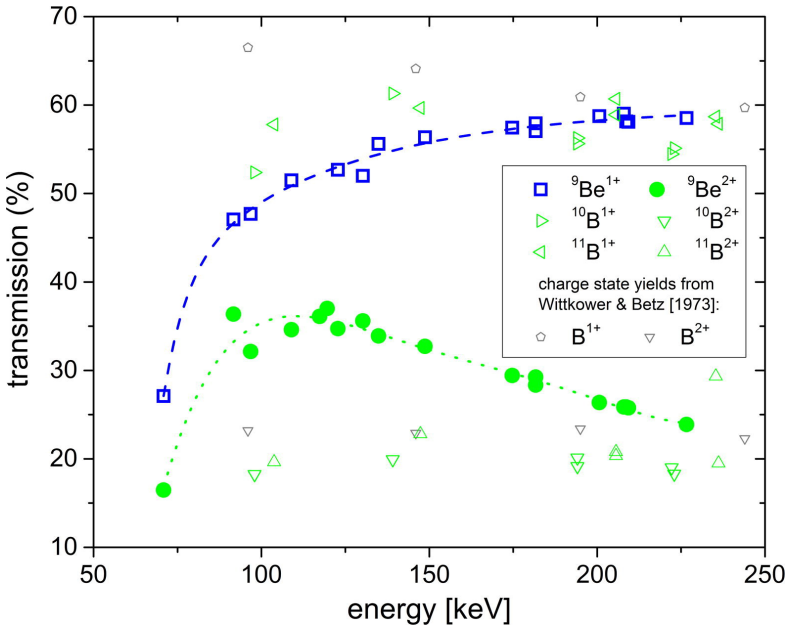

Figure 2.8: Transmissions through the Tandy accelerator for Be and B [37]. They are in a good agreement with the measured charge state yields of B in He for the 1+ and 2+ charge states reported in [38].

process with He at low energies.

Comparison between Ar and He stripping

After the installation of the He stripper, a first study of the transmissions through the tandem has been performed for different radionuclides. The main results are presented in Table 2.3, where the maximum transmissions through SARA's accelerator with Ar and He strippers are compared. The reported values for the He stripper have been obtained from the transmission curves of each isotope, made by measuring the beam currents in the HE and LE sides of the facility at different stripper thicknesses and applying the Formula 2.5.

Light ions transmissions did not present substantial improvements with the He stripper. Beryllium transmission at the terminal voltage of 1 MV did not change for the 1+ charge state, being 58% with both Ar [39] and He, while in the 2+ charge state it slightly reduced from 25% to 22%, respectively. ^{9}Be transmission curves will be given in Chapter 4. Carbon is the more disadvantaged nuclide by the new stripper, since the 2+ charge state transmission decreased from 43% with Ar to 32% with He at 1 MV terminal voltage. Concerning aluminium, the 1+ charge state at 0.7 MV increased its maximum transmission from 23% with Ar [40] to 38% with He. At 1 MV, the 2+ transmission is almost unchanged, whereas the 3+ transmission increased, passing from 13% with Ar to 18% with He. The corresponding transmission curves will be presented in Chapter 3.

The positive effects of the He stripping are particularly evident for heavy ions like iodine and actinides. The maximum achievable transmission through the accelerator for uranium ions is 38%, which corresponds to a charge state yield of 47%, i.e. 20% beam loss in the stripper channel [31]. This is in agreement with the results obtained at the Tandy [15] and VERA [35] facilities. Preliminary results showed a maximum transmission of 27% for iodine with the He stripper, against the 10% achieved with Ar.

The new stripper has had important consequences on the background that had to be taken into account. Background estimations have required a special care and played a crucial role in the optimization of the measurements. Chapters 3 and 4 will be dedicated

Table 2.3: Recap of the measured maximum transmissions obtained for different isotopes and charge states with both Ar and He strippers. The terminal voltage is given by the HE spectrometer acceptance.

Isotope	Charge state	Terminal voltage (kV)	Energy (keV)	Maximum transmissions (%)	
				Ar gas [19]	He gas
^{9}Be	1+	1000	1400	58	58
	2+	1000	2400	25	22
^{12}C	2+	1000	3040	43	32
^{27}Al	1+	700	1440	23	38
	2+	1000	2650	54	52
	3+	1000	3650	12	18
^{40}Ca	3+	1000	3400	6	28 [41]
^{129}I	3+	1000	4030	10	27
^{238}U	3+	650	2590	11	38 [31]

to the study of the facility performance relatively to ^{26}Al and ^{10}Be, respectively, whereas heavier ions are investigated in other works [31, 41].

In general, a deterioration of this figure of merit has been evinced with the new stripper for those isotopes suffering background caused by scattering events, e.g. ^{10}Be and ^{236}U. ^{10}Be is measured at the SARA facility with the so-called degrader technique (see Chapter 4) and its background is mainly due to ^{9}Be molecular fragments (from ^{9}Be^{1}H^{16}O^{-} on the LE side) arriving to the detector after undergoing charge exchange and/or scattering processes in the accelerator tubes and the HE spectrometer, being $1 - 2 \cdot 10^{-14}$ with the Ar stripper and $2 - 4 \cdot 10^{-14}$ with He. Also uranium background almost doubled, passing from $5 \cdot 10^{-11}$ to $9 \cdot 10^{-11}$ because of scattered ^{235}U and ^{238}U molecular fragments.

As shown in Formula 2.11, R_{scat} increases with the stripper pressure since it depends on the vacuum conditions in the accelerator tubes. From the theory of molecular gas flow

[42], the conductance[3] C of a cylindrical tube can be written as [43]:

$$C = 3.81 \frac{D^3}{L} \sqrt{\frac{T}{M}} \tag{2.12}$$

where D and L are the tube diameter and length, respectively, T is the gas absolute temperature and M is the gas molecular mass. It follows that the conductance for He is more than three times higher than Ar:

$$\frac{C_{He}}{C_{Ar}} = \sqrt{\frac{M_{Ar}}{M_{He}}} \approx 3.16 \tag{2.13}$$

Thus, for the same stripper pressure, there is more residual gas in the acceleration tubes when He gas is used as stripper, with the consequent increase of R_{scat}.

2.4.2 The low-noise gas ionization chamber

Improving the ion-detection means maximizing the signal height and minimizing its width (i.e. the signal resolution). The energy resolution is a crucial parameter during the detection of radionuclides suffering the presence of interferences, since it determines the discrimination factor between neighbouring peaks. In the case of a GIC as the one introduced in Section 2.2.5 commonly used in LE-AMS, the resolution mainly depends on three factors: (i) the energy straggling in the silicon nitride entrance window, (ii) the electronic noise, (iii) the statistics of charge production and collection inside the chamber.

As it is shown in Figure 2.9, these three effects contribute in different ways to the total energy resolution depending on the detected ion. The contribution given by the electronic noise is dominant for radionuclides with $Z < 6$, whereas the statistical fluctuations related to charge production and collection condition the resolution for the heavier ones. The energy straggling due to the silicon nitride membrane always represents a minor contribution [44].

[3]The conductance of an accelerator tube is defined as the gas volume passing per unit time through a cross-section of the tube.

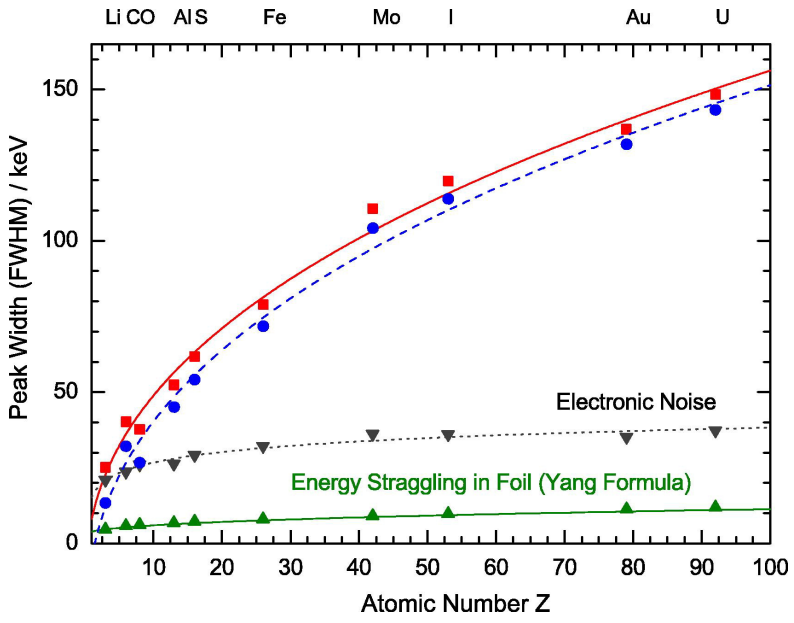

Figure 2.9: Resolution contributions for projectiles having an initial energy of 800 keV as a function of the atomic number [44]. The red points represent the total energy resolution, whereas the blue ones show the contribution of the gas. The energy straggling due to the entrance foil corresponds to a 34 nm thick silicon nitride membrane.

The GIC originally installed at the end of SARA's beam line has been designed and assembled by HVEE. It is schematically represented in Figure 2.10. Anodes' shapes and positions have been conceived for low detector capacitance, with lengths of 15 cm and 31 cm, respectively. Voltage divider rings have been used to create a homogeneous electrostatic field perpendicular to the incoming ions. ORTEC preamplifiers have been connected to the anodes with a 10 cm cable and mounted outside of the chamber containing the detector.

To improve the rare isotope detection, a miniaturized GIC provided by the ETH-Zurich and optimized for LE-AMS requirements has been installed at the SARA system. A schematic of the new GIC is shown in Figure 2.11 and perspective views are given in Figure 2.12. Both anodes have a length of 5 cm with a maximized active area and low-noise CREMAT CR-110 preamplifier modules [45] are mounted directly on the anodic plates through an AC coupling in order to minimize capacitance introduced by cables. In this way, the capacitance associated to the detector is reduced and the preamplifiers noise, which presents a dependence on such capacitance, is reduced as well.

Energy resolution

With its low-noise design, the ETH GIC results particularly suitable for light ions detection, representing the electronic noise the major contribution to their energy resolution. In particular, the detector performance is of great interest in the case of ^{10}Be, since measurements are contingent upon the isobaric ^{10}B interference. Regardless of the technique used to achieve ^{10}B suppression, the final ^{10}Be detection depends on the performance of the GIC, as it is represented in the examples in Figure 2.13. Therefore, optimal resolutions are essential to achieve a clear separation between the different elements entering the GIC.

The new detector performance has been studied with the stable isotope ^{9}Be, but results can be extended to ^{10}Be. The GIC has been calibrated by injecting ions with different energies and evaluating the pulse height in the energy spectrum of the ΔE section. The ^{9}Be beam extracted from the source is normally intense enough to damage

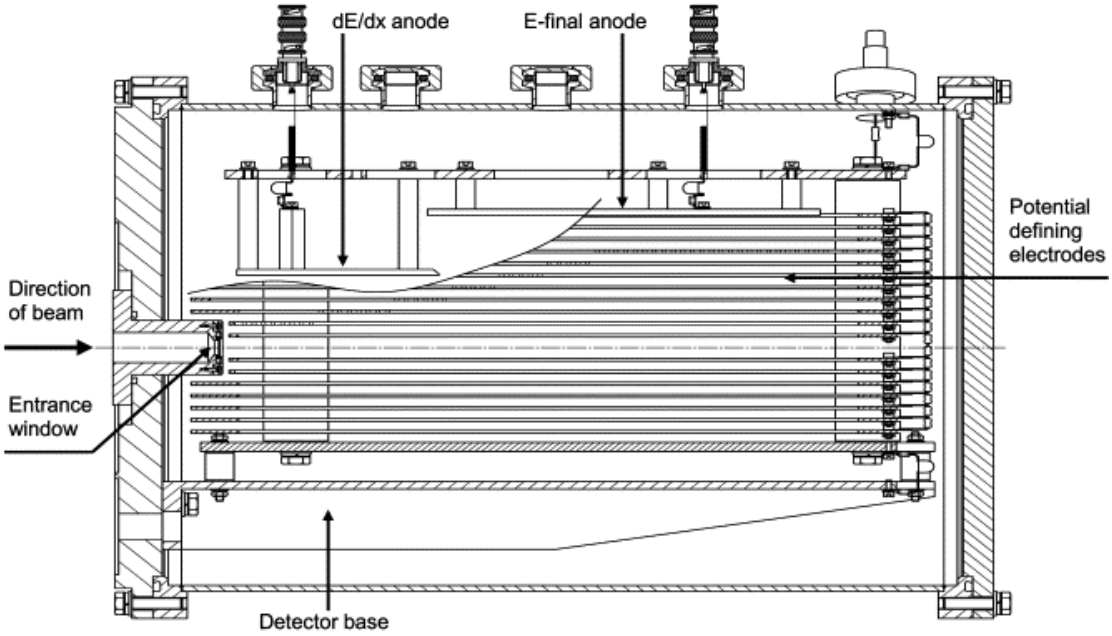

Figure 2.10: Schematic representation of the HVEE detector.

the GIC entrance window and saturate the electronics, therefore has been attenuated during the calibration from μA to tens of pA by closing the slits, inserting apertures and defocusing it. The detector pressure has been adjusted to fully stop the ions along the first anode. The ^{9}Be peak in the energy spectrum has been fitted by a Gaussian (Figure 2.14), whose centroid has been taken as a measure of the mean pulse height. As it is shown in Figure 2.15, the output of the GIC for projectiles with energies ranging from 500 to 1400 keV follows a linear trend:

$$H = \alpha E + \beta \tag{2.14}$$

where H is the pulse height in ADC channels and E the beam energy in keV. α in channels/keV and β in channels are the fit parameters.

Taking the FWHM of the Gaussian fit as a measure for the detector energy resolution, a 1300 keV ^{9}Be peak presents a width of 34 keV. Contributions to the resolution are given by the electronics of the data acquisition system, the energy loss straggling in the entrance window and the fluctuations in the charge production and collection in the gas

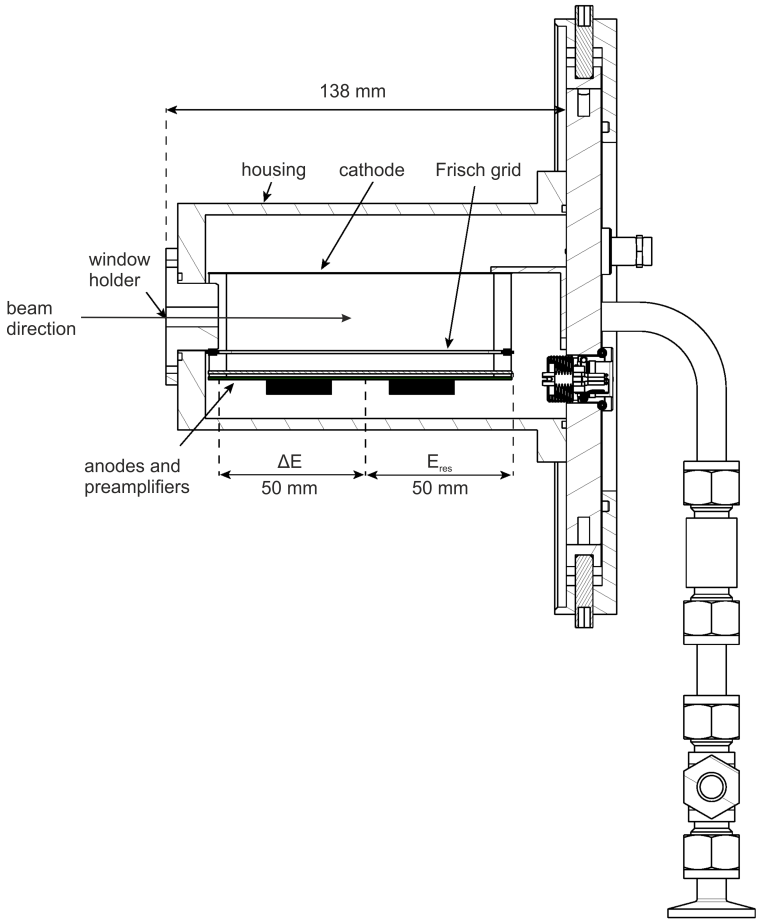

Figure 2.11: Schematic representation of the ETH detector.

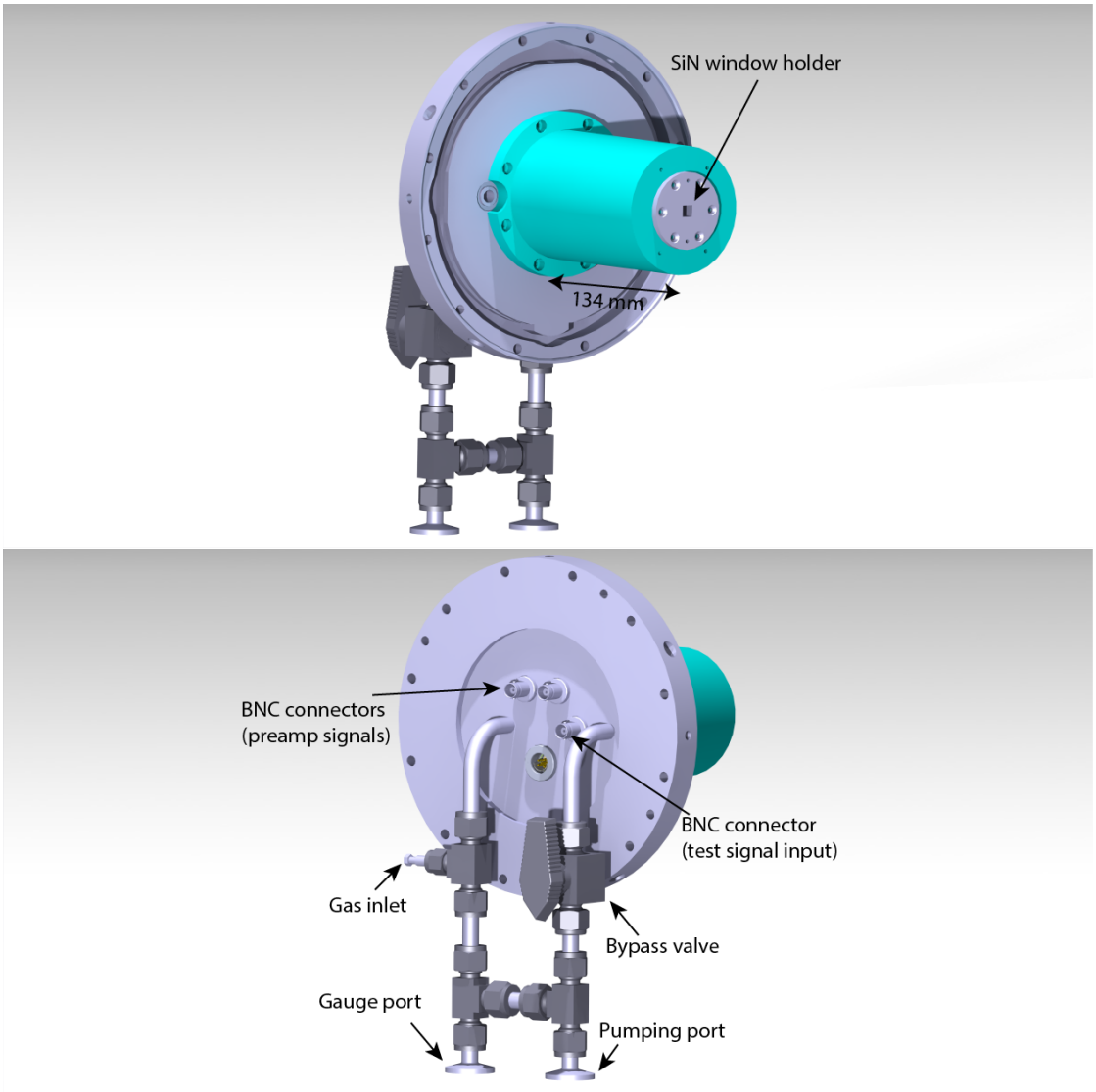

Figure 2.12: ETH detector front and back [46].

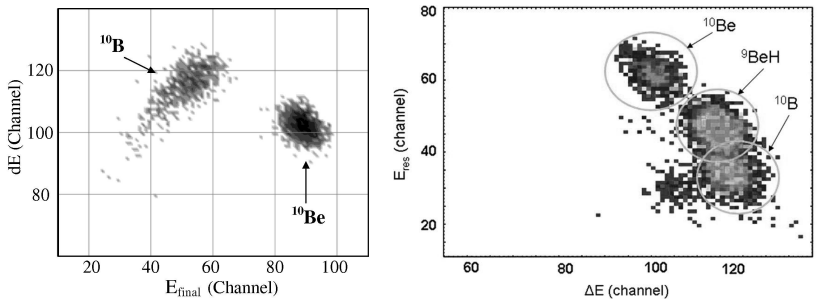

(a) With the degrader technique [13]. (b) With the BeF_2 technique [39].

Figure 2.13: Examples of two-dimensional spectra acquired at the SARA facility during ^{10}Be measurements with the original setup by adopting two different ^{10}B suppression techniques. An optimal detector resolution is essential to discriminate the elements entering the chamber.

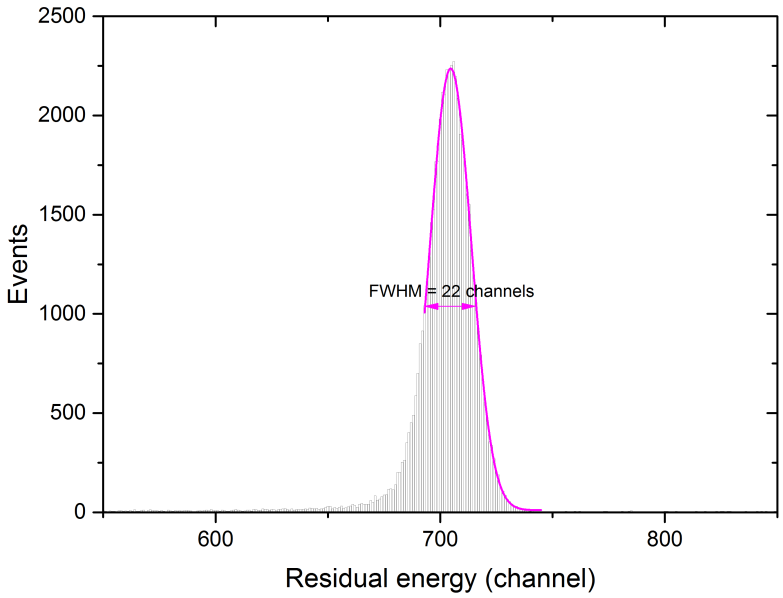

Figure 2.14: Energy spectrum of a 1300 keV ^{9}Be beam with the ETH detector. The GIC pressure has been set at 35 mbar, so that ions are fully stopped in the ΔE section. The Gaussian fit used to estimate the pulse height and the FWHM has been done discarding the the part below the lower half height of the distribution in order to avoid the influence of the low-energy tail on the fit.

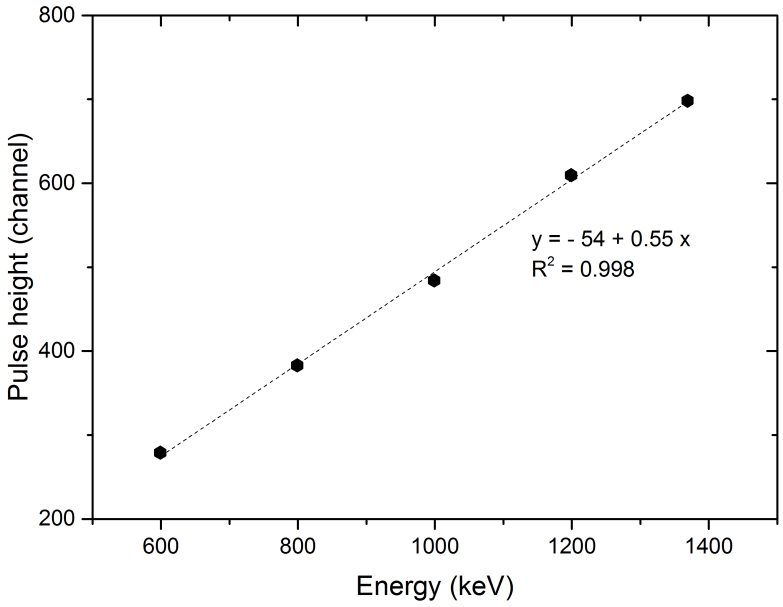

Figure 2.15: ^{9}Be energy calibration with the ETH GIC.

volume.

The contribution of the electronic noise has been estimated through a pulse generator coupled to the first anode preamplifier and amounts to 22 keV.

Energy straggling Ω caused by the passage through the silicon nitride entrance foil has been calculated according to the semi-empirical Sun's formula [47, 48]:

$$\frac{\Omega}{\Omega_B} = 2.532 \cdot \left[\frac{(E/A)^{3/2}}{Z}\right]^{0.2608} \tag{2.15}$$

where E is the projectiles' energy in MeV, A is the projectiles' mass, Z is the projectiles' atomic number and Ω_B is the Bohr's straggling [49]:

$$\Omega_B^2 = 4\pi Z^2 Z_t e^4 N t \tag{2.16}$$

being Z_t, N and t the atomic number, density and thickness of the target material, respectively. The straggling in the silicon nitride window is normally a minor contribution and depends on the foil thickness. However, it can be easily improved using a thinner membrane: for example, a 30 nm window, so far the thinnest available on the market,

would produce an energy straggling of just 7 keV contributing even less to the total resolution.

The contribution due to statistical fluctuations in the production and collection of charge in the detector gas has been estimated by subtracting the squares of the electronic noise and silicon nitride contribution from the square of the total resolution:

$$r_{gas}^2 = r_{tot}^2 - r_{noise}^2 - r_{foil}^2 \tag{2.17}$$

and amounts to 26 keV.

The different contributions to the resolution are summarized in Table 2.4, where they are compared with the ones estimated with the old setup following the same procedure. The total resolution (FWHM) of the ETH GIC is 6 keV lower than the previous one. This is consequence of the reduced contribution of the electronic noise, amounting to 22 keV, despite of the 29 keV measured with the old setup. The calculated energy stragglings caused by the detectors entrance windows slightly differ since the silicon nitride foils installed during the experiments had different nominal thicknesses. The contribution due to the charge production and collection is almost the same for the two detectors.

The resolution has been measured also for uranium ions following the same procedure just described for beryllium. A total energy resolution for 2.7 MeV uranium ions of 7% has been achieved with the ETH detector, against the 10% obtained with the HVEE design. The most likely explanation for this improvement is a more efficient charge

Table 2.4: Different contributions to the total resolution of a ^{9}Be beam at 1300 keV.

	Old setup	ETH GIC
FWHM (keV)	40	34
Electronic noise (keV)	29	22
Silicon nitride foil thickness (nm)	40	50
Silicon nitride foil straggling (keV)	8	9
Gas (keV)	26	25

collection in the first case as the resolution for heavy ions is conditioned by the charge production in the active area of the detector.

Chapter 3

Optimization of ^{26}Al Measurements

3.1 Introduction

^{26}Al is a cosmogenic radionuclide that decays to ^{26}Mg by positron emission:

$$^{26}_{13}Al \quad \rightarrow \quad ^{26}_{12}Mg + e^{+} + \nu_e \tag{3.1}$$

or electron capture:

$$^{26}_{13}Al + e^{-} \quad \rightarrow \quad ^{26}_{12}Mg + \nu_e \tag{3.2}$$

with a half-life of $(7.08 \pm 0.17) \cdot 10^5$ y (weighted average from [50]). This radionuclide is produced in extraterrestrial and terrestrial materials by spallation reactions in which Si is the primary target. ^{26}Al is an important tool to gain insights into several geological and astronomical processes, and its measurement is often combined with ^{10}Be for burial dating. The investigation of natural archives whose ^{26}Al derives from the atmosphere is very difficult, since the ^{26}Al produced by cosmic rays in the atmosphere has a very low production rate (3 orders of magnitude less than ^{10}Be), resulting in isotopic ratios ^{26}Al/^{27}Al which normally don't exceed the 10^{-14} level. Indeed, the stable ^{27}Al has an isotopic abundance of 99.9+% [51] and is prevalent in the environment where it constitutes about the 8% of the earth crust. The ^{26}Al is also produced in terrestrial rocks at a rate three times higher than ^{10}Be, which is sufficient to allow studies concerning

terrestrial surfaces processes: e.g. in quartz (SiO_2), where ^{27}Al content is low, isotopic ratios of up to 10^{-11} can be found. ^{26}Al is normally present in extraterrestrial material in rather elevate ratios. In this case, even if decay counting techniques could be used, the AMS is preferred as it requires much smaller samples. In addition to the research involving natural samples, ^{26}Al is also used for biomedical research as a tracer in organisms metabolism [52]. Typical atom ratios in this case are much higher, of up to 10^{-9}.

Typical ^{27}Al/^{26}Al ratios lie in the range $10^{-14} - 10^{-12}$. The ^{26}Al analysis is subjected to the interference of the stable isobar ^{26}Mg, whose isotopic abundance is 11.01% [51]. Magnesium constitutes the 2.3% of the earth crust, therefore its content in the samples is very high, even if a good chemistry is applied. This interference can be easily removed by the AMS technique, since the extraction of Al^- from the source eliminates the disturbing ^{26}Mg because magnesium does not form stable negative ions. Nevertheless, because of the aluminium low electron affinity, the yield of Al^- is considerably low, providing currents ranging from 100 to 500 nA. A long measurement is normally required to evaluate samples with a ^{27}Al/^{26}Al atom ratios at the level of 10^{-13}.

Even if the extraction of AlO^- from the samples provides currents of up to 3 μA, the MgO^- molecular ion readily forms resulting in ^{26}Mg rates of tens of MHz that completely overwhelms the counting capability of the GIC. The techniques adopted so far to suppress the intense ^{26}Mg flux from AlO^- currents are based on gas-filled magnets placed at the HE side of the AMS facility. When ^{26}Al and ^{26}Mg pass through the magnet, they interact with the gas ending up with an average charge state and trajectories which depends on the atomic number. So, they are spatially separated at the exit of the magnet. Unfortunately, this technique requires beam energies above 40 MeV [53, 54, 55], which are far higher than those available at SARA. A very promising ^{26}Mg suppression method utilizes laser photodetachment of the molecular anions outgoing the ion source and can be applied to isobaric systems where the interfering isobars have a smaller electron affinity than the isotope of interest. Using a laser with an energy in between the two electron affinities, the negative ions of the isobar can be selectively neutralized by

overlapping the ion beam with the laser beam [56]. Since the suppression takes place before the acceleration stage, it is independent on the terminal voltage and is in principle applicable also on compact AMS systems like SARA. However, further investigations are still necessary to improve the overall performance of this setup and make it reliable for routine ^{26}Al measurements [57].

The possibility of measuring ^{26}Al by AMS on the SARA facility was initially demonstrated during the acceptance tests carried out by HVEE on site [12, 13] and was followed by the subsequent optimization work carried out by the CNA AMS group [40]. The installation of the He stripper in 2015, however, required a new analysis of the transmission and the background for the most populated charge states at the exit of the accelerator. The effects of the He stripping on the ^{26}Al AMS has been previously investigated exclusively at terminal voltages below 600 kV [37]. The study of the SARA performance with the upgraded setup provides a useful insight of the mechanisms behind the He stripping process at terminal voltages between 600 and 1000 kV. These data are essential to find the optimal measurement settings for ^{26}Al AMS and represents a useful information also for other research groups operating with similar facilities.

3.2 Samples

The aluminum targets used for the experiments described in the following sections are based on Al_2O_3. The standard samples are produced at the Space Sciences Laboratory (SSL, University of California, Berkeley, USA) [50]; their nominal values are listed in Table 3.1. Al_2O_3 powder provided by Sigma-Aldrich (Sigma-Aldrich, St. Louis, USA) is used as a blank for background estimations. Standard and blank materials are thoroughly mixed with a metallic powder and pressed into Cu cathodes. From the previous study of the ionization efficiency of the ion-source it was demonstrated that Cu-mixed samples in an atom/atom proportion Al_2O_3:Cu 1:1 provide the highest and most stable currents (200-300 nA) [40].

Table 3.1: Standard samples used during the experiments. The uncertainty of isotopic ratio is $\sigma = \pm 1.2\%$ [50].

Name	Nominal ^{26}Al/^{27}Al ratio (10^{-11})
01-4-1	7.44
01-4-2	3.10
01-4-3	1.065

3.3 Effects of the He stripping

As it was already highlighted in the introduction, the extraction of Al^- from the ion source results in currents in the LE side Faraday cup of up to few hundreds nA. However, depending on the sample material and on the source performance, lower currents are not rare. In this case it is essential to optimize the measurement efficiency, which is mainly determined by the transmission through the tandem accelerator.

After the installation of the He stripper, the charge state distribution at the exit of the accelerator has been studied for different terminal voltages and stripper thicknesses. Between 500 and 1000 kV, the most populated charge states after the stripping process are 1+, 2+ and 3+. The transmission curves for ^{27}Al at the maximum terminal voltage are plotted in Figure 3.1. The He mass thickness of 0.06 μg/cm^2 corresponds to the end of the pre-equilibrium region and the beginning of the equilibrium of the yield distributions. The 1+ charge state is overpopulated relatively to the others in the pre-equilibrium region, reaching a maximum transmission of 38% at a stripper gas thickness of 0.01 μg/cm^2. Between 0.01 and 0.04 μg/cm^2, the 1+ transmission decreases, while the 2+ and 3+ yields still increase until reaching the maximal transmissions of 52% and 17% at 0.04 μg/cm^2, respectively. At higher He thicknesses the transmission of the three charge states decreases, but the equilibrium is reached just at 0.06 μg/cm^2, since from that point a further increase of the stripper pressure does not change the relative charge states distributions. Nevertheless, the absolute transmissions exponentially decrease because of

the scattering losses in the stripper channel, as it has been explained in Section 2.4.1.

The behaviour of the transmission curves measured as a function of the stripper thickness is rather unusual. As it is shown in Figure 2.5, the maximum transmission is normally present at the passage from the pre-equilibrium to the equilibrium region. In the case of ^{27}Al curves, the highest values lie in the pre-equilibrium zone, where an overpopulation is especially evident for the 1+ and 2+ charge states. The reasons behind such a behaviour are still not clear and require further investigations. However, a possible explanation might be represented by the presence of molecules that survive the stripping process and contribute to the current detected in the HE cup. This could explain why the 3+ charge state is less affected by this effect, since 3+ molecules are unstable and have less probability to go beyond the HE magnet. As a result, the transmission of the lower charge states (1+ and 2+) might be overestimated.

Population yields of 21%, 48% and 17% are calculated for the 1+, 2+ and 3+ charge states respectively by fitting the transmission data obtained at stripper thicknesses above 0.06 μg/cm^2. These values are consistent with the charge state yields estimated by Nikolaev et al. at a 910 keV stripping energy [58] (Figure 3.2).

In Figure 3.3, transmission values measured at different terminal voltages at a stripper thickness of 0.05 μg/cm^2 are represented. Such a He thickness ensures to work close the charge state distribution equilibrium region without relevant scattering losses. Transmission data recorded at the 600 kV Tandy facility are plotted for comparison. The transmission of the three charge states results almost constant in the energy range permitted by the SARA apparatus. At stripping energies below 600 keV, there is a good agreement between the transmissions measured at the SARA and the Tandy facilities, despite the different design of the stripper channels and the ion optics systems.

3.4 ^{26}Al low-energy AMS

The analysis of the effects of the He stripping on ^{27}Al ions is followed by a study of feasibility of ^{26}Al measurements. Several experiments are conducted for the purpose

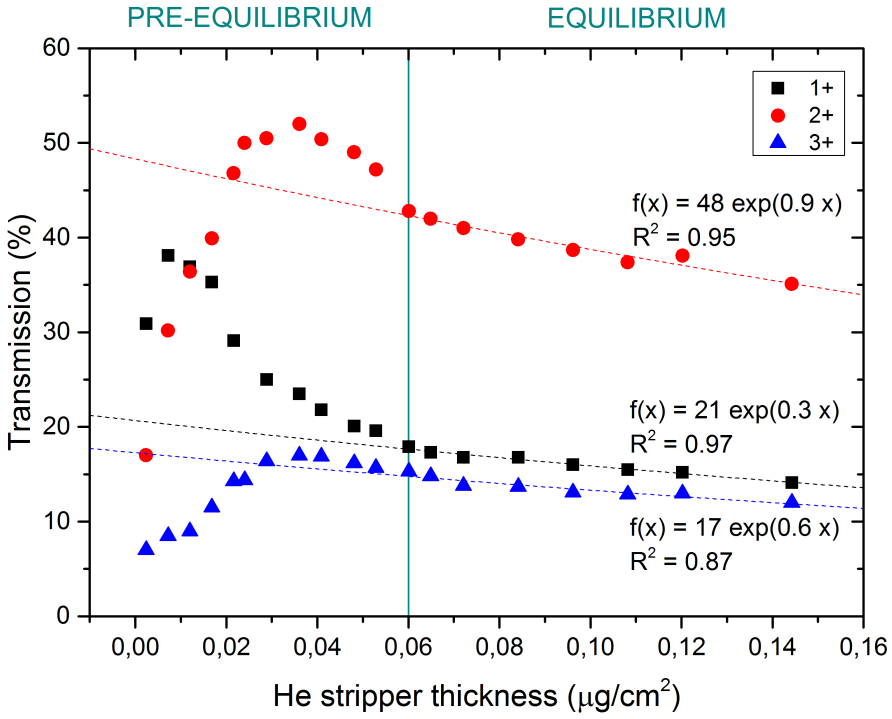

Figure 3.1: ^{27}Al transmission as a function of the He stripper thickness for the 1+, 2+ and 3+ charge states on the SARA facility at 1 MV terminal voltage.

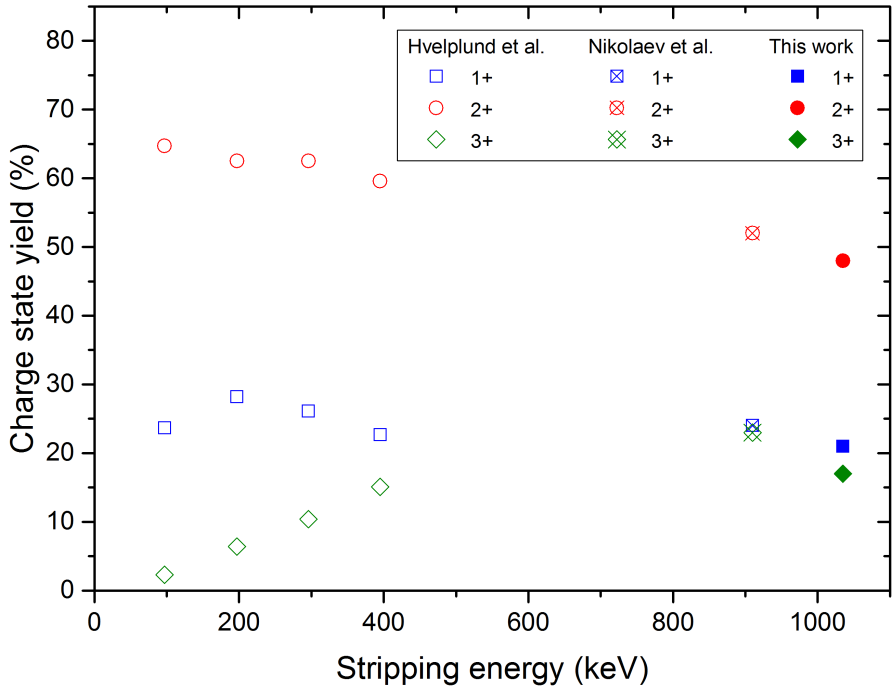

Figure 3.2: Comparison between the charge state yields reported in [58, 59] and the ones calculated in this work.

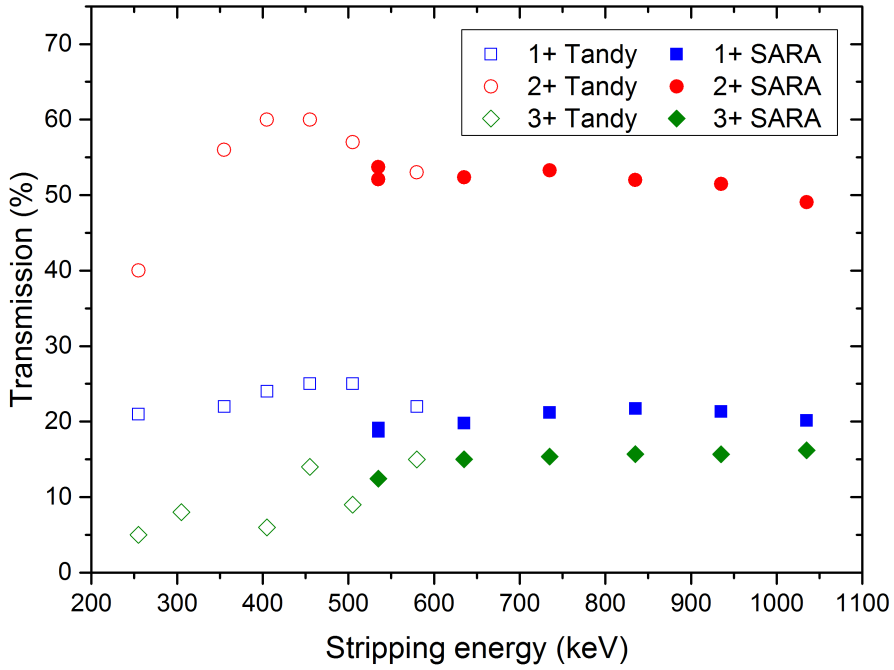

Figure 3.3: ^{27}Al transmission as a function of the terminal voltage for the charge states 1+, 2+ and 3+ at a stripper thickness of 0.05 μg/cm^2. Data recorded at the Tandy facility are represented for comparison [37].

of identifying the different background causes and minimizing them, at the same time keeping the efficiency as high as possible. The purpose of such a work is the definition of the optimal conditions for routine ^{26}Al measurements with the current SARA setup in the three most populated charge states available after the stripping process (1+, 2+ and 3+). Indeed, the origins of the backgrounds are different as well as the necessary techniques to reduce them. The results and issues related to each of the three charge states are described in the following sections.

3.4.1 The 1+ charge state

The 1+ charge state presents its maximum transmission at stripping energies between 700 and 1000 keV (Figure 3.3), corresponding to terminal voltages between 700 and 800 kV, but the ESA bending power allows to work at a maximum of about 700 kV, resulting in a beam energy after the accelerator of 1400 keV.

The suppression of 1+ molecules such as $^{13}C_2^{1+}$, $^{14}N^{12}C^{1+}$, $^{10}B^{16}O^{1+}$, $^{24}Mg^1H_2^{1+}$ and $^{25}Mg^1H^{1+}$ surviving the stripping process forces to increase the He thickness to values where substantial beam losses are present. In Figure 3.4, a scan over the stripper pressure shows that a full molecular suppression is possible at thicknesses above 0.14 μg/cm^2. In this region, the ^{26}Al transmission goes drastically to values below 14%.

Working with the 2-dimensional spectra can give a chance of measuring ^{26}Al at a lower stripper pressure, so with a higher beam transmission. Spectra of standard samples acquired at different stripper thicknesses are shown in Figure 3.5. At thicknesses above 0.09 μg/cm^2, molecules are not fully destroyed in the stripping process, but their count rate of hundreds of Hz can be handled by the electronics of the detector and ^{26}Al can be separated from the corresponding molecular fragment (Figure 3.5a). In this configuration, the $^{27}Al^{1+}$ transmission through the accelerator is 17%, ^{26}Al standard samples are measured close to their nominal values and the background is of few 10^{-13}.

Such a high background is caused by ^{25}Mg which is injected into the accelerator as $^{25}Mg^1H^-$ along $^{26}Al^-$. Charge exchange in the HE acceleration tube allows $^{25}Mg^{1+}$ to gain additional energy and pass the HE magnet. Following scattering processes at the

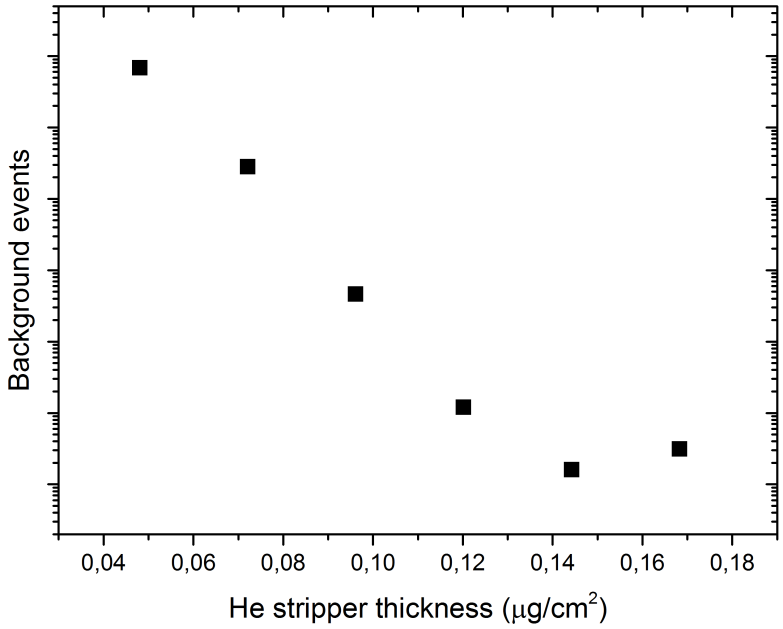

Figure 3.4: $^{26}Al^{1+}$ background as a function of the He stripper thickness. Molecular suppression is achieved at thicknesses above 0.14 μg/cm^2.

ESA walls, part of these ^{25}Mg ions reach the detector and enter the ^{26}Al gate resulting in background events.

3.4.2 The 2+ charge state

The 2+ charge state transmission is almost constant in the studied energy range (from 500 to 1000 kV) and is more than twice higher than the 1+ and 3+, as shown in Figure 3.3. Therefore, the 2+ charge state would seem the most appropriate for ^{26}Al measurements.

In general, conventional ^{26}Al AMS require the employment of an odd charge state independently of the terminal voltage. If an even charge state such as $^{26}Al^{2n}$ is selected, intense counting rates of $^{13}C^{n}$ from the injection and subsequent break-up of the $^{13}C_2^-$ molecular ions are observed. These ions have the same kinematic properties as $^{26}Al^{2n}$ (e.g. the E/q and mE/q^2 ratios) and therefore pass both the magnetic and electric analyzers. C is a very abundant element, having C13 an isotopic abundance of 1% [51]. It is present in the samples and in the source components and,therefore, cannot be avoided.

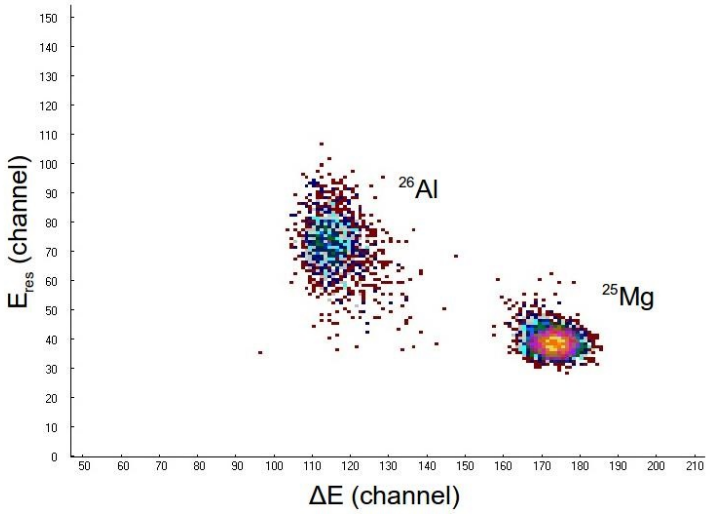

(a) Stripper thickness: 0.09 μg/cm^2.

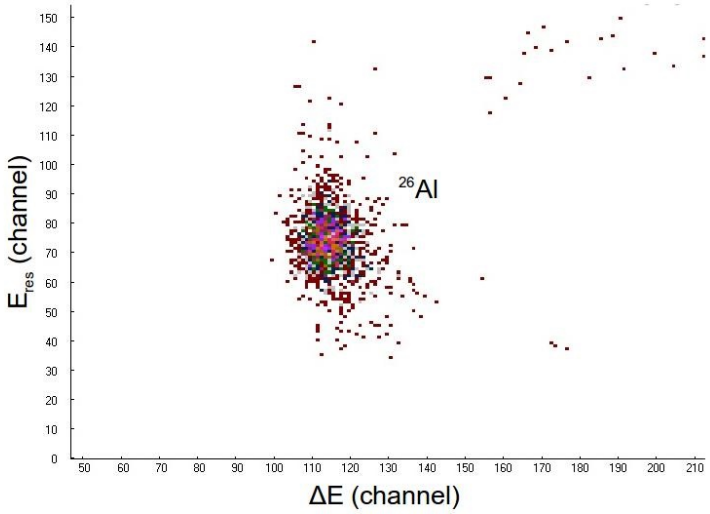

(b) Stripper thickness: 0.14 μg/cm^2.

Figure 3.5: ^{26}Al spectra of a standard sample in the 1+ charge state at different stripping pressures.

Therefore, the intense interference caused by $^{13}C^{1+}$ does not make $^{26}Al^{2+}$ detection possible in the conventional way at SARA. $^{13}C_2^-$ molecules are extracted from the samples and, since they have mass of 26 u, are selected by the LE magnet arriving to the stripper channel. $^{13}C^{1+}$ ions resulting from the stripping process are able to pass through the HE filters and reach the detection system where they could be separated taking advantage of their different energy. However, their count rate is so high to saturate the electronics and for this reason, ^{26}Al has been always measured with the conventional setup in either the 1+ or 3+ charge state [40].

The studies presented in [37, 60] demonstrated that ^{26}Al measurements in the 2+ charge state are feasible at energies below 1550 keV by adopting proper interference suppression techniques for ^{13}C. Following the promising results highlighted in these works, the so-called passive absorber technique was tested at the upgraded SARA facility; results will be deeply discussed in the dedicated Section 3.5.

3.4.3 The 3+ charge state

As shown in Figure 3.3, the 3+ transmission increases with the beam energy, so the background is studied at the maximum terminal voltage, 1 MV. Molecular background is not important in this case since molecules are unstable in the 3+ charge state and most of the corresponding molecular fragments are removed by the HE spectrometer. Therefore, the stripper thickness of 0.04 μg/cm^2, which corresponds to the maximum transmission, can be set. In this configuration, the transmission through the accelerator is about 17%, the standard samples are measured close to their nominal value and a background level of few 10^{-14} is measured. Acquired spectra are really clean and there is almost no need of inserting slits in the beam path to improve the background/transmission ratio. A typical $^{26}Al^{3+}$ monodimensional spectrum is shown in Figure 3.6.

The memory-effect in the ion source has been identified as one contribution to the background. Some events, indeed, are recorded when a blank sample is measured after running ^{26}Al targets for a long time. In Figure 3.7, the evolution of the background after a 2 h of sputtering of a high-level standard (01-4-1, Table 3.1) is represented. The number

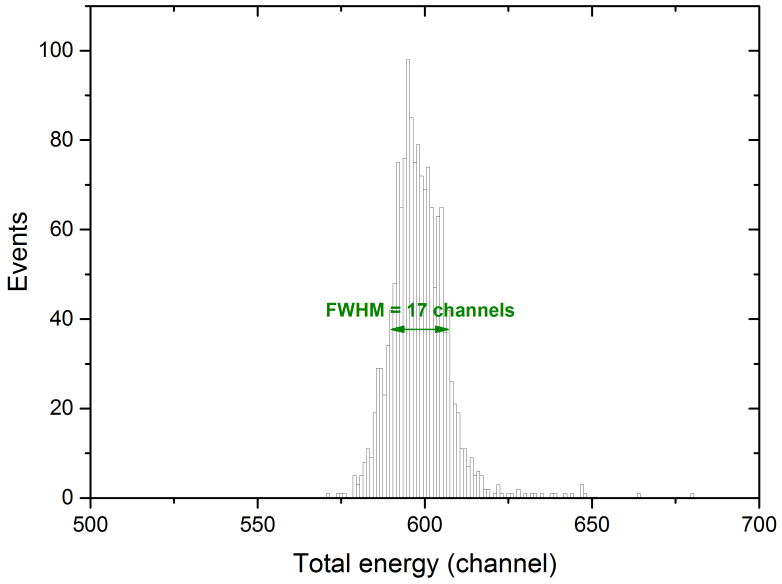

Figure 3.6: Example of an acquired total energy spectrum of ^{26}Al for a standard sample in the 3+ charge state.

of recorded events decreases during the first 30 min of measurement and then stays quite constant, proving ^{26}Al contamination in the source during the ions extraction from the standard, and indicating a progressive source cleaning during the blank measurement. To further demonstrate the occurrence of this phenomena, the background is estimated just after measuring a high-level standard for a progressively increasing time, from 1 min to 2 h. As illustrated in Figure 3.8, the background ratio slightly increases with the standard measurement duration, showing the influence of the ion source memory-effect.

This background source has to be taken into account during the measurements, where samples, standard and blank targets are alternated. As a precaution, a low-level standard has to be chosen, in order to contaminate as less as possible the ion source during its estimation. Furthermore, before estimating background and real samples ^{26}Al/^{27}Al ratios, some time has to be dedicated to clean the source with a blank or with a material with nominally no ^{26}Al content.

The memory-effect contributes to ^{26}Al background of all the charge states selected at the exit of the accelerator. However, its contribution is too low to be relevant in the 1+

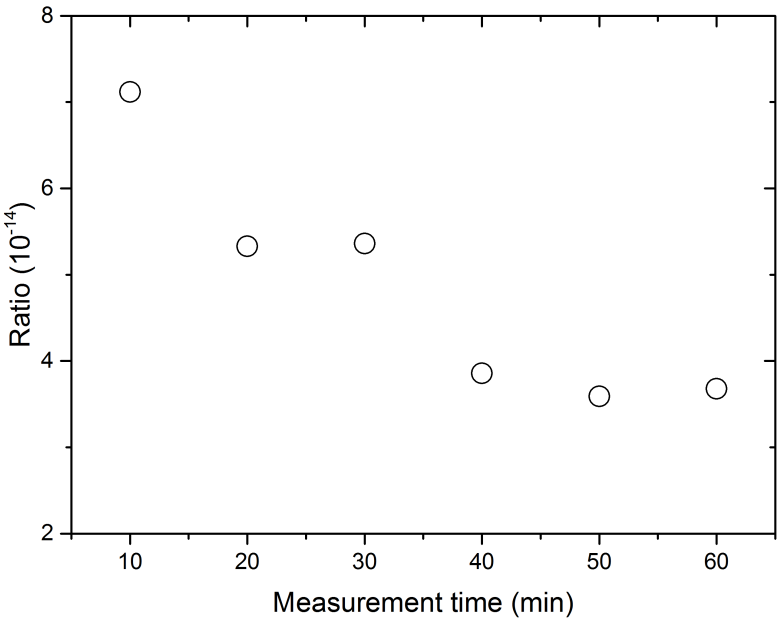

Figure 3.7: Evolution of a blank sample after measuring the 01-4-1 standard for two hours.

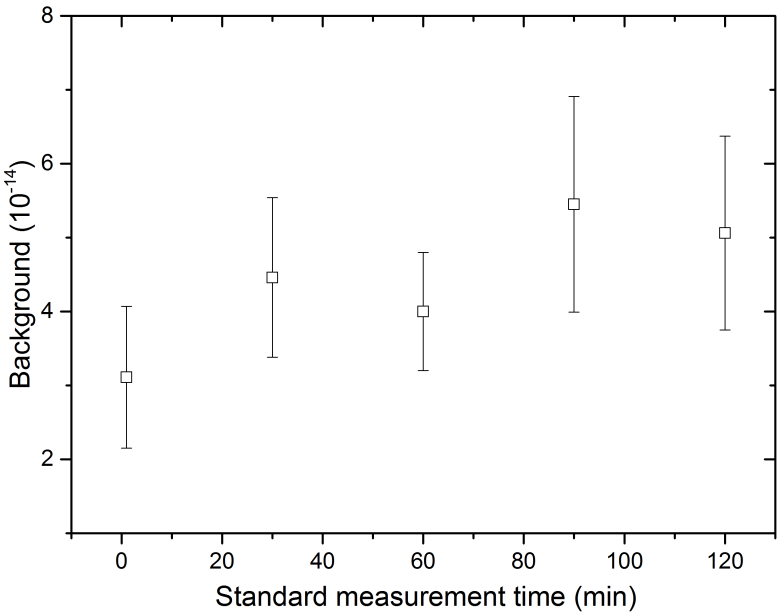

Figure 3.8: Effect of the cross-talk on the background levels. On the x-axis: standard measurement duration; on the y-axis: background ratio estimated for one hour.

charge state, whose background is at the level of 10^{-13} because of ^{25}Mg reaching the detector following dispersive processes in the HE side of the facility. Charge exchange phenomena which cause the ^{25}Mg energy gain in the HE acceleration tube and allow its selection by the HE magnet are less probable in the 3+ than the 1+ charge state.

In conclusion, having a lower background level than the 1+ and the same transmission, the 3+ charge state is evidently more suitable for routine measurements.

3.5 The Passive Absorber Technique

The high transmission of the 2+ makes this charge state worth of further investigations. However, to work with the 2+ charge state and benefit of its high transmission, ^{13}C interference has to be removed. This can be done by applying the so-called passive absorber technique.

A passive absorber takes advantage of the different ranges of ions in matter, and consists in an absorber material placed in front of the final detection system, a GIC in our case. The absorber must have a thickness high enough to stop the disturbing ions but to let the isotope of interest reach the active volume of the detector. This technique is applicable to suppress $^{13}C^{1+}$ during the $^{26}Al^{2+}$ detection, since ^{13}C ions carry half of ^{26}Al energy, for which their range is significantly lower.

The passive absorber technique was originally applied to achieve ^{10}B suppression during ^{10}Be measurements at AMS systems operating at 6 MV [61] and it is conventionally used at terminal voltages above 3 MV for ^{10}Be measurements [62, 63].

At lower energies, the energy and range stragglings worsen the separation between the investigated isotope and its interference, therefore the passive absorber technique could not be used until the development of high-resolution gas ionization chambers. The promising results described in [37, 60] with an ETH gas ionization chamber at the Tandy facility (600 kV terminal voltage) encouraged to install and test a passive absorber also at SARA not only for $^{26}Al^{2+}$ measurements, but also for ^{10}Be analysis. The setup of the absorber used at our facility is introduced next, together with the ^{26}Al results. ^{10}Be

results will be presented in the dedicated Chapter 4.

^{26}Al tests with the absorber setup have been carried out at the SARA system at a terminal voltage of 700 kV, corresponding to the highest $^{27}Al^{2+}$ transmission (Figure 3.3). Therefore, the ^{26}Al beam arrived to the absorber cell carrying an energy of 2100 keV. For this reason, all the simulations have been done assuming a 2100 keV ^{26}Al beam energy.

3.5.1 Absorber Setup

The most important feature of a passive absorber is its homogeneity, which is particularly critical when using foils at low beam energies. At terminal voltages above 3 MV, absorbers are traditionally based on havar [61, 64], titanium [65] or mylar ($C_{10}H_8O_4$) [66] foils. Havar and titanium have also the advantage to be almost H-free, which reduces protons background during ^{10}Be measurements. This effect will be deeply discussed in Chapter 4.

The foils manufactured with the above listed materials cannot be used at lower terminal voltages for two reasons: (i) their minimum mass thicknesses commercially available don't fit well for low-energy purposes, and (ii) they don't possess sufficient homogeneity to allow a reasonable separation between the investigated isotope and the interference. After the introduction in the market of the silicon nitride foils, they were rapidly adopted in several absorber setups at both high [67, 68] and low energies [37, 60], as the excellent homogeneity and the availability of thicknesses, from about 30 to several hundreds nm, make these membranes more suitable than the other materials. The criticality of the minimum mass thickness of the absorber foils for low beam energies is highlighted in Table 3.2, where the SRIM estimation of the energy loss suffered by a 2100 keV ^{26}Al ions passing through the considered materials is also reported.

Another factor plays a role in the choice of an absorber. Even if SRIM simulations can provide an estimate of the energy losses in the absorber material, an easy and fast change of the absorber thickness is preferred, specially during tests when fine adjustments are often required.

Table 3.2: Minimum mass thickness of the most common commercial foils used as absorbing materials. The energy loss of the 2100 keV ^{26}Al beam in the thinnest membrane according to SRIM simulation is reported.

Commercial name	Material	Minimum mass thickness (μg/cm^2)	^{26}Al energy loss in the thinnest foil[a] (keV)
havar	cobalt alloy[b]	33.2 [69]	122
titanium	Ti	4.5 [69]	23
mylar	$C_{10}H_8O_4$	0.7 [69]	6
silicon nitride	$Si_3N_{3.1}H_{0.06}$	0.1 [70]	0.7

[a] At a beam energy of 2100 keV.

[b] Nominal composition: cobalt (41-44%), chromium (19-21%), nickel (12-14%), tungsten (2.3-3.3%), molybdenum (2-2.8%), manganese (1.35-1.8%), carbon (0.17-0.23%) beryllium (0.02-0.08%) and iron (balance).

Taking into account all these factors, the passive absorber chosen for the experiments at the SARA facility is a combination of silicon nitride foils and a gas volume. It consists in the modified entrance holder for the gas ionization chamber sketched in Figure 3.9. With this absorber design, the incoming beam passes through a first silicon nitride window, a gas volume and a second silicon nitride foil before reaching the sensitive area of the detector (Figure 3.10).

The first silicon nitride foil separates the absorber/GIC gas from the rest of the beam line, which is at a high vacuum pressure (about 10^{-7} mbar). A 500 nm thickness and a 5x5 mm^2 area make the membrane able to withstand a pressure difference of 500 mbar; being so thick, on the one hand it is responsible for an initial beam energy reduction and on the other hand allows to work with a wide range of absorber gas pressures. The absorber volume between the two silicon nitride foils has a length of 16 mm and is connected to the detector via a hole with a 1 mm diameter, thus the absorber cell and the GIC are filled with isobutane (C_4H_{10}) gas at equal pressure. The interference should be completely stopped inside the absorber volume, therefore an accurate setting of the gas pressure is fundamental. The second silicon nitride foil has a thickness of 75 nm, an area of 5x5 mm^2 and prevents the charge created into the absorber to reach the sensitive

detector volume.

3.5.2 SRIM Simulations

To have an idea of the feasibility of this technique at the SARA facility, ^{26}Al and ^{13}C ions behaviour into the absorber have been simulated with the SRIM software [71]. At a terminal voltage of 700 kV, ^{26}Al and ^{13}C arrive to the absorber with energies of 2100 and 1050 keV, respectively. Residual energies of these ions traveling through the absorber length are plotted in Figure 3.11. In this simulation, an absorber/GIC gas pressure of 30 mbar is supposed. The most of the ^{13}C ions is suppressed by the absorber, but a small fraction can still reach the detector. The energy difference between the ^{13}C and ^{26}Al ions that enter the chamber is sufficiently high to permit a discrimination between these isotopes. However, depending on the intensity of the interference (i.e. on the carbon content in the samples), the application of a higher absorber pressure might be needed to further stop ions along the absorber.

In Figure 3.12, the fraction of ^{13}C ions passing beyond the absorber is plotted against of the isobutane pressure, representing an estimation of the carbon suppression factor. According to this simulation, pressures above 30 mbar should completely stop ^{13}C inside the absorber cell. Since in this setup absorber and detector are connected, a gas pressure of 30 mbar estimated to stop the interference in the absorber makes ^{26}Al to stop along the first anode. Therefore, only that anode can be used to identify the particles arriving into the active area of the detector.

Figure 3.13 presents a visual representation of ^{26}Al and ^{13}C ions behaviour into the absorber. With an isobutane pressure of 40 mbar, ^{13}C ions are fully suppressed whereas ^{26}Al ones reach the active volume of the gas ionization chamber. The first silicon nitride foil causes a wide angular straggling in the beam, which is critical for ^{26}Al ions because part of them does not fulfill the acceptance of the second foil and cannot reach the detector. According to the simulation, the spatial distribution of the ^{26}Al beam at the second foil in the plan which is transversal to the movement axis is characterized by an angular dispersion $\sigma \approx 400$ mrad. Thus, some losses are inevitable in the 5x5 mm^2

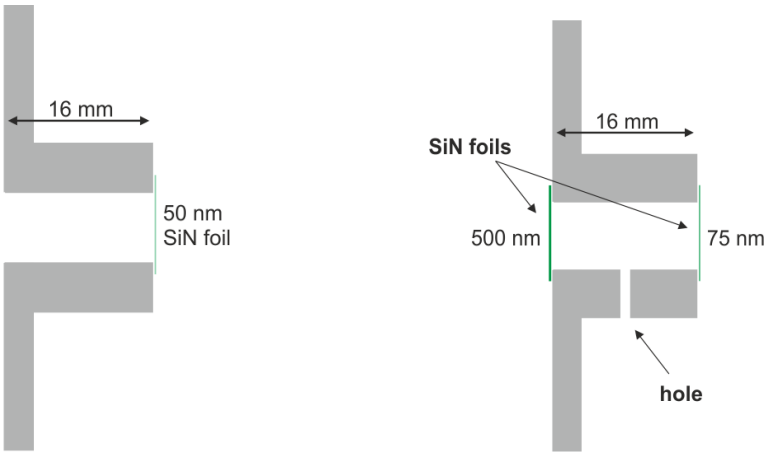

(a) Conventional holder for the detector entrance window.

(b) Modified holder for the absorber setup.

Figure 3.9: The modified GIC window holder used as a passive absorber.

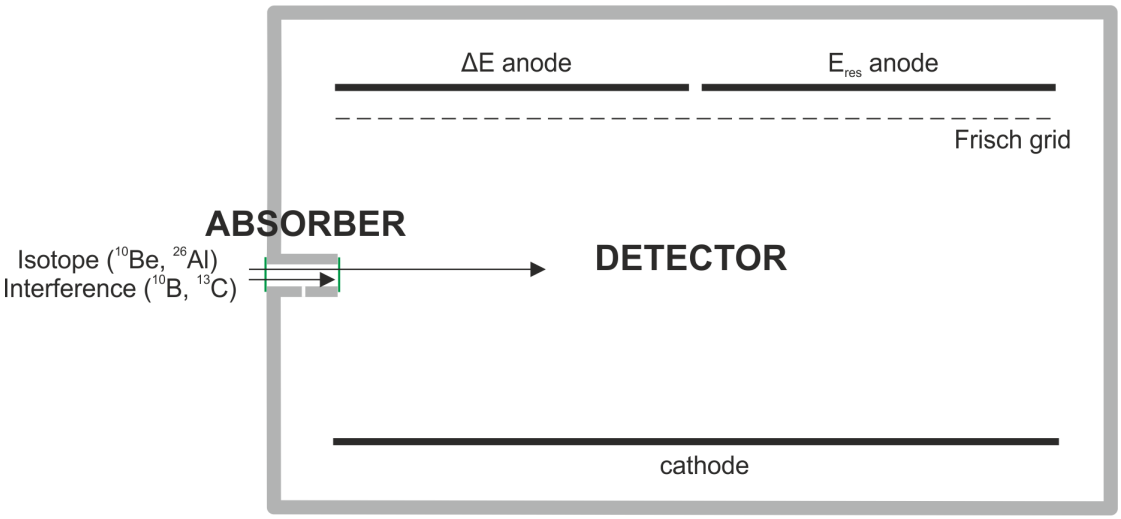

Figure 3.10: Sketch of the absorber setup.

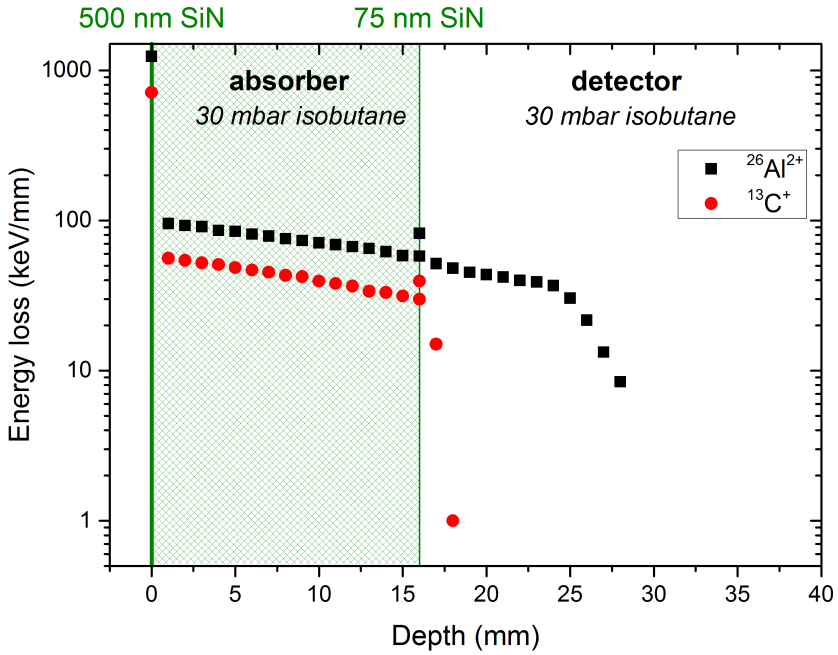

Figure 3.11: SRIM simulation of the residual energy of 2100 keV ^{26}Al and 1050 keV ^{13}C ions in the absorber/GIC setup.

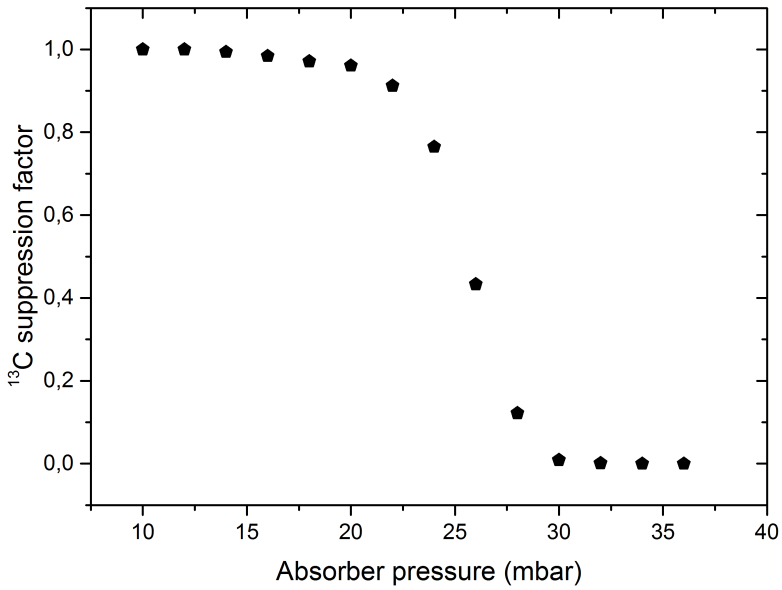

Figure 3.12: ^{13}C suppression factor at different absorber pressures according to SRIM simulations.

silicon nitride foil separating the absorber gas volume from the detector, whose angular acceptance amounts to 155 mrad. A transmission of less than 40% through the absorber cell is this way roughly estimated.

3.5.3 $^{26}Al^{2+}$ Detection with the Passive Absorber

The experiments with the absorber cell have been done at a terminal voltage of 700 kV (i.e. 2100 keV $^{26}Al^{2+}$ beam energy) since the transmission through the accelerator is maximum (Figure 3.3).

Like in the 1+ charge state, an interference is represented by molecules of mass 26 u which can pass through the HE spectrometer in the 2+ charge state if the stripper pressure is not high enough to destroy them. The 26 u molecules that can reach the detector are listed in Table 3.3, where also the energies of each molecular fragment after the break-up in the first absorber foil are reported. Symmetric breakups as C, N, B or O carry a kinetic energy similar to ^{13}C and are completely stopped into the absorber. The problem arises with $^{24}MgH_2$ and ^{25}MgH, since the Mg molecular fragments pass the absorber and, according to SRIM simulations, enter the detector with energies of 50 and 70 keV, respectively, which are similar to the one of ^{26}Al (40 keV). As explained before, this absorber setup forces to work in the first anode, where $^{24,25}Mg$ molecular fragments and ^{26}Al cannot be discriminated. Therefore, a complete molecules dissociation during the stripping process is essential, which can be achieved at He thicknesses above 0.1 $\mu g/cm^2$, as it is demonstrated by the stripper scan in Figure 3.14.

By applying a stripper thickness of 0.12 $\mu g/cm^2$, the transmission through the accelerator is $\sim 38\%$. With an absorber/GIC pressure higher than 30 mbar, the $^{13}C^{1+}$ and $^{26}Al^{2+}$ peaks can be clearly separated and identified in the acquired spectra, as it is shown in Figure 3.15. An isobutane pressure of 40 mbar allows a complete $^{13}C^{1+}$ ions suppression.

In this configuration, a transmission of 55% in the absorber cell is measured (calculated according to Formula 2.5), meaning that the overall efficiency is about 22%, with a $^{26}Al/^{27}Al$ background atom ratio of $3 \cdot 10^{-13}$.

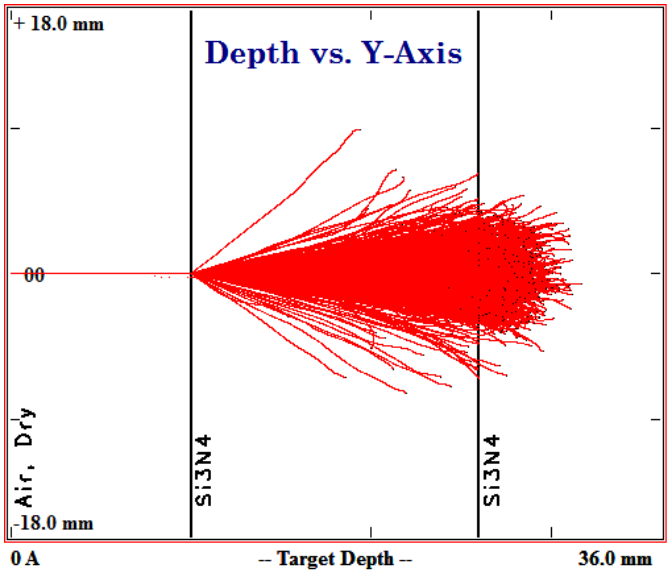

(a) ^{26}Al ions (E = 2100 keV)

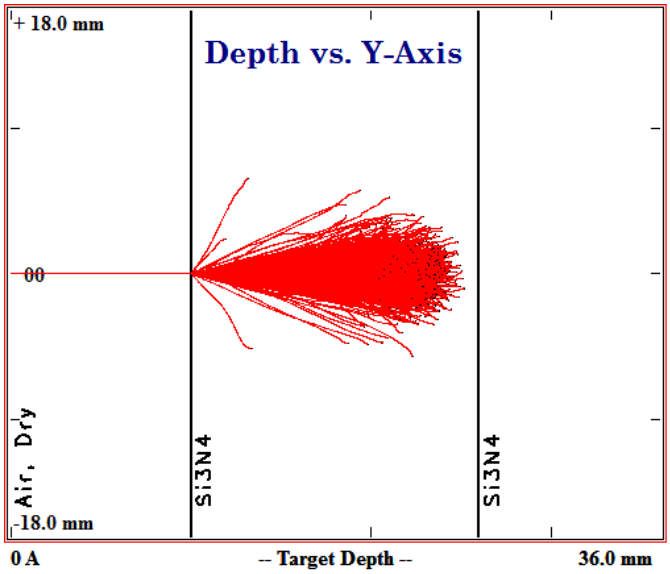

(b) ^{13}C ions (E = 1050 keV)

Figure 3.13: SRIM simulations of the ^{26}Al and ^{13}C ions behaviour into the absorber. By applying a 40 mbar isobutane pressure, ^{13}C ions are fully stopped into the absorber, whereas ^{26}Al ones can reach the detector volume.

Table 3.3: 26 u molecules that can reach the absorber setup if the stripping thickness is not sufficiently high. The energy after the break-up in the first absorber foil is reported for every fragment. According to SRIM, just ^{24}Mg and ^{25}Mg can enter the detector if the absorber gas pressure is set at 40 mbar.

Molecule	Fragment	Energy after breakup (keV)	Residual energy (keV)
$^{13}C_2$	^{13}C	1050	-
$^{10}B^{16}O$	^{10}B	808	-
	^{16}O	1292	-
$^{14}N^{12}C$	^{14}N	1131	-
	^{12}C	969	-
$^{24}MgH_2$	^{24}Mg	1939	48
	H	81	-
^{25}MgH	^{25}Mg	2019	73
	H	81	-

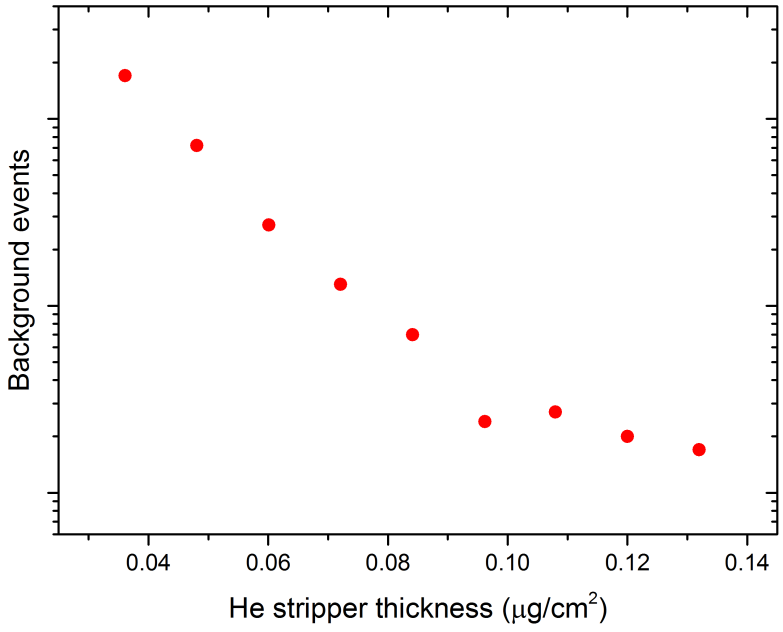

Figure 3.14: $^{26}Al^{2+}$ background as a function of the He stripper thickness.

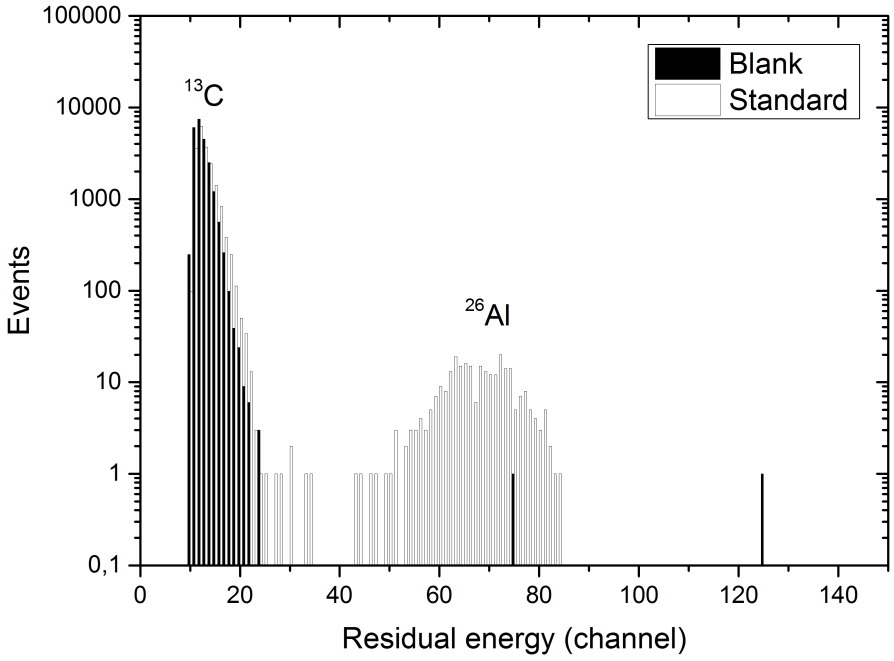

Figure 3.15: $^{26}Al^{2+}$ with the absorber setup. The absorber pressure of 38 mbar allows part of the ^{13}C ions to access the detector.

Three different background sources can be identified: (i) the memory-effect in the ion source, (ii) 26 u mass molecules surviving the stripping process and (iii) pile-up signals caused by $^{13}C^{1+}$. As clearly demonstrated with the 3+ charge state, the ^{26}Al background is influenced by the history of the ion source, specially when samples with high ratios are measured. The memory-effect (i) is independent on the charge state, thus it affects the 1+, 2+ and 3+ backgrounds. The contribution (ii) concerns the magnesium hydride molecules ($^{24}MgH_2$ and ^{25}MgH) that survive the stripping process and reach the detecting system. Even if the applied stripper thickness should ensure full molecular destruction, some molecules can survive the stripping process and originate background events in the detector. The contribution (iii) is strictly related with the passive absorber technique: indeed, if the absorber thickness is not sufficient to completely suppress the interfering ions, the elevate ^{13}C count rate can result in pile-up events produced by the electronics of the detector. These events appear in the energy spectrum extending toward higher channels, arriving some of them at the ^{26}Al gate.

The energy of the ^{26}Al ions entering the detector active volume can be easily changed by modifying the absorber gas pressure. The residual energy can be estimated by using a calibration of ΔE section of the gas ionization chamber done without the absorber with an attenuated ^{27}Al beam at different known energies (Figure 3.16). In Figure 3.17, the ^{26}Al residual energy measured at different absorber thicknesses is plotted and compared with SRIM calculations, showing a large discrepancy between the experimental data and the simulations: indeed, the measured energy after the passage through the absorber is significantly higher than predicted by the SRIM software. Also, the transmission through the absorber cell is underestimated by SRIM, since a 55% transmission is measured against the simulated 40%. Such a difference could be caused by an inaccurate knowledge of the absorber thickness (e.g. foils thicknesses, pressure measurement) or by an incorrect GIC calibration. Nevertheless, a similar effect has been detected at the Tandy at a slightly lower beam energy [60]. This suggests a possible underestimation of the residual energies and the angular straggling by the SRIM software when the simulations are relatively close the Bragg peak.

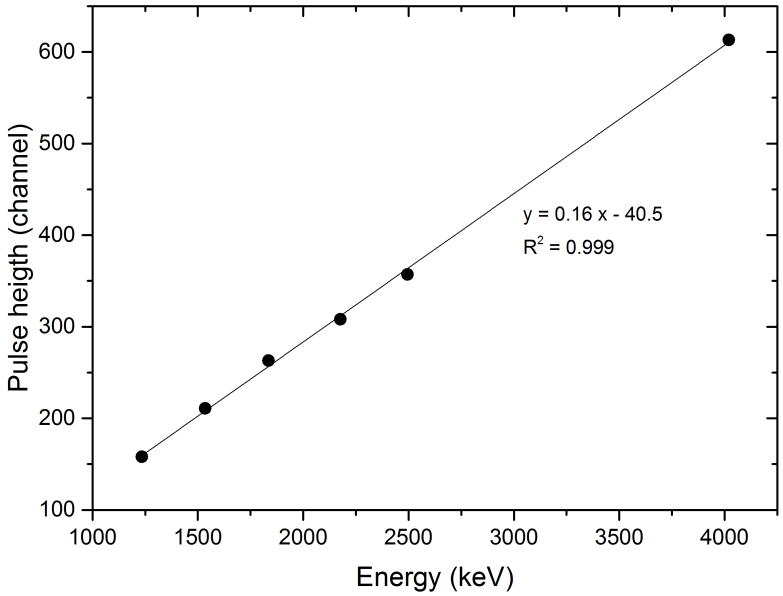

Figure 3.16: GIC calibration with ^{27}Al ions.

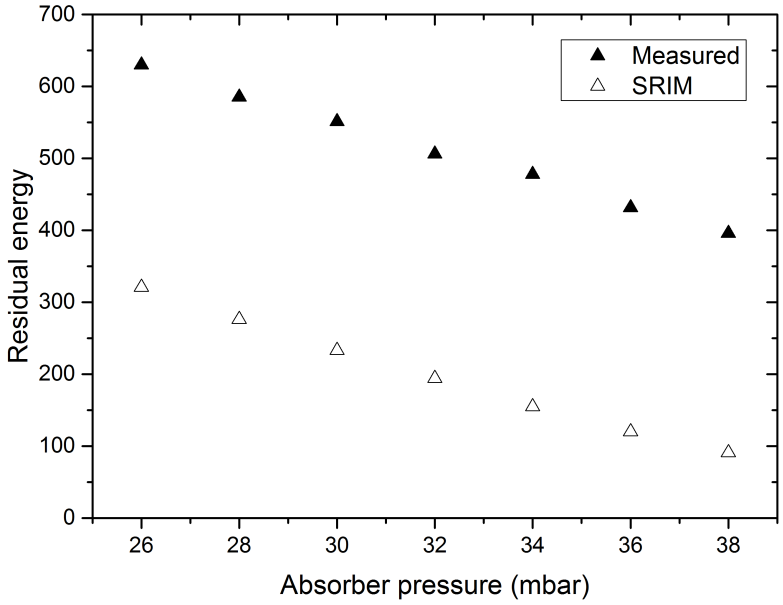

Figure 3.17: Residual energy of a 2100 keV ^{26}Al beam as a function of the absorber pressure compared with the SRIM calculations.

Absorber Setup Optimization

The design of the passive absorber device can be easily modified to obtain higher transmissions. In the tested setup, beam losses are caused by the angular straggling inside the absorber cell and specially by the very thick first foil. Therefore, a thinner membrane can be used instead of the 500 nm one to reduce the ions angular straggling and drastically improve the setup performance. For instance, if a 100 nm silicon nitride foil were used, the SRIM simulations predict a complete ^{13}C suppression at a gas pressure of $\sim$ 50 mbar, with a ^{26}Al transmission above the 90%. Taking into account that some discrepancies can be present between the SRIM calculations and the real absorber gas pressure needed to suppress ^{13}C, a 100 nm foil with an area of 5x5 mm^2 can be chosen, since it withstands a pressure difference up to 100 mbar and allows to work in a wide applicable pressure range.

Furthermore, the transmission through the absorber can be improved by using a second silicon nitride foil with a larger area, as demonstrated by the experiments realized at the Tandy facility with a 1550 keV $^{26}Al^{2+}$ beam [37, 60], where a 8x8 mm^2 membrane was used.

In principle, even if these two small modifications to the absorber design did not have been tested for lack of time, they would considerably enhance the efficiency of ^{26}Al measurements, without deteriorating the background.

3.6 Conclusions

The 1+, 2+ and 3+ are the most populated ^{26}Al charge states available after the He stripper in the energy range that can be reached at the SARA facility. In principle, measurements are possible in the three cases with the transmission and background values summarized in Table 3.4. Nevertheless, the 3+ results the best choice given the low ^{26}Al/^{27}Al ratios associated to environmental samples. Furthermore, it can be measured with the conventional setup (i.e. no absorber cell is necessary), which makes the routine work easier.

Table 3.4: Measurement parameters for ^{26}Al in the 1+, 2+ and 3+ charge states at the upgraded SARA facility. Reported background have an error σ = 20%.

Charge state	1+	2+	3+
Terminal voltage (kV)	700	700	1000
Energy (keV)	1435	2135	4035
He stripper thickness ()	0.09	0.1	0.04
Transmission accelerator (%)	17	40	17
Transmission GIC (%)	98	55 (absorber)	98
Overall efficiency (%)	17	22	17
Background	$2 \cdot 10^{-13}$	$3 \cdot 10^{-13}$	$2 \cdot 10^{-14}$

In the case of ^{26}Al measurements, the overall performance of the facility suffered a worsening after the installation of the He stripper. In Table 3.5, the transmission and background for Ar [40] and He stripping gases are reported. The measurement parameters drastically deteriorated in the 1+ charge state passing from Ar to He stripping, since the transmission reduced (from 25% with Ar to 17% with He) and the background increased of one order of magnitude (from $3 \cdot 10^{-14}$ to $3 \cdot 10^{-13}$). However, the 3+ transmission increased from 10% with the Ar stripper to 17% with He, whereas the background did not substantially change.

Routine measurements were carried out with the Ar stripper in the 1+ charge state, therefore with a 25% transmission and a ^{26}Al/^{27}Al background ratio of few 10^{-14}. With the He stripper, samples are measured in the 3+ charge state, which has the same background but a 30% less transmission than $^{26}Al^{1+}$ with the Ar stripping. In conclusion, the stripping with He gas did not bring any benefit to ^{26}Al AMS at low energies and actually reduced the measurement efficiency.

However, in a multi-elemental facility like SARA, He stripping is extremely convenient for heavy ions. The installation of a double stripper would be optimal, so that it would be possible to change from Ar to He at the occurrence. The conversion of the single

stripper actually used at SARA to a double one is very expensive and not scheduled in the short term. The measurement efficiency might be easily increased with the He stripper by applying the passive absorber technique, which gives a chance to detect ^{26}Al in the charge state 2+, which is characterized by a very high transmission through the accelerator. The preliminary experiments described in the previous sections demonstrate that the high-resolution ETH gas ionization chamber equipped with a absorber cell perfectly solves the 2100 keV $^{26}Al^{2+}$ and 1050 keV $^{13}C^{1+}$ peaks. However, even if the absorber design can be easily modified to allow a higher efficiency, further studies are necessary to reduce the ^{26}Al/^{27}Al background ratios to levels of $10^{-15} - 10^{-14}$ required by the AMS samples.

Table 3.5: Comparison between the transmission and the background for the different charge states with He and Ar stripping gases.

Stripping gas	Charge state	Transmission (%)	Background (10^{-14})
Ar	1+	25	3
	3+	10	2
He	1+	17	20
	3+	17	2

Chapter 4

Optimization of ^{10}Be measurements with the SARA facility

4.1 Introduction: ^{10}Be LE-AMS

After ^{14}C, ^{10}Be is the most measured radionuclide through the AMS technique due to its applications in environmental sciences and geology. This cosmogenic radionuclide is mainly created in the atmosphere and in the lithosphere and decays with a half-life of $(1.36 \pm 0.07) \cdot 10^6$ y [72] via β^- emission to stable ^{10}B through the reaction:

$$^{10}_{4}Be \quad \rightarrow \quad ^{10}_{5}B + e^- + \overline{\nu_e} \tag{4.1}$$

In the atmosphere, the major production of ^{10}Be is from the interaction of high-energy cosmic rays with atmospheric nitrogen and oxygen[1]. However, ^{10}Be has a short residence time in the atmosphere (less than 2 y) because it permanently binds to aerosols and reaches the Earth's surface through precipitations. In rocks, instead, ^{10}Be is primarily produced by spallation of oxygen and silicon, with production rates strongly depending on altitude and latitude.

Beryllium is a very rare element and tends not to be very mobile in the environment once it is deposited in rocks, sediments, soils or ice cores (e.g. ^{10}Be residence time in

[1]The 75% of ^{10}Be production is from neutrons; about 10% is from protons.

soils under normal conditions is 10^5 y). These two properties determine the geophysical interest for ^{10}Be. Indeed, the rarity of the stable ^{9}Be means that ^{10}Be can be detected in those natural reservoirs where other radionuclides are diluted by their stable isotope to such an extent that their measurement is impossible.

^{10}Be has a large variety of applications in Earth sciences. The measurement of ^{10}Be produced directly in rocks by cosmic rays bombardment at the Earth's surface provides information about the exposure history of the analyzed sample. In this case, it is very useful to combine measurement of other radionuclides with different half-lives (e.g. ^{14}C, ^{26}Al or ^{36}Cl) to ensure the absence of meteoric contamination [73] and to constrain erosion rates [74]. The low mobility of beryllium, once it has become attached to mineral surfaces, has led to the use of ^{10}Be to study marine sedimentation rates [75], Mn-nodules and crusts [76] and subduction pathways in arc volcanism [77]. ^{10}Be in terrestrial soils is used as a tool to to study Pleistocene surface processes or as a tracer of sediment transport [78]. ^{10}Be concentrations in polar ice have proven to provide information about the history of the cosmic ray flux in the atmosphere [79], of solar activity and of other causes of production rates variations (e.g. changes in the geomagnetic field) [80]. In addition to its terrestrial geophysical uses, ^{10}Be is also measured in extraterrestrial material, where it is produced by galactic cosmic rays (i.e. there is almost no contribution from solar cosmic rays) and represents an indicator of exposure ages [81].

The applications previously presented normally require a detection limit of the ^{10}Be/^{9}Be isotopic ratio between 10^{-15} and 10^{-11}, which can be exclusively achieved with the AMS technique.

^{10}Be measurement with conventional mass spectrometry techniques is limited mainly by the presence of three interferences: (i) 10 u mass molecules, in particular ^{9}Be^{1}H, (ii) ^{20}Ne^{2+} ions, as they have the same M/q ratio than ^{10}Be^{1+}, and (iii) the isobar ^{10}B (stable, 19.9% isotopic abundance [51]). The AMS technique is able to pass over the first two issues. The application of an adequate stripper pressure can provide indeed a complete molecular suppression, since the most of the break-up products are removed from the beam in the HE analyzer. Concerning ^{20}Ne, it cannot be extracted from the

samples because Ne, as a noble gas, has a negative electron affinity and does not form any metastable negative ions nor molecules.

Unfortunately, the isobar interference cannot be resolved by any MS system using its mass difference ΔM/M = $5.96 \cdot 10^{-5}$ relative to ^{10}Be. Besides, in AMS the process of ^{10}Be detection in a nuclear detector is complicated due to the high ^{10}B rates involved, in the range of the MHz.

^{10}Be measurements with AMS apparatuses necessarily involve sophisticated techniques that take advantage of the different stopping powers of the isobars in the matter. An overview of the currently established methods is presented in the following section, with a special focus on the developments realized at the SARA facility during the last years. The rest of the chapter is centered on the optimization of the ^{10}Be detection with different approaches, in order to find the best measurement conditions with the current SARA setup.

4.2 ^{10}B suppression methods

Several ^{10}B suppression techniques have been developed and investigated during the years within the AMS community. The feasibility and suitability of each method depends on the beam energy and the involved ^{10}Be/^{9}Be atom ratios.

Concerning the nature of the analyzed material, ^{10}Be samples can be prepared in form of fluoride compounds, where Be is analyzed as BeF^- on the LE side, or as beryllium oxide, where the BeO anion is selected.

Beryllium fluoride compounds such as BeF_2 or $BaBeF_4$ have the advantage of suppressing most of the ^{10}B in the source, since the $^{10}B^{19}F^-$ ions are metastable and dissociate on the LE side of the AMS system [82]. Residual ^{10}B coming from other 29 u mass molecules (e.g. $^{9}Be^{10}B_2^-$ or $^{10}B^{17}O^1H_2^-$) can be effectively separated from ^{10}Be in a ΔE-E$_{res}$ gas ionization chamber taking advantage of their different nuclear and electronic stopping powers [83]. The BeF_2 method provides relatively low BeF^- currents ranging from 100 to 150 nA. Other issues are given by the hygroscopic and electrostatic

nature of the material, which make complex the samples preparation and handling. The former drawbacks are overcome using $BaBeF_4$ instead, but the extracted BeF^- are still too low to assess efficient measurements [39].

The procedure to prepare BeO samples is well known and practical for routine analysis. Its issue is its toxicity, so severe protocols have to be followed for its safe manipulation in the laboratory[2]. BeO^- currents are elevate and stable compared to the ones of fluoride compounds, reaching values of few μA. The main drawback is that both BeO^- and BO^- molecules produced in the ion source are stable. The ^{10}B/^{9}Be ratio in the samples is typically of the order of 10^{-5}, therefore a ^{10}B suppression of 7-10 orders of magnitude is required to measure ^{10}Be/^{9}Be levels of $10^{-15} - 10^{-12}$. In this case, the separation cannot take place in a multi-anode detection system because the involved ^{10}B count rates of tens of MHz is high enough to saturate detector's electronics. Thus, ^{10}B count rates have to be reduced to few kHz before entering the ionization chamber, in order to achieve the desired overall suppression of 7-10 orders of magnitude. For this purpose, two approaches have been used by the AMS community: the so-called degrader and absorber techniques.

In the degrader technique, the beam passes through a thin foil placed in front of an electrostatic or magnetic deflector [84]. Since ^{10}Be and ^{10}B ions emerge from the degrader foil with different average energies, ^{10}B can be physically separated by the following filter. A suppression of 4-5 orders of magnitude is obtained and the residual ^{10}B, coming from the high energy tail of the resulting energy distribution, is separated from ^{10}Be in a ΔE-E_{res} gas ionization chamber. The disadvantages of this technique are the losses produced by the distribution of charge states, since only one of them can be selected by the subsequent cinematic filters, as well as energy and angular straggling that affect the beam after the passage through the degrader.

The second technique has been already introduced in Chapter 3 for the measurements of $^{26}Al^{2+}$ and consists in placing a passive absorber cell in front of the gas ionization

[2]To avoid the contaminant to enter the organism through the respiratory system, BeO material has to be handled in laboratory vented systems with protective masks.

chamber. Since the interfering ^{10}B has a higher differential energy loss than ^{10}Be, the passive absorber thickness (i.e. a combination of the membrane thickness and/or gas pressure in the absorber cell) can be chosen to stop ^{10}B and leave ^{10}Be to access the detector. Nowadays, this method is successfully applied at accelerator terminal voltages above 3 MV [57, 62, 63]. The problem at lower energies is that the range straggling worsens the separation between ^{10}Be and ^{10}B so that the efficiency of the technique is compromised. However, its applicability at facilities with terminal voltages below 600 kV has been recently demonstrated [37].

It is important to highlight that ^{10}Be measurements at LE-AMS facilities are possible with both the degrader and the absorber techniques exclusively with the use of silicon nitride membranes, whose homogeneity minimizes the energy and angular straggling effects on the beam compared to other materials.

^{10}Be measurements are routinely carried out at the CNA since the installation of the SARA facility in 2006. In Table 4.1, the different ^{10}B suppression techniques studied with the original setup are schematized [39]. Tests realized with fluoride compounds were not so encouraging, therefore BeO samples were analyzed with the degrader technique.

After the installation of the He-stripper and the high-resolution GIC, the question arises on which of the two techniques best suits the new setup and under which conditions. The technical upgrades are not expected to bring benefits to the fluoride compounds method, since the ionization efficiency of the source did not change and the extraction of BeF^- ions from the samples still provides low intensity currents. Therefore, the efforts have been oriented on the optimization of the ^{10}Be measurement from BeO samples.

Both the degrader and the passive absorber techniques have been widely studied with the new setup. With reference to Figure 4.1, degraders are inserted in the beam path at the waist position between the HE magnet and the ESA, whereas the passive absorber is mounted in front of the ETH GIC. Several experiments have been carried out to estimate the measurement efficiency and background, which are strictly related to the stripping process and the adopted suppression method. Since the stripping process with He gas is not well known at SARA's typical energies, a preliminar study became necessary to

Table 4.1: Recap of the ^{10}B suppression techniques tested at the SARA facility with the old setup [39]. The most suitable method resulted the BeO with a degrader foil.

	BeF_2	$BaBeF_4$	BeO
Extracted ions	BeF^-	BeF^-	BeO^-
LE current (nA)	90-150	30-50	(1-2)·10^3
^{10}B count rate (Hz) in the GIC	10^2	10^2	$10^7 - 10^8$
Normalized ^{10}B count rate (Hz/nA)	1	1	10^5
^{10}B suppression technique	GIC	GIC	Degrader + GIC
Overall efficiency (%)	45	45	5-6
Background (10^{-15})	6	Not estimated	10-40
Material properties	Electrostatic, hygroscopic	Easy to handle	Toxic

understand the effects on the stable isotope transmission as a function of the stripper thickness and terminal voltage. Then, the overall efficiency and background have been estimated and optimized depending on the suppression technique.

4.3 Samples

Severe and inevitable beam losses in the HE side of the facility occur with both the degrader and the absorber techniques. The transmission T_{HE} in the HE spectrometer has been estimated according to Formula 2.6 with standard samples produced at the Space Sciences Laboratory (SSL, University of California, Berkeley, USA) [72], whose nominal values are listed in Table 4.2. The high-level standard kindly provided by the ETH group was used for other experiments [68]. Blank material for background estimations has been prepared by precipitating a standard carrier solution (1000 mg/l Be for ICP-OES[3] produced by Merck KGaA, Darmstad, Germany) with NH_4 and calcinating in a muffle furnace at a temperature of 1000 ºC for 2 hours.

The standard and blank BeO powders have been mixed with Nb in mass proportion

[3] Acronym for Inductively Coupled Plasma Optical Emission Spectrometry.

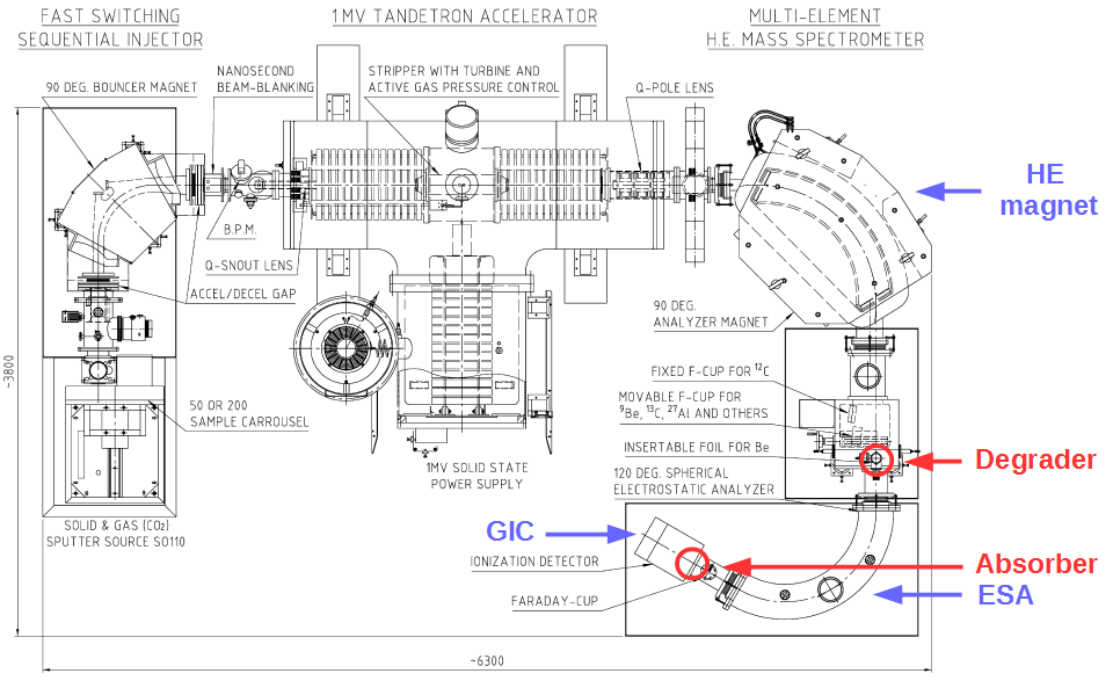

Figure 4.1: Positions of the degrader and the absorber in the SARA facility.

Table 4.2: Standard samples used during the experiments. SSL standards are normally used during routine measurements for samples normalization, having the isotopic ratio an uncertainty of $\sigma = \pm 1.1\%$ [72]. The nominal value of the ETH standard is not known with an elevate precision, but because of its high ^{10}Be content, it is more suitable for tuning or for other experiments [46].

Name	Nominal ratio (10^{-12})	Manufacturer
BeSt 2007	≈ 240	ETH
ICN 01-5-1	27.1	SSL
ICN 01-5-2	8.56	SSL
ICN 01-5-3	6.320	SSL

BeO:Nb 1:7 and pressed into appropriated Al cathodes. The so obtained BeO^- currents are of about 1-2 μA, which are higher and more stable than other metal matrixes as Ag or Cu [39].

To precisely know the ^{10}Be content in the blank used for background estimations, some of this material has been measured at the AMS facilities in Trondheim (Nasjonallaboratoriene for datering, NTNU Vitenskapsmuseet, Trondheim, Norway) and Vienna (Faculty of Physics, University of Vienna, Vienna, Austria). These AMS apparatuses have been demonstrated to be able to detect ^{10}Be/^{9}Be isotopic ratios ratios down to $3 \cdot 10^{-15}$ [85] and $5 \cdot 10^{-16}$ [57], respectively. The ^{10}Be/^{9}Be ratio of the blank used at the SARA system has been estimated in Trondheim as $(2.8 \pm 0.3) \cdot 10^{-14}$ and in Vienna as $(2.87 \pm 0.17) \cdot 10^{-14}$.

4.4 He stripping

The overall efficiency of ^{10}Be measurements is the result of two contributions: the transmission through the accelerator and through the HE spectrometer. The first one has been initially studied independently on the adopted ^{10}B suppression technique, in order to better understand the beam behaviour in the new stripper gas as a function of its thickness and the terminal voltage. The second one depends on the adopted ^{10}B suppression technique. On the other hand, the influence of the stripper on the overall efficiency and background is strictly related to the measurement technique and will be discussed in dedicated sections.

In Figure 4.2, the transmission through the accelerator is presented as a function of the He mass thickness for the 1+ and 2+ charge states at the terminal voltage V_T of 1 MV, corresponding to a stripping energy of 370 keV. The maximum transmissions are obtained for both charge states at a stripper pressure of $1 \cdot 10^{-2}$ mbar, corresponding to an areal density d_0 of 0.026 μg/cm^2. Charge state yields $\Psi_{1+} = 61\%$ and $\Psi_{2+} = 23\%$ can be extrapolated from ^{9}Be experimental data for $d > d_0$. Therefore, about 3-4% of the beam is lost in the stripper channel. Since the 3+ charge state has a transmission below

0.1% and assuming a negligible yield for the 1- at the equilibrium, a yield for the neutral state of about 27% is evinced.

Figure 4.3 shows the ^{9}Be transmission for the 1+ and 2+ charge states in the whole energy range allowed by the machine, for stripping energies between 170 keV (V_T = 450 kV) and 370 keV (V_T = 1000 kV) and for the stripper mass thickness corresponding to the maximum transmission in Figure 4.2. The lowest terminal voltage allowed by the SARA apparatus is determined by the accelerator design and by the focusing system, in particular by the lower limit of the Q-Snout lens. The transmission for the 1+ charge state increases with the energy, reaching a maximum of 58% at 1 MV. For the 2+ charge state, a decreasing behaviour is revealed until a stripping energy of 280 keV (V_T = 750 kV), where a 20% transmission is obtained, and then it starts increasing again. Therefore, in this case two maxima are present: the first one at a stripping energy of 170 keV, corresponding to a transmission of 22.5%, and another one at a stripping energy of 370 keV, where the transmission amounts to 21%.

The optimization of the stripper thickness at low energies (180 keV stripping energy, i.e. V_T = 470 kV) resulted in a maximum transmission of 24% (Figure 4.4), with a charge state yield $\Psi_{2+,470kV} = 26\%$ (5% beam losses in the stripper). If the transmission slightly increased only from 22.5 to 24% by adjusting the stripper thickness, then its optimization for all the energies is not expected to produce drastic changes in the curves in Figure 4.3.

In Figure 4.5, the measured transmissions with SARA for different stripping energies (already presented in Figure 4.3) are compared with the ones obtained with the 600 kV Tandy [37] and the 3 MV Vienna Environmental Research Accelerator (VERA). Data at VERA have been measured within a collaboration with the Isotope Research and Nuclear Physics group of the University of Vienna.

Transmissions detected with SARA for terminal voltages below 600 kV are slightly lower than the ones found at the Tandy. A possible explanation might be an ion optical effect that affects the beam at lower voltages. As it was stated before, the focusing of the beam in the middle of the stripper channel is carried out thanks to the so-called Q-Snout

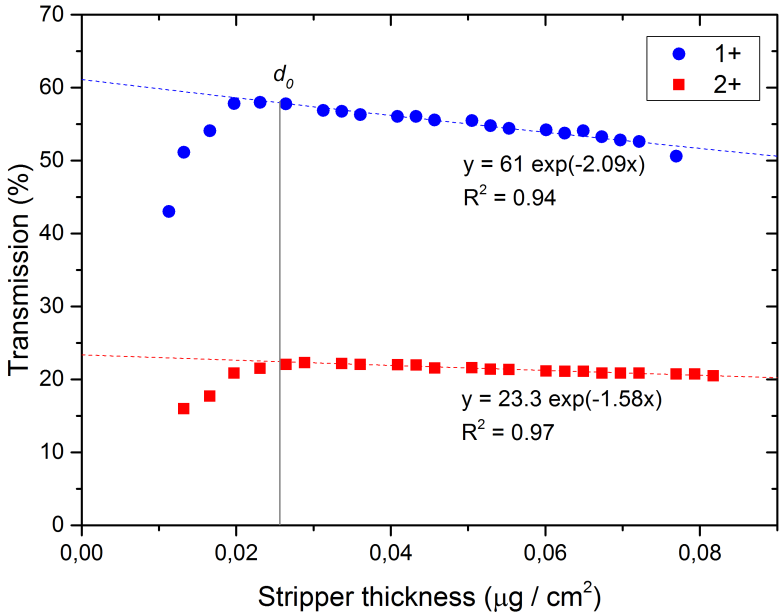

Figure 4.2: Measured ^{9}Be transmission as a function of the He stripper thickness for the 1+ and 2+ charge states at a terminal voltage of 1 MV (i.e. 370 keV stripping energy). The maximum transmissions are achieved at stripper thicknesses of about 0.026 μg/cm^2.

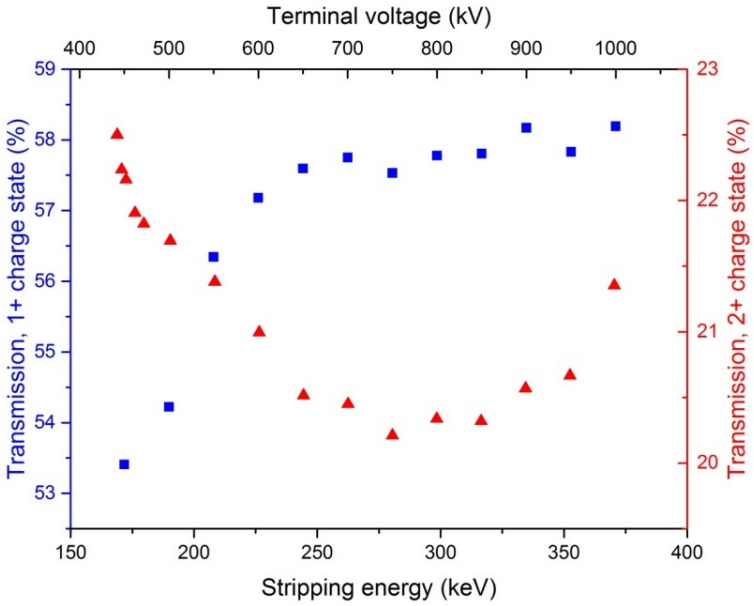

Figure 4.3: Measured ^{9}Be transmission as a function of the energy for the 1+ and the 2+ charge states for a stripper mass thickness of 0.026 μg/cm^2.

lens, by adjusting its potential with the terminal voltage according to the Formula [21]:

$$V_{Q-Snout} = 0.082 \cdot V_T - \frac{E_0}{e} \tag{4.2}$$

where E_0 is the beam energy before the accelerator. For a terminal voltage of 600 kV and an extraction energy from the ion source of 29 keV, the optimum Q-Snout potential should be 20 keV. Even if the lens voltage ranges between 0 and 60 kV, the closeness to its lower limit might deteriorate the focusing power of this optical element causing a transmission reduction through the tandem.

Data acquired at VERA show that at stripping energies of about 700 keV the 1+ and 2+ transmissions are both about 30%. Such a behaviour is expected, since the average charge state of equilibrium distribution increases with the beam energy [86].

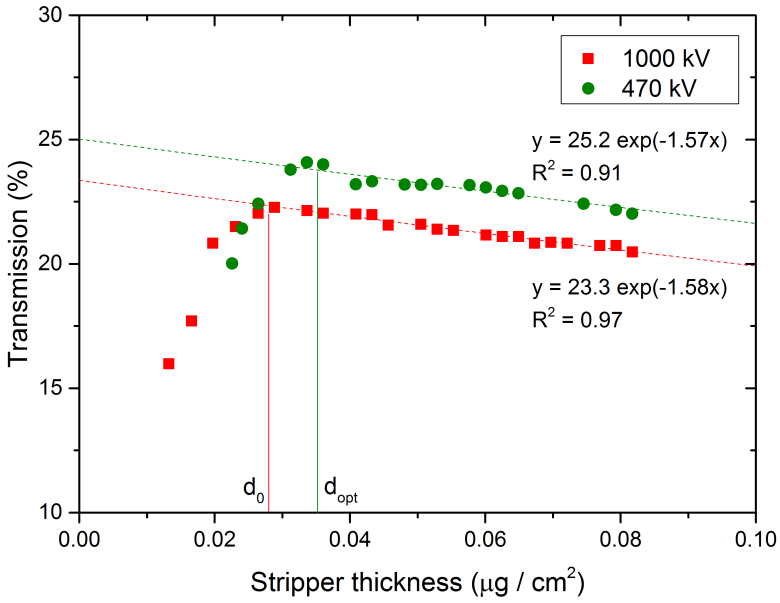

Figure 4.4: Measured ^{9}Be transmissions at the SARA system as a function of the He stripper thickness for the 2+ charge state at the terminal voltages of 470 and 1000 kV (i.e. at beam energies of 1.1 and 2.4 MeV, respectively). The optimization of the stripper thickness shows that the maximum transmission at low energies is achieved at about 0.035 μg/cm^2.

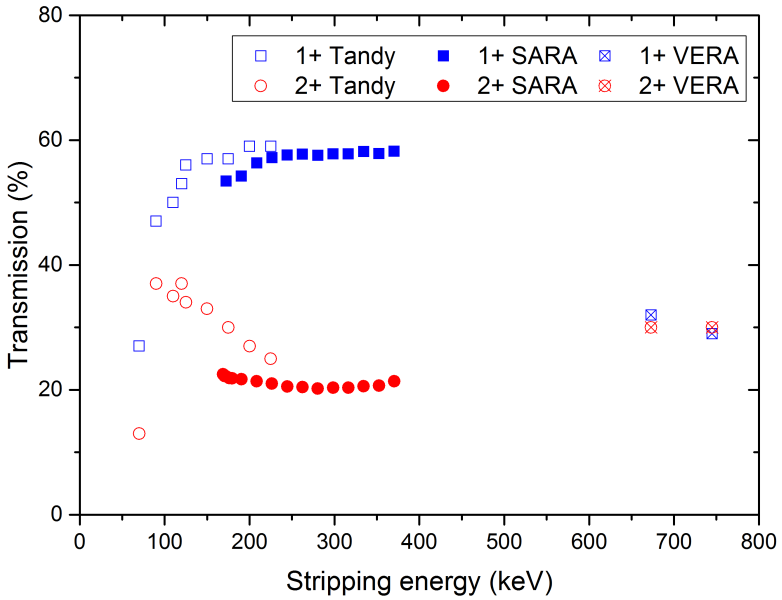

Figure 4.5: Comparison between the ^{9}Be transmissions through the accelerator acquired at the 600 kV Tandy [37], 1 MV SARA and 3 MV VERA facilities for the 1+ and 2+ charge states as a function of the stripping energy.

4.5 The degrader technique

The degrader technique was applied for the first time by Raisbeck et al. on a 2 MV AMS facility [84] and subsequently widespread to larger and smaller AMS systems. So far, it is the most common way to measure ^{10}Be with LE-AMS facilities.

SARA was designed to measure ^{10}Be using this technique [12]. Indeed, it is equipped with a dedicated holder for degrader foils placed at the beam waist position between the HE magnet and the ESA (i.e 37.5 cm distance from the ESA entrance). The energy range for ^{10}Be measurements at SARA is between 1.4 (1 MV terminal voltage, 1+ charge state after the accelerator) and 2.4 MeV (1 MV terminal voltage, 2+ charge state after the accelerator), where the main contribution to the particles stopping power S is given by the so-called Coulomb collisions with the target electrons (i.e. projectiles interact with the electrons in the target nuclei shell according to a Coulomb potential). The differential energy loss for a charged particle with kinetic energy E travelling a distance x into a

target can be described in this energy range by the Lindhard-Scharff Formula [87]:

$$S = -\frac{dE}{dx} = 8\pi r_0 \hbar \xi \frac{Z_p Z_t}{\left(Z_p^{2/3} + Z_t^{2/3}\right)^{3/2}} \quad v_p \tag{4.3}$$

where Z_p and Z_t are the projectile and target atomic numbers, respectively, v_p is the projectile's velocity, r_0 is the Bohr's radius, $\hbar$ is the reduced Planck's constant and $\xi = Z_p^{1/6}$ is an experimentally derived factor. The stopping power depends linearly on the projectile velocity and is therefore related to the energy as $S \propto \sqrt{E}$.

When the 10 u beam selected by the HE magnet passes through the degrader, ^{10}Be (Z = 4) emerges with a higher energy than ^{10}B (Z = 5) due to the Z_p dependency of the stopping power. In Figure 4.6, the mean energy loss of ^{10}Be and ^{10}B ions in silicon nitride material calculated by SRIM is plotted as a function of the energy, showing that between 1 and 2.5 MeV the isobars have a significantly different energy loss. The spatial separation Δx in mm is determined by the ESA energy resolving power:

$$\Delta x = 1300 \frac{\Delta E}{E} \tag{4.4}$$

The trajectories of ^{10}Be and ^{10}B ions after the passage through the degrader are schematized in Figure 4.7. If a 100 nm thick silicon nitride foil is used, their energy difference ΔE after the degrader is about 30-35 keV, leading to a separation Δx at the detector entrance of several millimeters as shown in Table 4.3, where ΔE and Δx are presented for two beam energies (1400 and 2400 keV). The stopping power values and the residual energies have been provided by SRIM. Since the ΔE does not present important variations between 1400 and 2400 keV, Δx decreases with the energy. A thicker degrader foil should be used to compensate this effect and to keep the desired separation between ^{10}Be and ^{10}B.

Even if the presence of the degrader foil leads to a ^{10}B suppression of 4-5 orders of magnitudes before the detector, part of the high-energy ^{10}B tail still enters the chamber. However, a count rate of few kHz is recorded for degrader foils of 100-150 nm thickness and can be handled by the GIC. ^{10}Be can be discriminated by taking advantage of the anode split in two sections, so that both ΔE and E_{res} signals are measured.

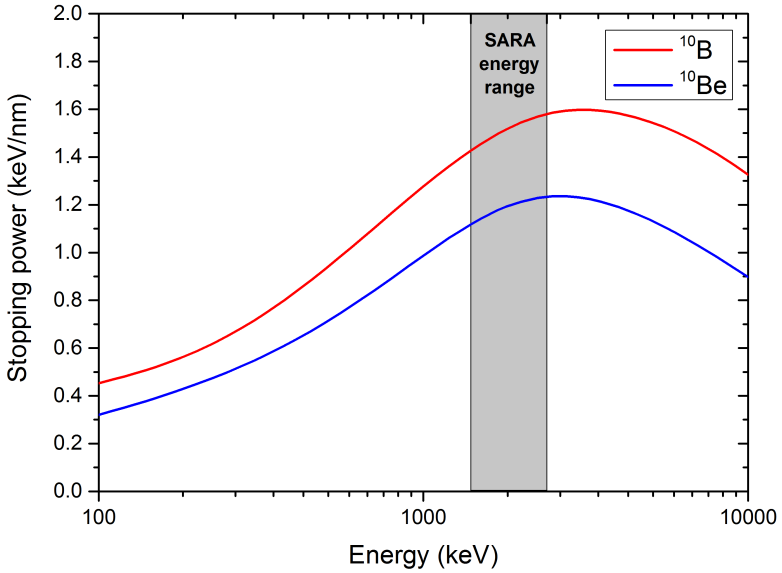

Figure 4.6: Electronic stopping power of ^{10}Be and ^{10}B ions in silicon nitride as a function of the energy according to the SRIM tool. ^{10}Be energy range at the SARA facility is highlighted in grey.

Table 4.3: Main parameters influencing the beam behaviour through a 100 nm degrader foil. ^{10}Be and ^{10}B ions emerge with an energy difference ΔE and arrive to the ESA image point with a spatial separation Δx.

Energy (keV)	-dE/dx (keV/nm)		Residual energy (keV)		ΔE (keV)	Δx (mm)
	^{10}Be	^{10}B	^{10}Be	^{10}B		
1400	1.118	1.427	1288	1257	31	31
2400	1.236	1.586	2276	2241	35	20

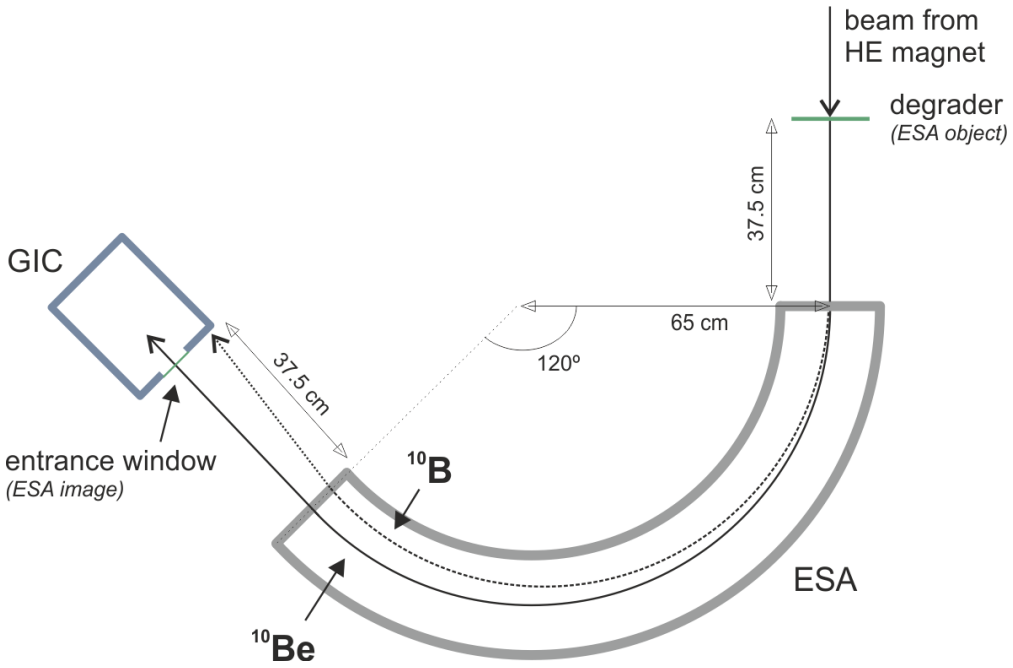

Figure 4.7: Schematic representation of ^{10}Be and ^{10}B trajectories in the ESA deflector after the passage through a degrader foil.

At 1 MV terminal voltage, ^{10}Be ions in the 1+ charge state reach the degrader with a 1400 keV energy. According to SRIM, for a silicon nitride foil thickness of 100 nm, the residual energy, i.e. the ^{10}Be average energy after passing through the membrane, is about 1290 keV (Table 4.3). In Figure 4.8, SRIM simulations of the energy loss of 1290 keV ^{10}Be and ^{10}B ions in 15 mbar isobutane gas are plotted against the penetration depth in the ETH GIC equipped with a 50 nm thickness silicon nitride window. Having a higher atomic number, ^{10}B produces more charge for ionization than ^{10}Be before the crossing point of both curves; after the crossing point, the situation is reversed. If the detector pressure is selected so that the intersection point is exactly between the two sections, the best possible isobar separation is achieved since the pulse height difference for isobars in the respective sections becomes maximum. In Table 4.4, the average energy deposited in the different GIC components by ^{10}Be and ^{10}B according to SRIM calculations is summarized, assuming the ions carry a 1290 keV energy after the degrader and the GIC is filled with 15 mbar isobutane.

Figure 4.9 shows an example of ^{10}Be spectrum acquired with the upgraded SARA setup, where signals from the E_{res} section are plotted against the ones from the ΔE anode. The lines corresponding to the same total energy have a -45º slope, therefore, points lying on the same line correspond to projectiles which release the same energy in the chamber. ^{10}Be and ^{10}B peaks appear in the spectrum with an ellipsoidal shape because of the energy straggling in the entrance window and in the gas detector. The ^{10}B low-energy tail is due by ^{10}B ions that undergo scattering processes at the ESA electrodes. Even if the isobars reach the GIC with the same energy, their peaks are not lying on the same total energy line for two reasons: (i) the energy loss in the detector window is not the same and (ii) the gas ionization yield depends on the projectiles species. Indicating with $\delta_{\Delta E}$ and $\delta_{E_{res}}$ the energy loss difference between the isobars in the first and the second anode respectively, the separation in the spectrum between the two isobars can be expressed as:

$$\delta_{E_{tot}} = \sqrt{\delta^2_{\Delta E} + \delta^2_{E_{res}}} \tag{4.5}$$

and represents the distance between the projections of the centroids of the ^{10}Be and ^{10}B

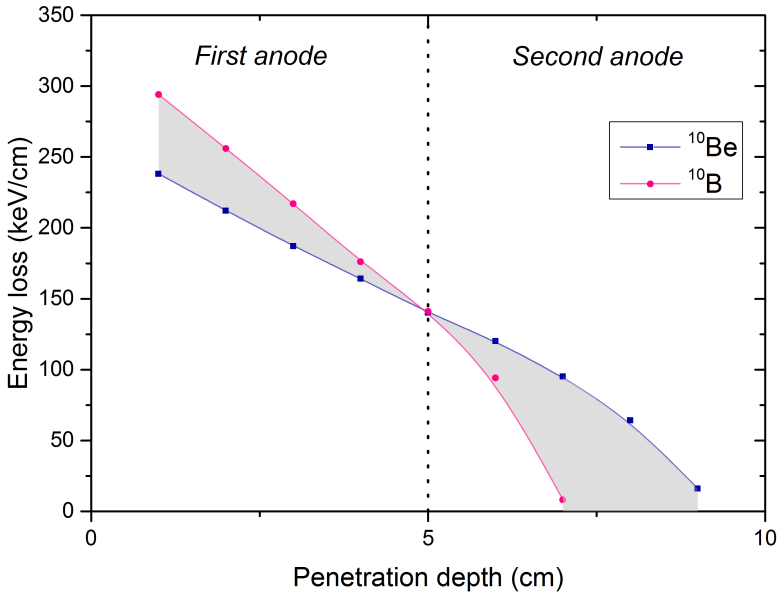

Figure 4.8: SRIM simulations of ^{10}Be and ^{10}B differential energy loss as a function of the penetration depth in the detector, assuming an energy of 1400 keV after the accelerator and a degrader of 100 nm thickness. The GIC is supposed to be equipped with a 50 nm thick silicon nitride window and filled with 15 mbar isobutane pressure. In this configuration, ^{10}Be ions emerge the degrader with about 1290 keV energy and enter the gas chamber with an average residual energy of 1240 keV. A fraction of the ^{10}B ions also emerge the degrader with 1290 keV energy and reaches the detector. After passing through the window, it enters the chamber with about 1220 keV energy.

Table 4.4: SRIM calculations of the deposited energy of 1290 keV ^{10}Be and ^{10}B in the different GIC components, assuming a 50 nm thickness entrance window and 15 mbar gas pressure.

Projectil	Energy loss (keV)		
	GIC window	ΔE section	E_{res} section
^{10}Be	52	941	295
^{10}B	67	1084	112
^{10}Be - ^{10}B	-15	-143	183

peaks to the same total energy axis.

The main disadvantage of the degrader technique is represented by significant beam losses in the HE spectrometer which considerably reduce the measurement efficiency. The degrader acts as a a second stripper, producing a distribution of charge states in the emerging ions (post-stripping). As the ESA is an E/q filter, part of the beam is lost because of the selection of just one charge state amongst the ones available after the membrane (mainly 2+ and 3+ at beam energies between 1 and 2.4 MeV). In the following, the selection of the charge state q after the accelerator (by the HE magnet) and q' after the degrader (by the ESA) will be indicated as the qq' configuration. Further losses are due to the energy and angular stragglings that increase the beam size after the degrader and cause part of the ions not to fulfill the ESA or the detector window acceptance.

Figure 4.10 shows ^{10}Be spectra acquired in the 2+2+ configuration at 1 MV terminal voltage (i.e. 2.4 MeV beam energy) for a standard and a blank sample with the upgraded SARA setup and a 100 nm degrader. ^{10}Be and ^{10}B peaks are easily identifiable with a very good and distinct separation.

4.5.1 Transmission through the high-energy spectrometer

As it was already stated in the previous section, the main disadvantage of the degrader technique lies in notable beam losses in the HE spectrometer.

First of all, ^{10}Be ions leave the degrader foil in a distribution of charge states, whose population yields depend on the beam energy. The ESA selects only one of the charge states resulting from such a post-stripping process, with consequent efficiency reduction.

Furthermore, the passage through the foil introduces in the emerging ions energy and angular stragglings, for which the beam shape is deformed during the passage through the ESA. To visually represent the effects of energy and angular dispersions, the beam behaviour from the degrader to the detector in the horizontal plan has been simulated with the GICOSY program [88], which provides accurate descriptions of ion optical systems using the transfer matrices associated to the optical elements. The different beam loss contributions have been simulated individually and in combination for a 1400 keV

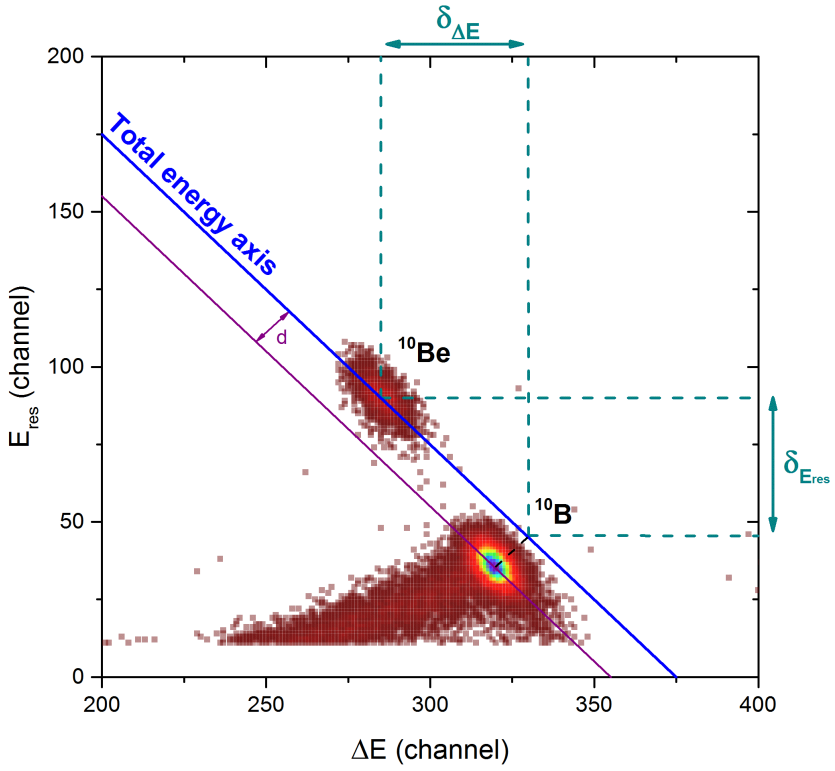

Figure 4.9: Example of a ^{10}Be 2D spectrum acquired at the upgraded SARA facility. The total energy lines passing through the ^{10}Be and ^{10}B peaks centroids are represented.

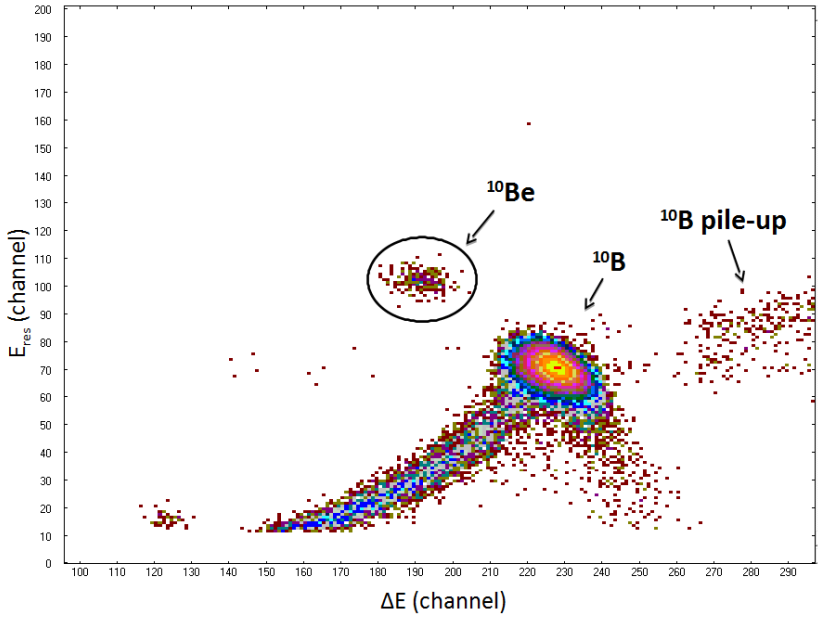

(a) Spectrum of the ICN-5-1 standard measured for 15 min to identify the ^{10}Be gate.

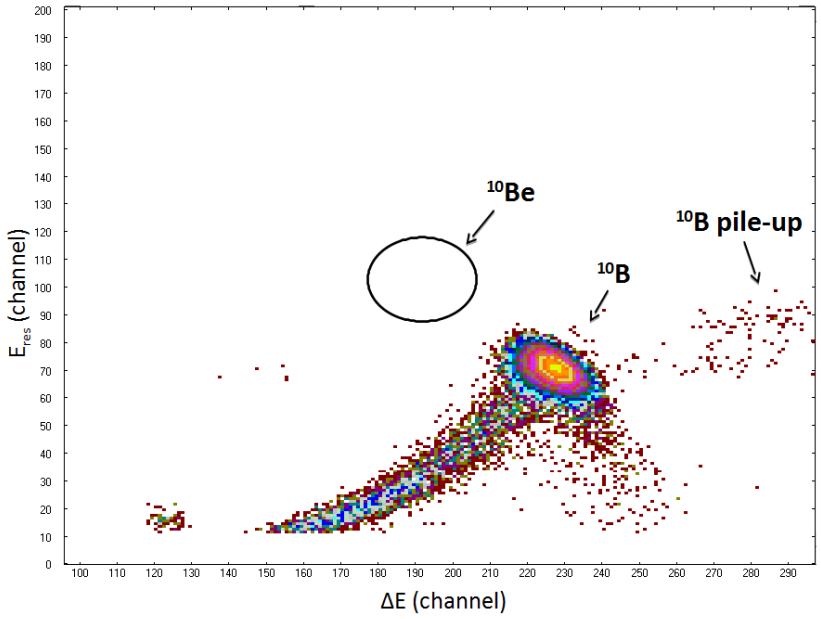

(b) Spectrum of a blank sample after 1 hour of measurements. No counts have been recorded.

Figure 4.10: Acquired ΔE-E$_{res}$ spectra with the He stripper and the ETH GIC during a 2.4 MeV ^{10}Be measurement (i.e. in the 2+2+ configuration). A 100 nm silicon nitride foil was used as a degrader.

beam (Figure 4.11).

In Figure 4.11a, just the effect of the energy straggling is considered: the beam starts broadening after entering the ESA until reaching the detector, where part of the ions is lost because of the acceptance of the GIC entrance window. The angular straggling effect is instead represented in Figure 4.11b: the beam increases its size after the degrader until the middle of the ESA and then reduces it, being minimum at the GIC entrance which is the ESA image. In this case, the beam losses are determined by the angular acceptance of the ESA, i.e. by the gap between the electrodes plates. The combination of the energy and angular stragglings is finally illustrated in Figure 4.11c.

In conclusion, the total ^{10}Be loss λ_{tot} due to the degrader foil can be explained in terms of the losses due to post-stripping λ_y, energy straggling λ_e and angular straggling λ_a according to the Formula:

$$\lambda_{tot} = \lambda_y \cdot \lambda_e \cdot \lambda_a \tag{4.6}$$

These three effects are independent on the charge state selected at the exit of the accelerator but are strongly related with the beam energy. However, two energy values are of special interest within this work: 1400 and 2400 keV. The first item correspond to the energy of the ions emerging the accelerator at 1 MV terminal voltage in the 1+ charge state; as demonstrated in Figure 4.2, the maximum transmission of about 60% through the He stripper is measured in these conditions. The second item represents the energy of the ions in the 2+ charge state at 1 MV terminal voltage. Even if the transmission through the accelerator is lower than the 1+ (about 25%), the higher energy results in reduced losses through the HE spectrometer.

A quantitative analysis of the different processes causing beam losses is presented in the following sections, where experimental data are given and supported by simulations with a deeper focus on the 1400 and 2400 keV beam energies.

Charge states distribution

In order to get an estimate on the relative charge state yields (i.e. the percentage of ions that leave the degrader in a certain charge state) after passing the degrader, the ^{10}Be

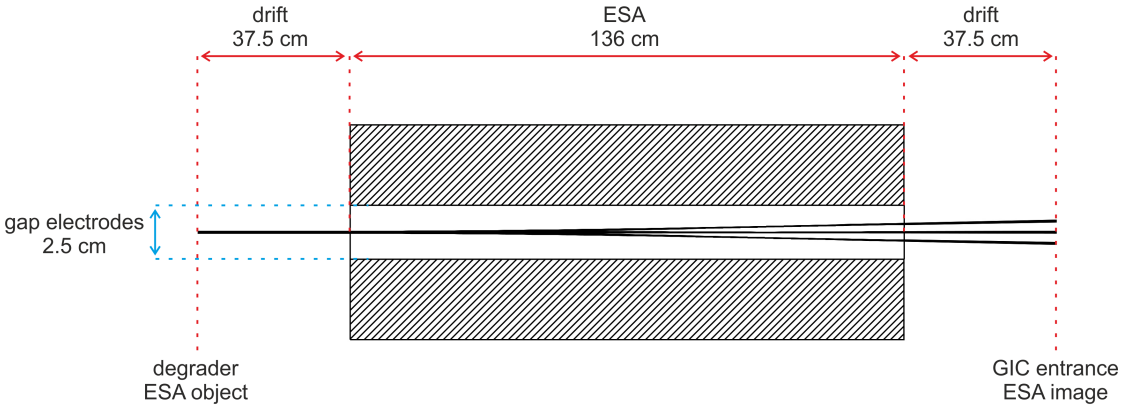

(a) Energy straggling.

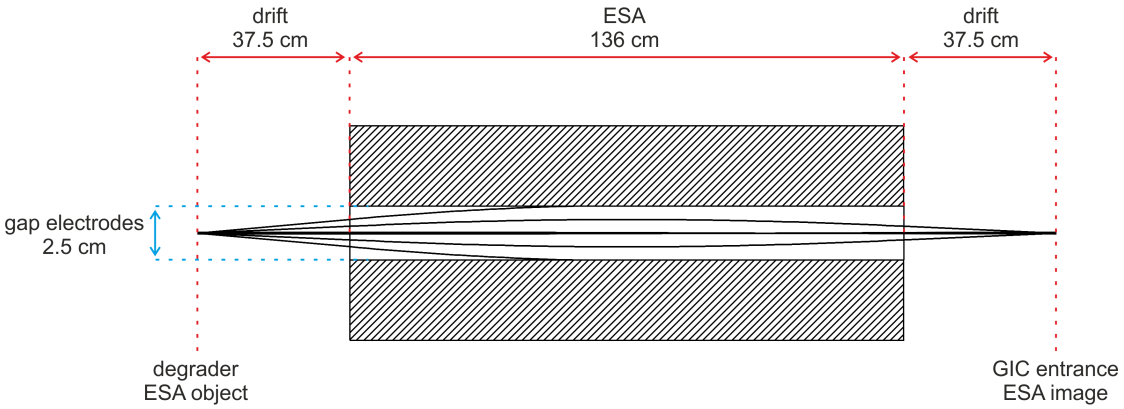

(b) Angular straggling.

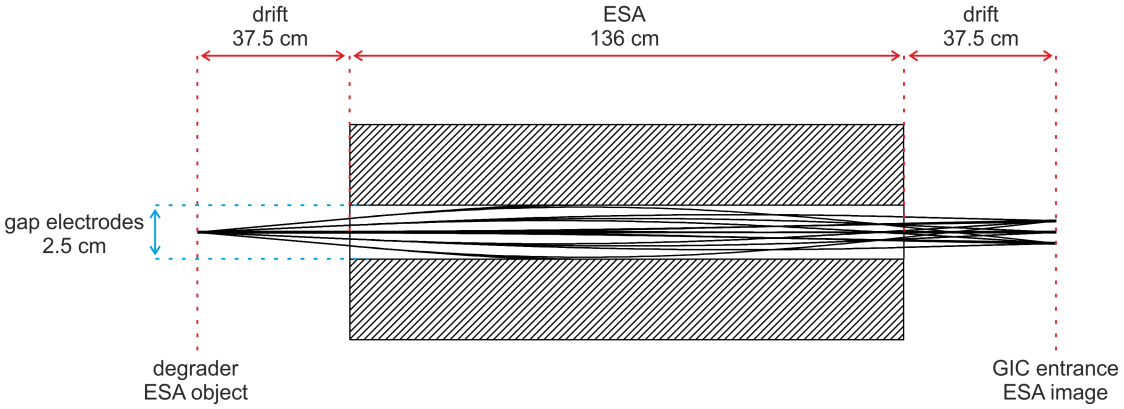

(c) Combined energy and angular straggling.

Figure 4.11: GICOSY simulations visually representing the effect of the energy and angular stragglings on a 1400 keV ^{10}Be beam passing through a 100 nm silicon nitride degrader. Ions' trajectories in the horizontal plan from the degrader to the detector are illustrated for three different initial energies ($\Delta E/E = 0, \pm 0.4\%$) and five angles ($\alpha = 0, \pm 8.5, \pm 17$ mrad).

transmissions for the different charge states from a 150 nm silicon nitride membrane to the detector is illustrated in Figure 4.12 for beam energies between 1100 and 2400 keV. These value have been obtained by comparing the measured ^{10}Be/^{9}Be isotopic ratio of a standard sample with its nominal one, according to Formula 2.5.

The 2+ and 3+ transmissions increase with the beam energy, reaching maximum values of 18% and 12% at 2.4 MeV, respectively. The 1+ charge state could be investigated just at low energies because of the limitations imposed by the electrostatic analyzer.

Based on the experimental transmission data, yields have been roughly estimated for a given beam energy assuming that every charge state is affected by the same losses and that the neutral and 4+ charge states are not significantly populated. Calculated yields are given in Table 4.5 for 1400 and 2400 keV beam energies.

Energy straggling

The energy straggling caused by the silicon nitride foil results in a broadening of the beam size in the horizontal plan up to several mm at the ESA image position according to the Formula 4.4 (Figure 4.11a), so that part of the ions is lost because of the acceptance ϵ imposed by the detector window. If the membrane has a side l = 5 mm, ϵ can be calculated from the Formula 4.4 as:

$$\epsilon = \left(\frac{\Delta E}{E}\right)_{accepted} = \frac{l}{1300[mm]} = \pm 0.2\% \tag{4.7}$$

The ESA scans given in Figure 4.14 show the ^{10}Be ions energy dispersion at the energies of 1400 and 2400 keV after the accelerator with a 100 nm degrader foil. The acceptances of the GIC window are indicated, showing the relevance of the losses taking place in both cases.

The energy straggling ΔE, i.e. the sigma of the energy distribution, has been estimated between 1 and 2.5 MeV according to Sun's semi-empirical Formula 2.15. Based on the experience of the ETH group, the real foil thickness has been considered a 10% thinner than the nominal value [46]. The relative energy straggling ΔE/E decreases with the beam energy and increases with the degrader thickness, as it is represented in Figure

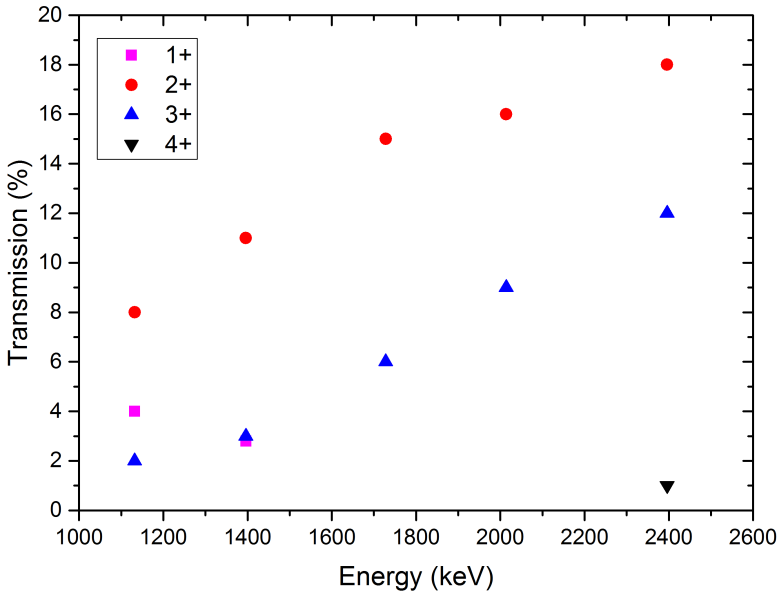

Figure 4.12: Transmission through a 150 nm degrader as a function of the energy for the 1+, 2+ and 3+ charge states.

Table 4.5: Calculated charge states yields in the post-stripping process for two different beam energies.

Energy (keV)	Charge state	Measured transmission (%)	Estimated yield (%)
1400	1+	3	18
	2+	10	65
	3+	3	18
2400	1+	$< 1^*$	2
	2+	18	57
	3+	12	38
	4+	1	3

* Extrapolated from the plot in Figure 4.12.

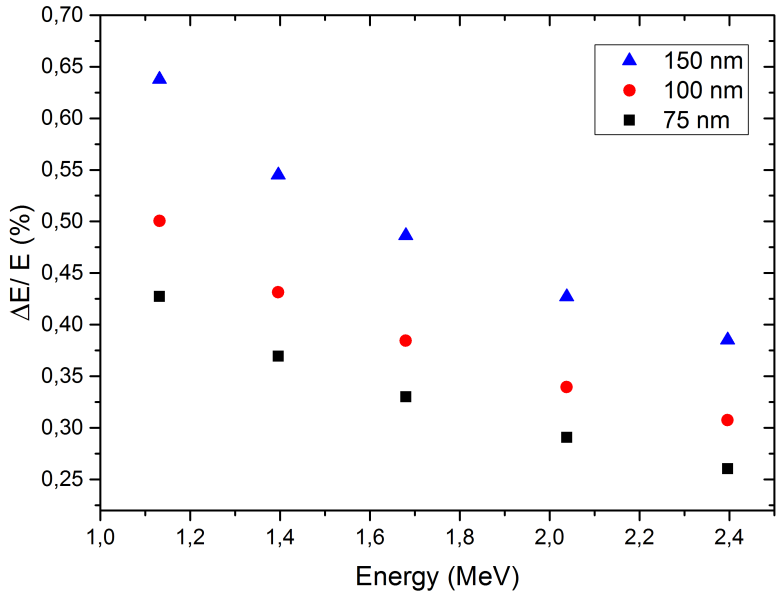

Figure 4.13: Energy straggling according to the Sun's formula.

4.13, where E is the residual energy after the degrader according to SRIM. Assuming that the beam energy distribution is described as a normal distribution with the mean value $\overline{E}$ and standard deviation ΔE provided by the Sun's formula, the transmission through the detector window is the probability for the ions to have an energy between $\overline{E} - \epsilon$ and $\overline{E} + \epsilon$ and is therefore provided by the standard normal table.

The beam widths and estimated transmission for 1400 and 2400 keV beam energies and different degrader thicknesses are given in Table 4.6.

Angular straggling

The angular straggling has the effect of broadening the beam size while passing through the ESA, as shown in Figure 4.11b. The angular acceptance of the rare isotope beam line from the degrader to the detector is limited by the gap between the ESA electrodes (i.e. 2.5 cm) and amounts to 15 mrad. Figure 4.15 shows that the angular straggling calculated with SRIM decreases with the ions' energy and increases with the degrader thickness.

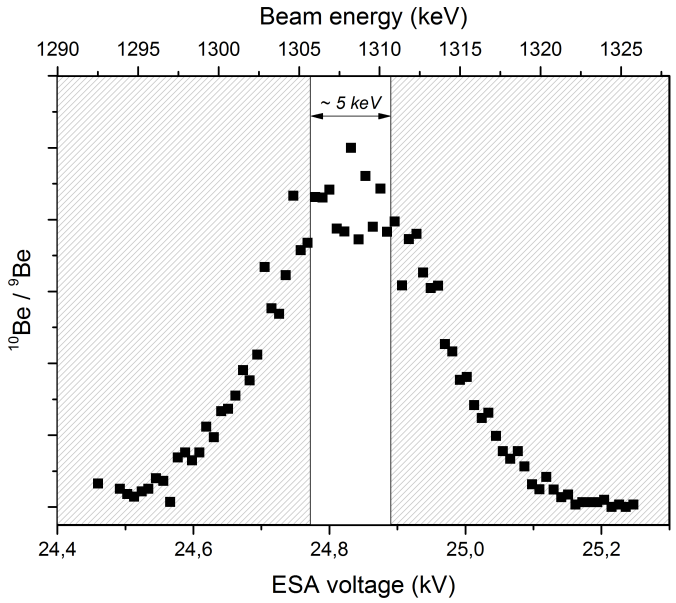

(a) 1+2+ configuration (1400 keV).

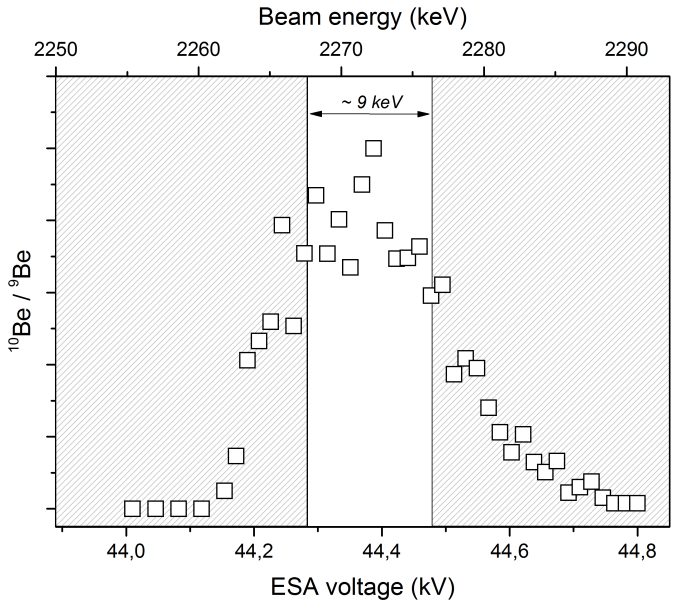

(b) 2+2+ configuration (2400 keV).

Figure 4.14: ESA scan of the 1+2+ and 2+2+ configurations at 1 MV terminal voltage and with a 100 nm degrader foil. The energy acceptance of the detector window is indicated in both cases.

Table 4.6: Calculated energy straggling after degrader foils and consequent beam spatial broadening at the ESA image position for different energies and membrane thicknesses. Estimated transmissions through the GIC entrance window are reported.

Energy (keV)	Degrader thickness (nm)	Energy straggling (%)	Beam width (mm)	Estimated transmission (%)
1400	75	0.3	9	42
	100	0.4	11	36
	150	0.5	13	30
2400	75	0.2	7	54
	100	0.3	8	49
	150	0.3	9	41

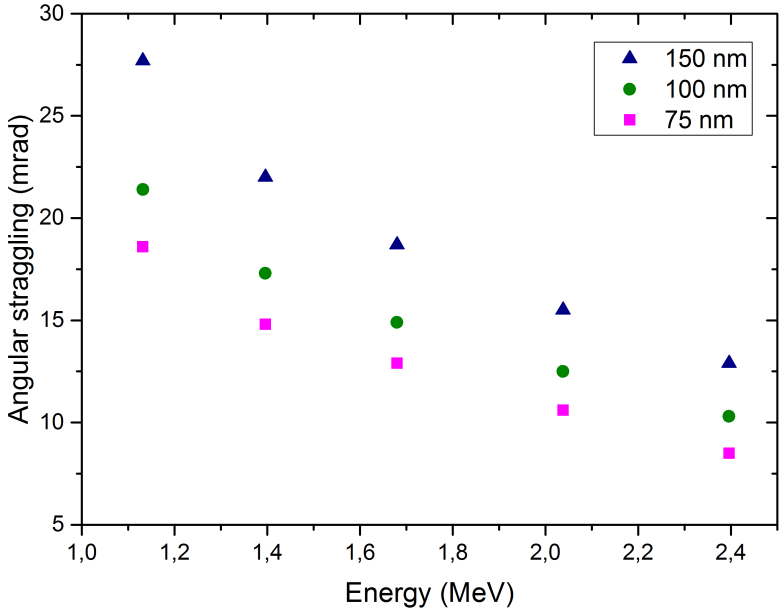

Figure 4.15: Angular straggling according to SRIM simulations.

The transmission through the ESA can be estimated with a procedure analogue to the one previously described for the energy straggling, assuming that the beam angular distribution has a mean value $\alpha = 0$ mrad and a standard deviation $\Delta\alpha$ provided by SRIM[4]. Calculated transmissions of 1400 and 2400 keV ions for different degrader thicknesses are given in Table 4.7.

Comparison between estimated and measured transmissions

Based on the estimated charge states yields in Table 4.5 and on the beam losses due to energy and angular stragglings given in Tables 4.6 and 4.7, a rough estimation of the beam transmission through the HE spectrometer is possible. In Table 4.8, calculated transmissions are reported for beam energies of 1400 and 2400 keV and a 150 nm silicon nitride degrader. These values result in a very good agreement with the experimental data.

As suggested from Figures 4.13 and 4.15, both energy and angular stragglings increase with the degrader thickness. Therefore the use of thin membranes might seem preferable. However, the agreement between the experimental and estimated transmissions is good for thick foils, but tends to deteriorate at reduced silicon nitride thicknesses, as it is shown in Figure 4.16.

The discrepancy found with the thinnest foil could be caused by a difference between the nominal thickness and the real one. However, the measured transmissions for a 75 nm foil would suggest a thickness of about 100 nm, i.e. about 30% thicker than the nominal. Such a high discrepancy is rather improbable, since the silicon nitride foils are provided by Silson with an uncertainty on the thickness of about $\pm 10\%$.

A more likely explanation could be the efficiency reduction of the detecting system because of the higher ^{10}B count rate, since the thinner is the foil the smaller is the energy difference between ^{10}Be and ^{10}B. In the 2+2+ configuration, the total count rate in the

[4]SRIM considers a point-like input beam and therefore provides just approximate estimations of the transmission through the ESA, since the ions arrive to the degrader (i.e. at the HE magnet image position) with a spatial dispersion of ± 1 mm [21].

Table 4.7: Angular straggling after degrader foils for different energies and membrane thicknesses according to SRIM simulations. Estimated transmissions through the ESA are reported.

Energy (keV)	Degrader thickness (nm)	Angular straggling (mrad)	Estimated transmission (%)
1400	75	14	72
	100	17	62
	150	23	50
2400	75	9	90
	100	10	86
	150	13	76

Table 4.8: Comparison between the estimated and measured transmissions of 1400 and 2400 keV ^{10}Be ions passing through a 150 nm degrader membrane.

Energy (keV)	Energy str. losses (%)	Angular str. losses (%)	Charge state	Estimated yield (%)	Estimated transmission (%)	Measured transmission (%)
1400	70	50	1+	18	3	3
			2+	65	10	10
			3+	18	3	3
2400	59	24	1+	2	0.7	$<$ 1*
			2+	57	18	18
			3+	38	12	12
			4+	3	1	1

detector is above 10 kHz for 75 or 100 nm degraders, whereas it is few hundreds of Hz when a 150 nm foil is used. Since the ^{10}B content in "real samples" is normally higher than in the standard and blank materials, the use of thick degraders is recommended to avoid that the elevate ^{10}B count rate increases the ADC dead time with the consequent detection efficiency reduction.

Overall efficiency

The overall efficiency of the measurements depends both on the transmission through the accelerator and the HE spectrometer after the beam emerges the degrader foil.

The overall efficiencies for the different charge states configurations and beam energies have been finally calculated with Formula 2.8 and summarized in Table 4.9, where the 1+2+ and 2+2+ are clearly the most interesting ones for their high efficiency. Indeed, even if the 2+ transmission through the accelerator (22%) is almost three times lower than the 1+ (58%), the 2+ beam losses produced by the passage through the degrader are considerably lower. This is a consequence of the higher energy of the 2+ charge state (2.4 MeV, instead of the 1+ 1.4 MeV), that results in reduced beam losses on the HE side due to the lower energy and angular straggling introduced in the degrader.

4.5.2 Background

The measurement optimization does not involve exclusively the maximization of the overall efficiency, but also the minimization of the ^{10}Be/^{9}Be background ratios. A detailed investigation of the potential background causes has been therefore carried out and is presented in the following sections.

In addition to the efficiency values, in Table 4.9 the backgrounds are reported, which have been evaluated by measuring blank samples and correcting the acquired values by the nominal ratio of a standard sample. Corrected ratios of a few 10^{-14} are obtained, which reflect the isotopic ratios of the blank samples adopted for the experiments. This means that to better test the sensitivity of the SARA facility, another material with less

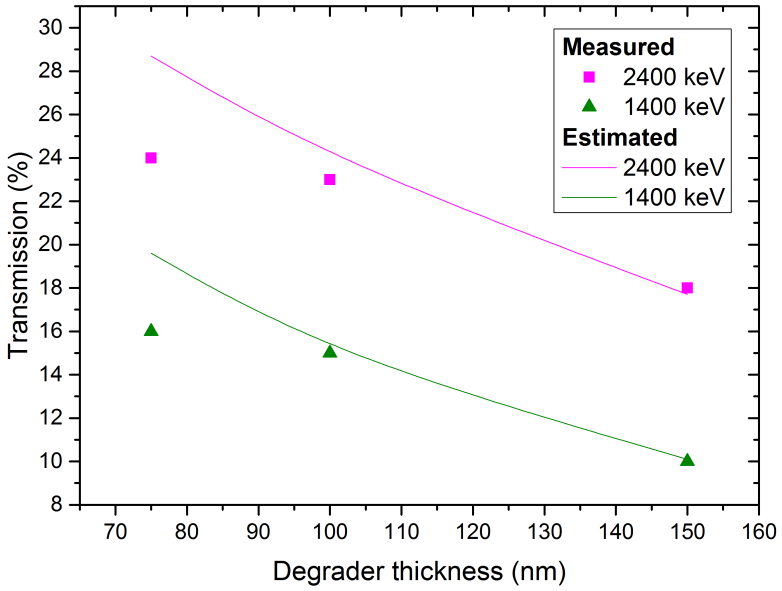

Figure 4.16: Transmission of ^{10}Be ions in the 1+2+ and 2+2+ configurations (1400 and 2400 keV beam energies, respectively). Estimated values for the 75 nm membrane are higher than the experimental ones, whereas the agreement is better in the case of the thicker foils.

Table 4.9: Overall efficiency and background for different charge states configurations and beam energies. The He stripper thickness has been set to 0.026 μg/cm^2 (corresponding to the highest transmission through the accelerator) and a 100 nm silicon nitride has been used as a degrader.

Energy (keV)	Charge states configuration	Transm. accelerator (%)	Transm. HE side (%)	Overall efficiency (%)	Background* (10^{-14})
1400	1+1+	58	4	2	6
1400	1+2+	58	10	6	4
2400	2+2+	21	23	5	2
1100	2+2+	24	8	2	6

* Background levels are measured with an error $\sigma = 20\%$.

or nominally no ^{10}Be content should be used.

The background levels presented in Table 4.9 have been obtained with an appropriate closure of the HE slits along the beam path, in order to keep the background low without affecting relevantly the beam transport to the detector. However, to study the different effects responsible for ^{10}Be background, all the experiments described in the following sections have been done with the slits completely open.

Memory-effect in the ion source

The memory-effect in the ion source has been identified by measuring a blank sample after running a standard for few hours. A decrease in the number of background events is recorded with time, proving that ^{10}Be events are coming from the contamination produced by the previous standard material. However, further studies and experiments are still necessary to quantitatively define the memory effect contribution on background estimations and measurements.

Isobar suppression

Since part of ^{10}B suppression takes place in the GIC, ^{10}Be and ^{10}B have to be clearly separated in the 2D spectrum. Even if the separation between ^{10}Be and ^{10}B is better at higher energy, the peaks are well distinguishable also at 1400 keV (Figure 4.17).

Molecular background

If the stripper thickness is not set for a full molecular dissociation, 10 u molecules like ^{9}Be^{1}H survive the stripping process and enter the HE spectrometer. One advantage of the degrader technique is that the post-stripping ensures full molecular suppression. As it will be demonstrated in Section 4.6.3, molecules are not dissociated at the stripper thickness corresponding to the highest transmission (0.03 μg/cm^2) and are present at levels of $10^{-9} - 10^{-8}$. This intense background is not found with the degrader technique, indicating that ^{9}BeH molecules break into the foil and the products are effectively removed by the

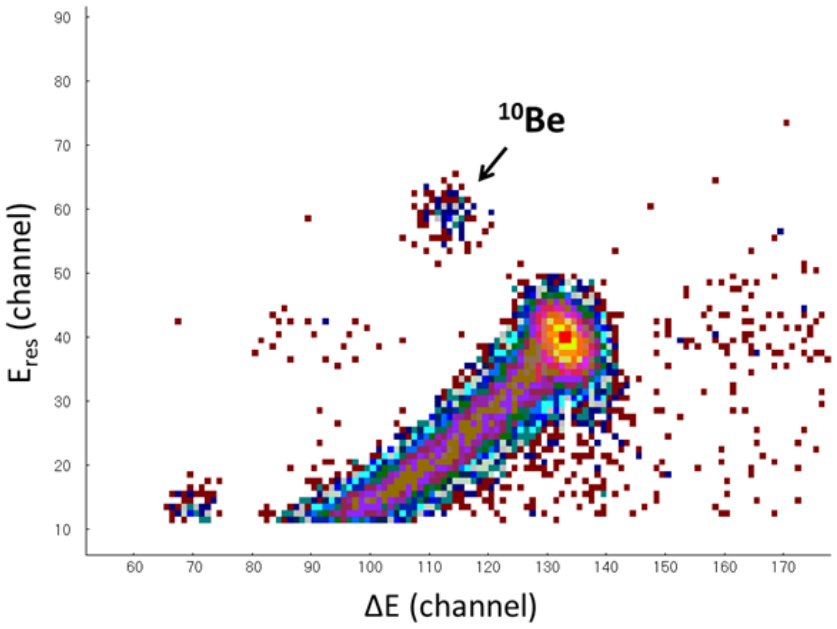

(a) 1+2+ configuration (1400 keV).

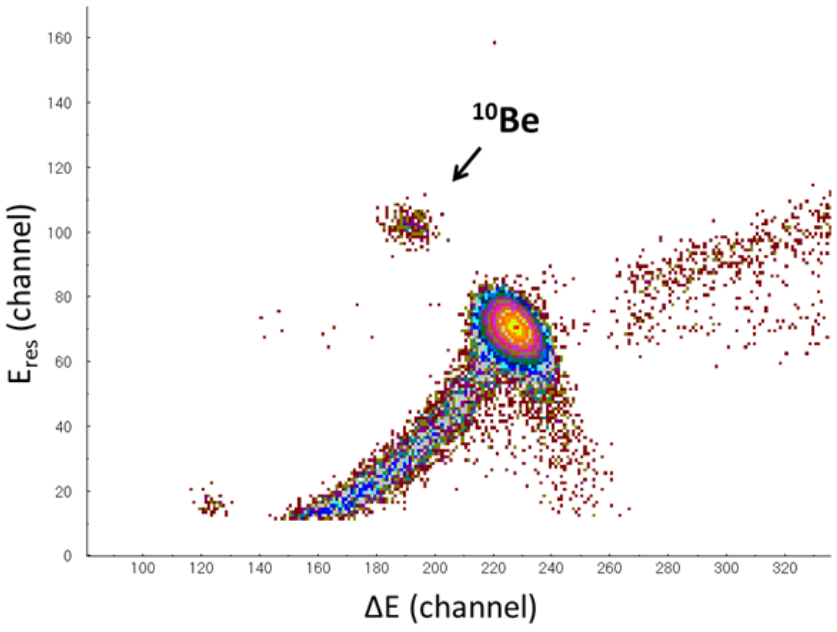

(b) 2+2+ configuration (2400 keV).

Figure 4.17: ^{10}Be spectra of a standard sample.

ESA.

Scattered ^{9}Be

Molecules as $^{9}Be^{16}O^{1}H$ and $^{9}Be^{17}O$ with mass of 26 amu are extracted from the BeO samples and driven by the LE magnet to the accelerator with $^{10}Be^{16}O$. Following the stripping process, a fraction of ^{9}Be acquires a higher charge state than ^{10}Be, enabling an additional energy gain in the high energy tube. By collisions with residual gas from the stripper along the HE tube, those ^{9}Be ions catch an electron and outgo the accelerator with the same momentum and charge state as ^{10}Be. Hence, simulating ^{10}Be magnetic rigidity, ^{9}Be ions are selected by the HE magnet and reach the degrader where, because of their stronger stopping power and the energy straggling effect, are shifted towards the ^{10}Be energy window.

Several experimental evidences confirm the occurrence of these scattering processes and their role in the background estimations. The scattering processes in the HE tube are related to the presence of residual gas from the stripper, which increases with the gas pressure. Therefore, a dependency of the background on the He stripper thickness is expected. Blank samples measured at different stripper pressures in the 1+2+ configuration at 1 MV terminal voltage reveal that at the stripper thickness corresponding to the maximum transmission (0.03 μg/cm^2), the background is $4{\cdot}10^{-14}$, whereas at a value three times higher (0.09 μg/cm^2) it increases to $1{\cdot}10^{-13}$.

As demonstrated in Figure 4.18, the stripper thickness does not affect with the same importance the background in the 2+2+ configuration, due to the lower probability of producing $^{9}Be^{3+}$ compared to $^{9}Be^{2+}$ in the accelerator tubes. Additionally, dispersive processes in the stripper and the degrader are reduced as a consequence of the higher beam energy of the 2+2+ configuration (2400 keV, despite 1400 keV in the 1+2+ configuration).

Spectra of a blank sample recorded for 15 minutes at the stripping thickness of 0.09 μg/cm^2 is shown in Figure 4.19, where the scattered ^{9}Be peak is clearly visible and partially overlaps the ^{10}Be gate.

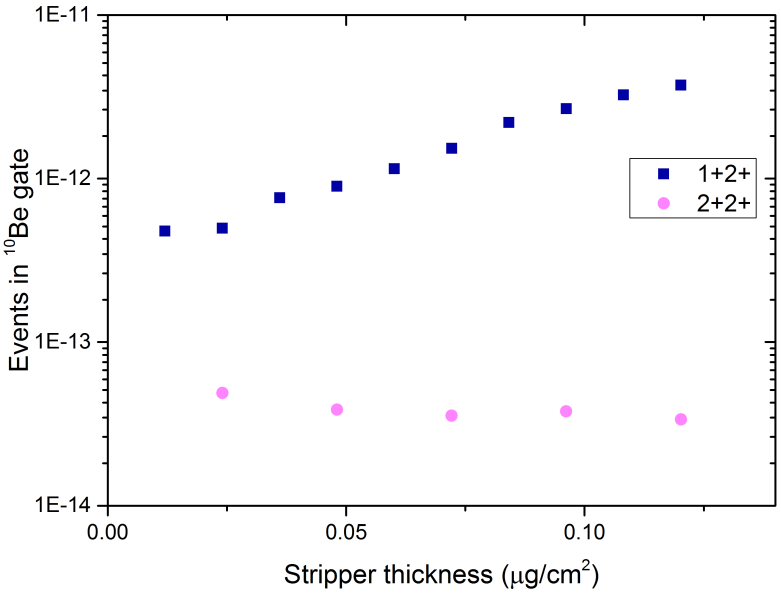

Figure 4.18: Measured ^{10}Be background as a function of the He stripper thickness in the 1+2+ and 2+2+ configurations at 1 MV terminal voltage, corresponding to beam energies of 1400 and 2400 keV respectively. The measurement time for each point is 15 minutes.

4.6 The passive absorber technique

The passive absorber technique has been already introduced in Chapter 3 for ^{26}Al measurements in the 2+ charge state and consists in installing an absorber material in front of the rare isotope detector. The principle of operation of this technique is based on the ranges difference in the absorber of projectiles with the same initial energy but different atomic number. The 10 u beam originating from the stripping process in the accelerator travels through the HE spectrometer directly to the detector, so that ^{10}Be and ^{10}B reach the absorber with the same energy. The ion with the higher nuclear charge (^{10}B) experiences a stronger deceleration than the one with a smaller atomic number (^{10}Be), which is therefore stopped at a shorter distance. The absorber thickness can thus be set to fully stop the interference and allow exclusively ^{10}Be to enter the detector.

The passive absorber technique is an affirmed and efficient method to measure ^{10}Be at facilities working with terminal voltages of 3 MV and above [64, 65, 66, 67, 89];

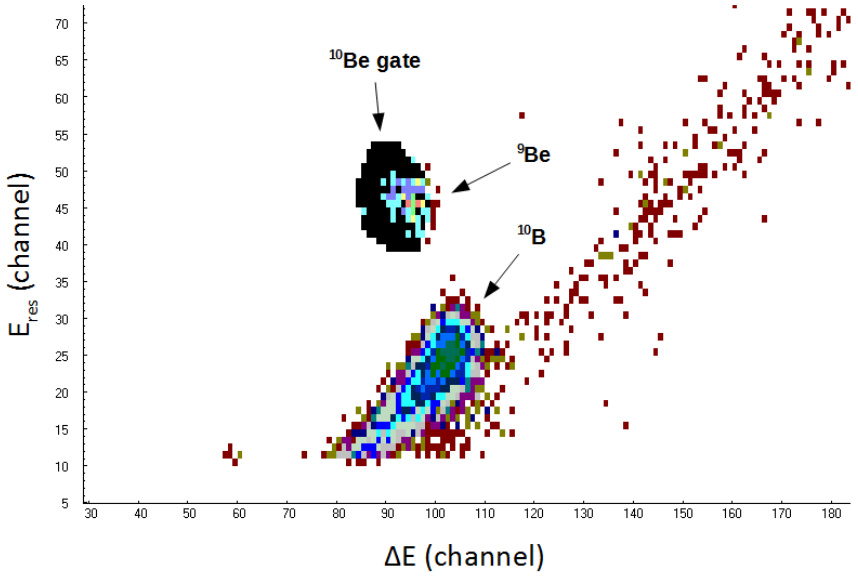

Figure 4.19: Blank spectra in the 1+2+ configuration with a 150 nm degrader at a stripping thickness of 0.09 μg/cm^2. The counts associated to scattered ^{9}Be are clearly recognizable after 15 minutes of acquisition and appear shifted from the center of the ^{10}Be gate.

sometimes, absorbers are also combined with degrader foils [68]. At terminal voltages below 1 MV, the poor resolution of ^{10}B and ^{10}Be compromises or even prevents the effectiveness of the technique. However, as it has been demonstrated at the Tandy facility, an appropriate design of the detecting system and of the absorber device can give a chance to apply this method also at terminal voltages below 0.6 MV [37].

Therefore, following the experience at the Tandy and the promising results described in Chapter 3 concerning $^{26}Al^{2+}$ measurements, the absorber technique has been also tested at the SARA system for ^{10}Be measurements. The experiments are realized with the absorber setup described in Section 3.5.1 with the 1+ and 2+ charge states at 1 MV terminal voltage. The absorber cell is constituted of an isobutane gas volume enclosed between two 5x5 mm^2 silicon nitride foils, with thicknesses of 500 and 75 nm, respectively (Figure 3.9). ^{10}Be ions in the 2+ charge state have a higher energy (2400 keV), for which a better separation from the ^{10}B peak is expected. The $^{10}Be^{1+}$ beam carries a lower energy, but it is still worth of being tested because of the higher transmission through the accelerator (55%, Figure 4.2), since it can still provide an elevate overall efficiency despite a worse resolution.

4.6.1 SRIM simulations

To have an idea of the effect of the absorber on the ^{10}Be and ^{10}B behaviour, several simulations with the SRIM tool have been performed.

At a beam energy of 1400 keV, absorber/GIC pressures above 40 mbar are necessary for a full ^{10}B suppression (Figure 4.20a). In Figure 4.20b, the residual energy of the isobars is plotted against the depth in the absorber and GIC for that pressure. In this case, ^{10}Be ions leave the absorber with an average residual energy of about 200 keV, whereas about 10% of ^{10}B ions enters the detector with an average energy of 10 keV, which is considerably lower than the ^{10}Be one. Even if the energy difference is sufficient to discriminate the isobars in the chamber, depending on the separation between the peaks it might be indispensable to work at increased absorber/GIC thicknesses. At a gas pressure of 45 mbar, ^{10}B is completely stopped into the absorber and ^{10}Be enters the

detector active volume with approximately 120 keV energy. As highlighted by Figure 4.21, ^{10}Be ions are affected by angular straggling, which increases the beam dimensions and prevents a fraction of the ions to pass the 5x5 mm^2 silicon nitride foil that separates the absorber from the detector. SRIM predicts an angular straggling of about 170 mrad for the ^{10}Be beam at an absorber pressure of 45 mbar, which should reduce the transmission to 70%, as the window angular acceptance is 175 mrad.

A similar set of simulations performed for the 2+ charge state reveals a sufficient ^{10}B suppression for absorber/GIC pressures above 70 mbar (Figures 4.22 and 4.22). At a pressure of 72 mbar, ^{10}B can't reach the detector, whereas ^{10}Be ions emerge with an average energy of 220 keV. Having an angular straggling of 110 mrad, almost 90% of the beam should be transmitted through the absorber (Figure 4.23).

SRIM simulations reveal the suitability of the 2+ charge state for ^{10}Be detection with the absorber setup. The higher energy than the 1+ has two positive effects indeed. First, as the range straggling is considerably lower than the one in the 1+ charge state, the separation between ^{10}Be and ^{10}B is expected to be better. In Figure 4.24, ^{10}B suppression factor is plotted as a function of the corresponding ^{10}Be residual energy (i.e. the energy of the ions that enter the active volume of the GIC). If the incoming beam energy is 2400 keV, a complete ^{10}B suppression is achieved at an absorber pressure that allows the entrance of ^{10}Be to the GIC with a residual energy of 220 keV, whereas in the case of a 1400 keV beam, ^{10}Be residual energy is just 160 keV. Second, the lower angular straggling into the absorber is expected to provide a higher transmission, making the measurements more efficient.

4.6.2 ^{10}Be detection with the passive absorber

Tests at the SARA facility concerning ^{10}Be with the passive absorber technique have required much more care than the ones with ^{26}Al, mainly because of the better separation from the interfering ^{13}C in the latter case.

The absorber/GIC pressures applied to suppress ^{10}B had to be slightly higher than the values provided by the SRIM simulations and in general pressure adjustments have

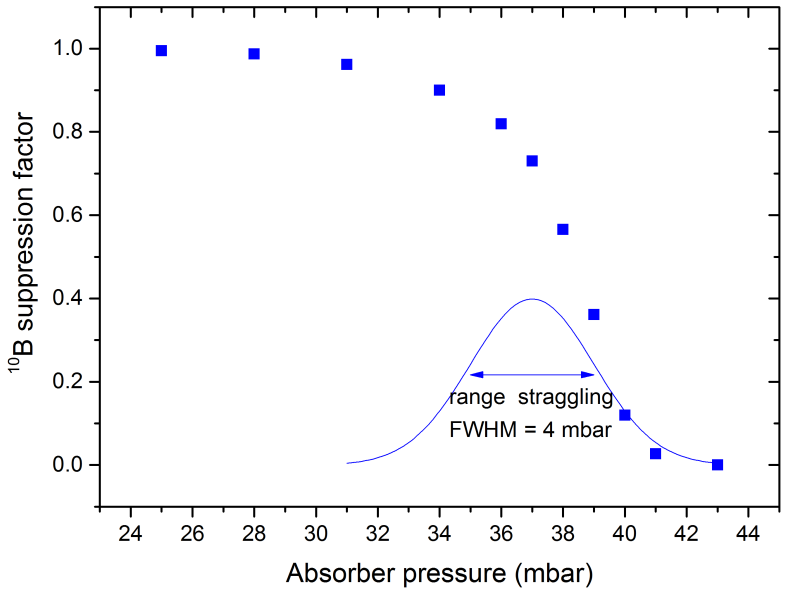

(a) ^{10}B suppression factor.

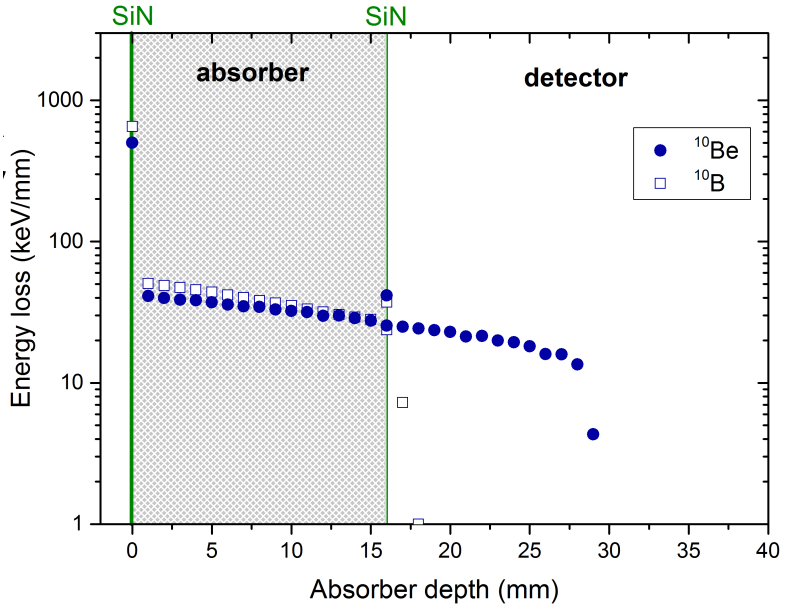

(b) ^{10}Be and ^{10}B energy loss assuming an absorber/GIC pressure of 40 mbar.

Figure 4.20: SRIM simulations of 1400 keV ^{10}Be and ^{10}B ions in the absorber/GIC.

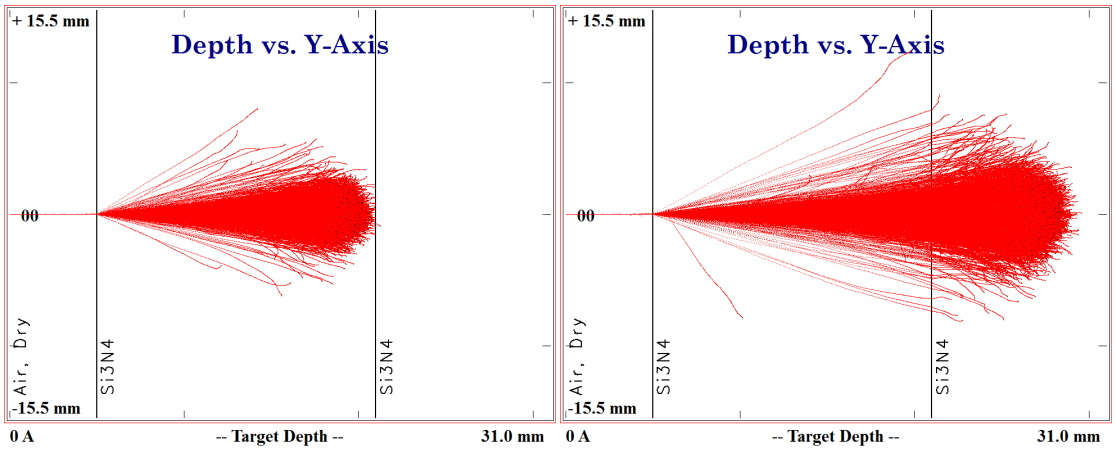

(a) ^{10}B (b) ^{10}Be

Figure 4.21: SRIM simulations of 1400 keV ^{10}Be and ^{10}B ions in the absorber/GIC at a gas pressure of 45 mbar.

been necessary very often during the experiments. Indeed, samples with a higher ^{10}B content or providing more intense beam currents had to be analyzed at an increased absorber thickness to further stop the interference before entering the chamber. Still, this absorber setup could be slightly affected by room temperature variations resulting in discrepancies with the theoretical predictions. Since ^{10}Be emerged from the absorber with a very low energy (about 100-200 keV according to SRIM simulations), peak has appeared in the total energy spectra at low ADC channels. Therefore, the electronic noise had to be minimized by an accurate grounding of the GIC housing and by removing any other of its sources, in order to suppress interfering signals and optimize the detector resolution. The plastic tube connecting the isobutane gas bottle and the detector volume needed frequent purging to keep the absorber/GIC gas as pure as possible.

Despite these difficulties, the isobars ^{10}Be and ^{10}B could be clearly identified both at 1400 and 2400 keV, obtaining residual energy spectra as the ones shown in Figure 4.25. The absorber/GIC pressures applied during the experiments have been high enough to stop ^{10}Be ions in the first anode.

$^{10}Be^{1+}$ arrives into the detector with an energy of 1400 keV. As illustrated in Figure

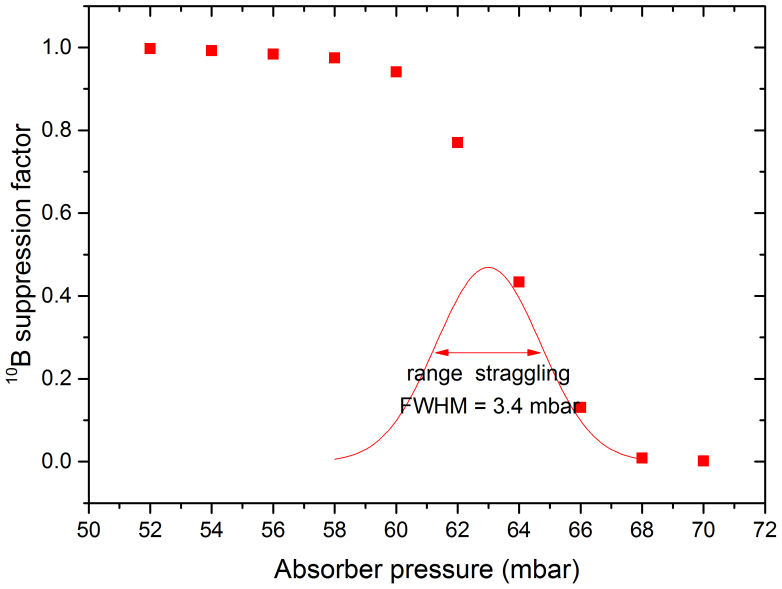

(a) ^{10}B suppression factor.

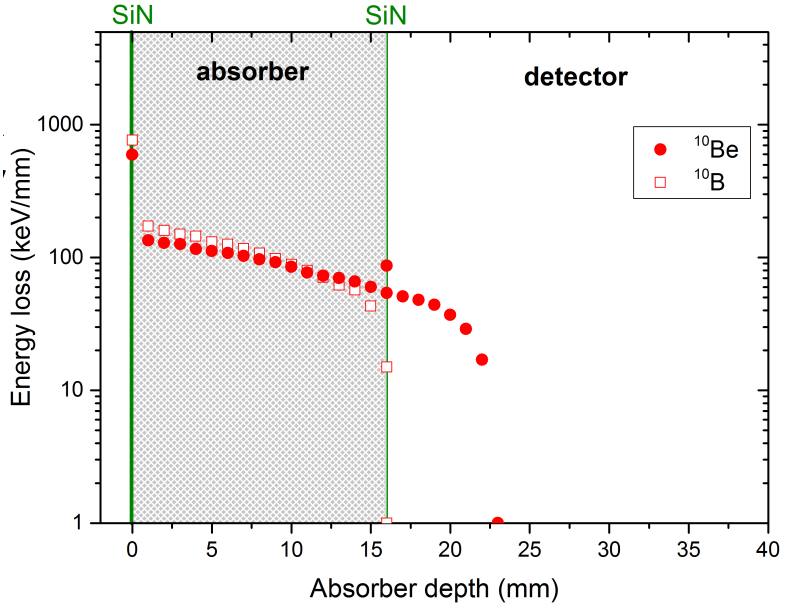

(b) ^{10}Be and ^{10}B energy loss assuming an absorber/GIC pressure of 80 mbar.

Figure 4.22: SRIM simulations of 2400 keV ^{10}Be and ^{10}B ions in the absorber/GIC.

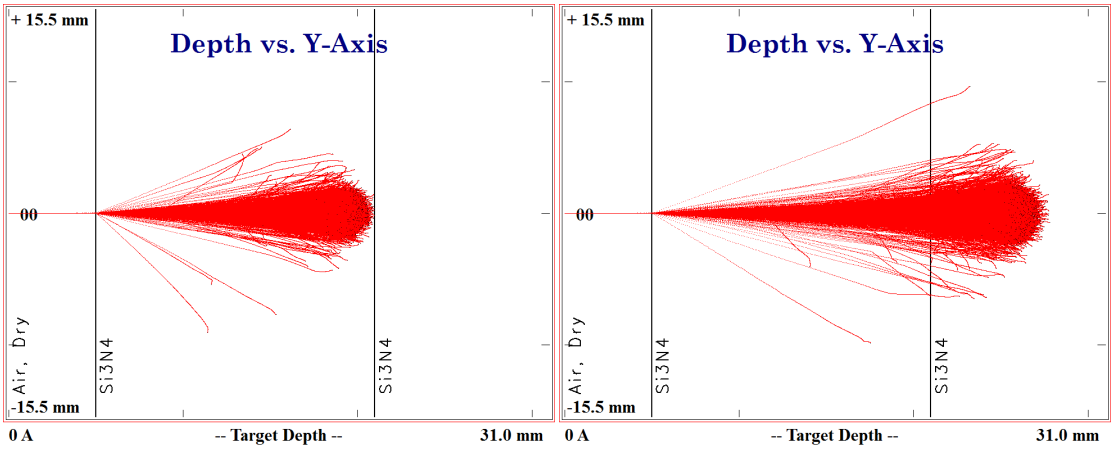

(a) ^{10}B (b) ^{10}Be

Figure 4.23: SRIM simulations of 2400 keV ^{10}Be and ^{10}B ions in the absorber/GIC at a gas pressure of 70 mbar.

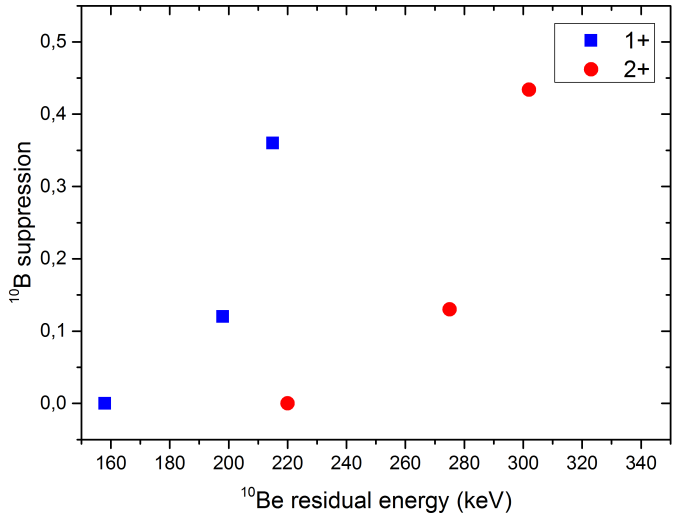

Figure 4.24: ^{10}B suppression factor plotted against the corresponding ^{10}Be.

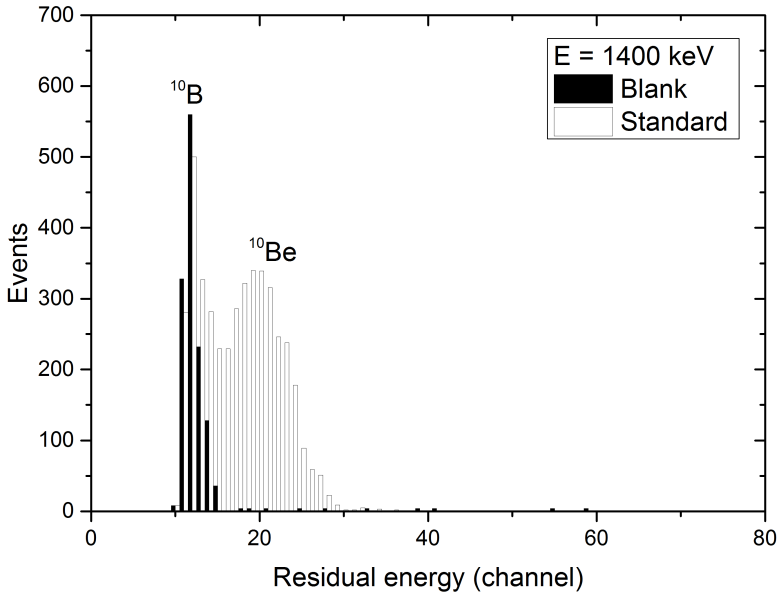

(a) 1+ charge state

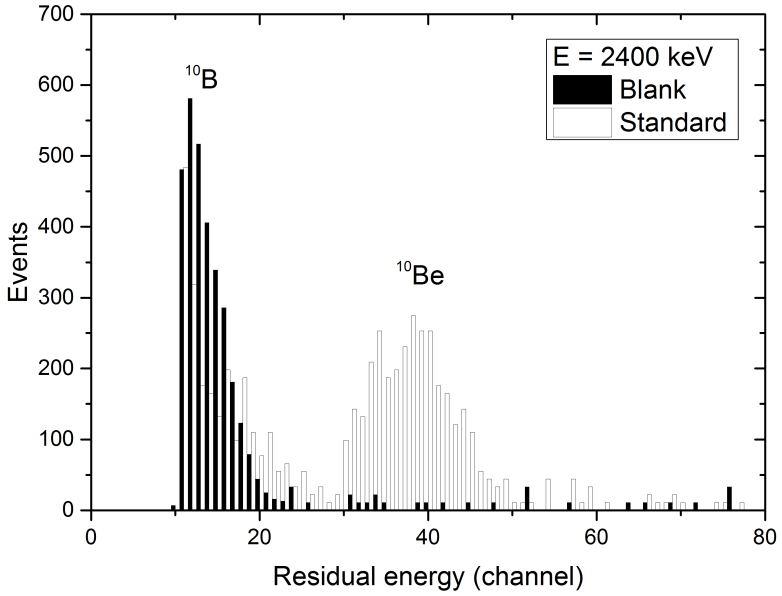

(b) 2+ charge state

Figure 4.25: ^{10}Be and ^{10}B spectra of the ETH standard sample (nominal ^{10}Be/^{9}Be ratio of $2.4 \cdot 10^{-10}$) with the passive absorber setup.

4.25a, ^{10}Be and ^{10}B peaks can be clearly identified in the residual energy spectrum. However, the ^{10}B high-energy tail overlaps the ^{10}Be peak, forcing to apply strict cuts to the energy signal or to increase the absorber/GIC gas pressure. By filling the detector with 47 mbar isobutane pressure, a complete ^{10}B suppression is achieved but a low-energy fraction of the ^{10}Be peak is lost.

^{10}Be in the charge state 2+ outgoes the accelerator set at 1 MV terminal voltage with an energy of 2400 keV. The transmission through the tandem at the stripper pressure needed to suppress molecular background is 18%. As evinced from Figure 4.25b, the separation between ^{10}Be and ^{10}B is much better because of the higher energy of the ions. ^{10}B could be completely stopped in the absorber by applying an isobutane pressure of 75 mbar without cutting the ^{10}Be peak. However, measurements have been complicated and in many cases nonviable due to the presence of a severe, continuous background that made hard to work with samples with isotopic ratios below 10^{-10}. Indeed, blank samples have provided ^{10}Be/^{9}Be ratios of several 10^{-11} and the ICN 01-5-1 standard normally used for precise transmission measurements was not even recognizable in the energy spectrum, having a nominal value of $2.7 \cdot 10^{-11}$ (Table 4.2). Just rough estimations could be therefore realized with the high-level ETH standard, revealing a ^{10}Be transmissions of about 60% through the absorber material.

4.6.3 Background

The identification of the different background sources is of help in the optimization of the measurements and the absorber/GIC setup.

In contrast to the degrader technique, a background contribution is represented by 10 u molecules that survive the stripping process and travel through the HE spectrometer to the absorber/GIC, breaking down in the first silicon nitride window. In the case of ^{9}Be^{1}H, which is the most abundant molecule, ^{9}Be originated in the break-up enters the absorber with about 9/10 of the ^{10}Be energy and reaches the active volume of the detector. Signals generated by ^{9}Be appear in the spectra as background events between the ^{10}B high-energy tail and the ^{10}Be peak. However, molecular background can be reduced by

increasing the stripper thickness in order to destroy ^{9}BeH molecules into the accelerator, so that ^{9}Be is removed by the HE spectrometer. In Figure 4.26, the exponential decrease of the background count rate with the stripper thickness is represented for beam energy of 1400 keV, showing a full molecular suppression at 0.12 μg/cm^2 which correspond to a 52% transmission through the accelerator (Figure 4.2). In this configuration, a 32% transmission through the absorber is measured, with a background of $3 \cdot 10^{-13}$. Therefore, an overall efficiency of 17% is achieved, which is three times higher than the maximum one detected with the degrader technique.

Once the molecular interference is discarded, the presence of a continuous background becomes evident in the energy spectrum and is extremely intense at 2400 keV. The background count rates are estimated at different beam energies and results in the sigmoid plot in Figure 4.27, presenting a jump of two orders of magnitude between 1700 and 2100 keV.

Two different processes might be responsible for this background: (i) the ^{10}B(p, α)^{7}Be reaction and (ii) Rutherford scattering of ^{10}B on protons. These two reactions involve the ^{10}B present in the incoming beam and the protons contained in the absorber, which are abundant both in the silicon nitride foils ($Si_3N_{3.1}H_{0.06}$ [27]) and in the isobutane gas (C_4H_{10}).

The ^{10}B(p, α)^{7}Be nuclear reaction occurs between ^{10}B and protons and results in α and ^{7}Be particles. Because the Q value is 1.15 MeV [90], products maximal energies in the forward direction are higher than the initial ^{10}B nuclides, explaining the extension of the background toward higher channels than the ones where the ^{10}Be peak lies. The count rate R [s^{-1}] of the induced events can be expressed with the formula:

$$R = \sigma \cdot \frac{I \cdot N_T}{A} \tag{4.8}$$

where I [s^{-1}] is the beam intensity, N_T is the number of the target protons, A [m^2] is the irradiated area and σ [m^2] is the reaction cross section. The dependency of R on the ^{10}B energy is contained in the cross section, which rapidly increases with the projectiles energy in the range studied at the SARA facility (Figure 4.28). This means

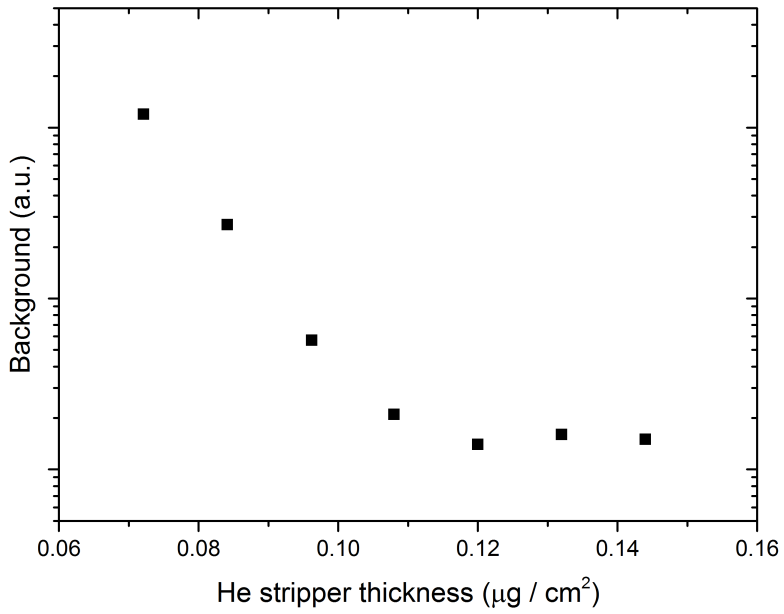

Figure 4.26: $^{10}Be^{1+}$ background events recorded as a function of the stripper gas pressure.

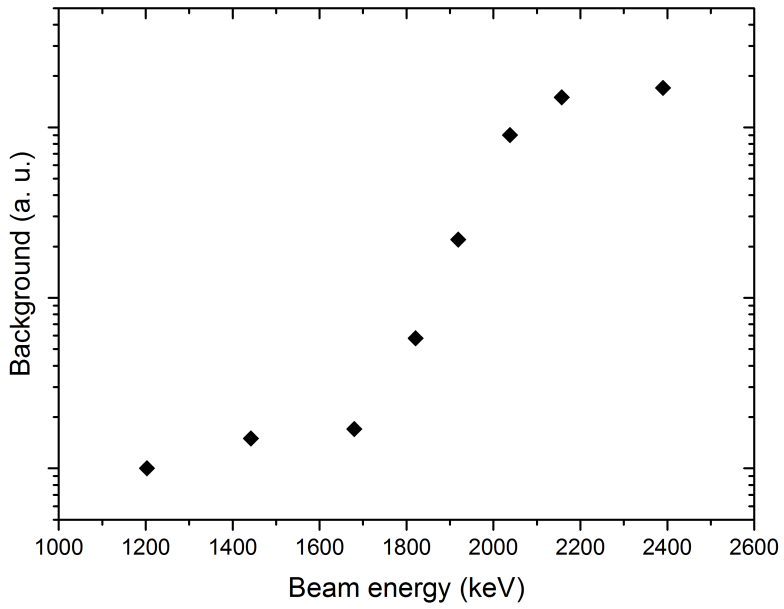

Figure 4.27: Background count rate as a function of the beam energy.

that the probability for the ^{10}B(p, α)^{7}Be reaction to occur is maximal at the first silicon nitride foil of the absorber, since the ^{10}B ions have maximal energies when they hit it. $\sigma \approx 10^{-4} - 10^{-2}$ b [5] can be extrapolated for ^{10}B beam hitting the 500 nm membrane with energies between 1400 and 2400 keV [91].

For a 2.4 MeV ^{10}B beam, the resulting α and ^{7}Be would have maximal energies of about 3.5 MeV. According to SRIM simulations, the most energetic α particles emerge the absorber with a residual average energy of 2.9 MeV if the gas pressure is 72 mbar. Those α are not stopped in the first GIC anode and lose about 2.1 MeV of energy there. On the contrary, a 3.5 MeV ^{7}Be would pass the absorber and enter the chamber with an energy of about 640 keV, which would be completely released into the first anode creating a signal at much higher channels than ^{10}Be. However, taking into account that the energy of both products can be lower, both α and ^{7}Be particles could be responsible for background events.

The second contribution to the background is represented by Rutherford scattering of ^{10}B on protons, which are knocked out from the first absorber window with a maximal energy:

$$E_{max} = \frac{4 m_H m_B}{(m_H + m_B)^2} \cdot E_B \approx \frac{E_B}{3} \tag{4.9}$$

where m_H and m_B are the colliding particles masses and E_B the incoming beam energy. For E_B = 2400 keV, scattered protons in the 500 nm silicon nitride foil have maximal energies E_{max} of about 800 keV. According to the SRIM simulations presented in Section 4.6.1, if the absorber pressure is set at 72 mbar, ^{10}B is completely stopped into the absorber volume whereas ^{10}Be accesses the detector active area with a residual energy of 220 keV. In these conditions, the 800 keV protons produced in the first foil enter the GIC with a residual energy of 630 keV. An evidence of the occurrence of scattering is represented by the peak generated by H entering the detector with the maximal energy, which is normally well visible in the residual energy spectra of 2400 keV beams (Figure 4.29). The continuous background at lower channels stems from (i) non-central collisions that generate slow protons and (ii) the interactions at different foil thicknesses where ^{10}B

[5] 1 b = 10^{-24} cm^2.

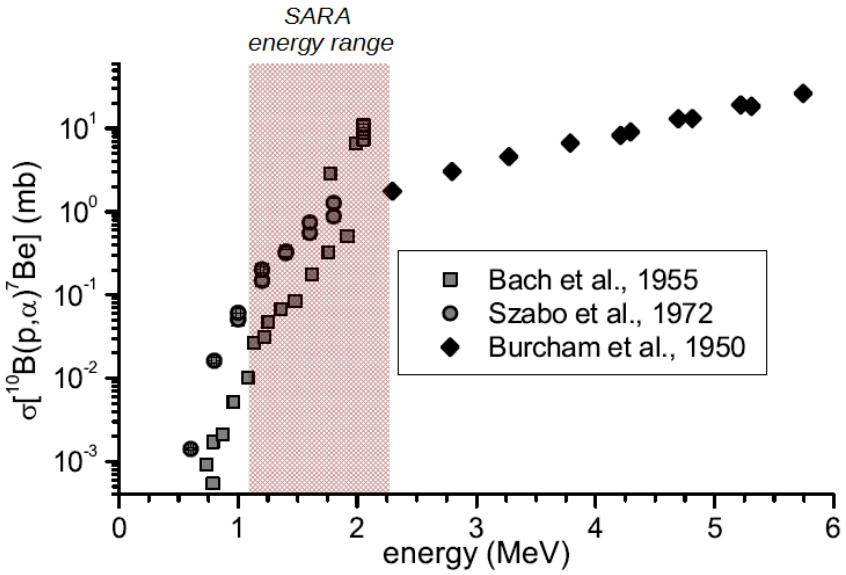

Figure 4.28: Cross section data of the ^{10}B(p, α)^{7}Be reaction from [91, 92, 93].

already lost part of the initial energy.

The Rutherford scattering differential cross section is given by the Formula:

$$\frac{d\sigma}{d\Omega} = \left(\frac{Z_H Z_B e^2}{4\pi\epsilon_0 E_B}\right)^2 \left(1 + \frac{M_B}{M_H}\right)^2 \frac{1}{cos^3\phi} \tag{4.10}$$

where Z_H and M_H are the protons atomic number and mass, respectively, Z_B, M_B and E_B are the boron atomic number, mass and energy, respectively, and ϕ is the scattering angle. The cross section results by the integration between 0 (assuming the beam hits the entrance window in the centre) and $\phi_{max} = 0.16$, which is determined by the geometrical characteristics of the absorber (i.e. the absorber length the and silicon nitride foils dimensions):

$$\sigma = \int_0^{\phi_{max}} \frac{d\sigma}{d\Omega} \cdot 2\pi sin\phi \cdot d\phi \tag{4.11}$$

In the energy range between 1400 and 2400 keV and for the examined absorber design, the Rutherford cross section is of 3-4 orders of magnitude higher than the one of the ^{10}B(p, α)^{7}Be reaction [37], so that process might be the main source of the observed background.

The Rutherford scattering occurs primarily in the first 500 nm silicon nitride foil. If the beam initial energy is 2400 keV, ^{10}B ions reach the absorber gas volume with a residual energy of 1600 keV, which is high enough to accelerate isobutane protons into the active volume of the detector. An explanation for the drastically reduced background at beam energies below 1700 keV is that in this case the absorber gas is not such an important contribution because of the too low ^{10}B residual energy. The second silicon nitride window does not contribute to the continuous background because ^{10}B ions have already lost the most of their energy when they hit it.

4.6.4 Absorber setup optimization: the stack of foils

The experiments carried out at the SARA facility clearly demonstrate the potential of the passive absorber technique for ^{10}Be measurements. Already with this very simple setup, indeed, an overall efficiency of 17% (52% 1+ charge state transmission through the accelerator, 32% transmission through the absorber device) is achieved at the beam energy of 1400 keV, which is three times higher than the obtained one with the degrader technique. At 2400 keV, the passive absorber provides an excellent separation between ^{10}Be and ^{10}B, but in this case the measurements are impeded by an intense protons background.

Therefore, the absorber installed during the experiments represents a proof of concept which provides useful information to enhance the setup and make it routinely usable.

First of all, the detecting system can be further improved to increase the separation between ^{10}Be and ^{10}B. The ETH GIC is equipped with CREMAT preamplifiers, whose characteristics are suitable for the normal operation involving 1-4 MeV ions. At lower energies, CoolFET® preamplifiers from Amptek [94] provide higher resolution and present general better performance [95]. Since ^{10}Be accesses the active volume of the detector after passing through the absorber with extremely low energies (100-200 keV), a better resolution is expected by the replacement of the preamplifiers. However, such a modification is not so easy, since CREMAT's modules are welded on the GIC anodic plates, whereas the CoolFETs should be placed externally the detector housing and

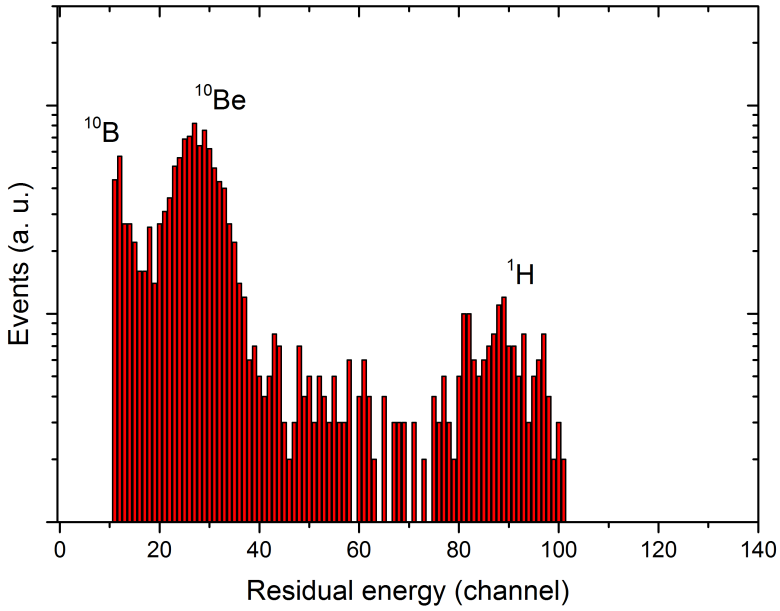

Figure 4.29: Residual energy spectrum of the ETH standard. The incoming 10 u beam carries a 2400 keV energy.

connected to the anodes through N type cables. Thus, the CoolFET preamplifiers would require substantial changes to the current detector design.

The most important aspect to work on is the continuous background caused by scattered protons into the absorber. The use of materials with reduced protons content should therefore be preferred. Since the absorber gas is an important target at 2400 keV beam energy, the use of another gas with less protons than isobutane, e.g. Ar, should provide better performance.

The first silicon nitride foil is the main source of the continuous background since contains an elevate amount of protons and ^{10}B ions hit it with the highest energy. The use of a thinner membrane is not expected to be of any help. The amount of H in the silicon nitride foils is hard to predict, since it can change for different batches of membranes and the reported stechiometry of $Si_3N_{3.1}H_{0.06}$ in [27] was derived on a much thinner one (35 nm). In [37], the hypothesis has been put forward that protons are mainly contained in the outer layers and not equally distributed over the whole depth of the foil. This would

imply that a thinner membrane could have the same content of protons than a thicker one [27, 57]. On the other hand, a thinner foil would increase the transmission through the absorber by reducing the beam angular straggling.

Working with the ΔE and E_{res} signals from both anodes gives a chance to discriminate ^{10}Be from the protons background. This is not possible with the setup used during the experiments because the absorber gas volume and the GIC are connected. One way to work in two anodes is to use an absorber whose gas feeding line is independent from the GIC one. This might provide the possibility of using different gases at different pressures. However, a dedicated gas handling is needed for the absorber, which requires changes to the whole detector housing design as described in [60].

Another option consists in using a passive absorber based on a stack of silicon nitride foils as the one routinely adopted at the 3 MV VERA facility for ^{10}Be measurements at a beam energy of 7 MeV [67]. In such a setup, the GIC window holder is designed to host several silicon nitride foils positioned on a metallic dedicated holder (see Figure 4.30). The main disadvantage is that the absorber thickness cannot be rapidly changed once the absorber is mounted, forcing to adjust the beam energy instead.

In order to make a comparison between different absorber designs, some experiments have been carried out at VERA with a ^{10}Be beam of 2400 keV and an stack of foils absorber, within a collaboration with the Isotope Research and Nuclear Physics group of the University of Vienna. Since VERA can operate at terminal voltages between

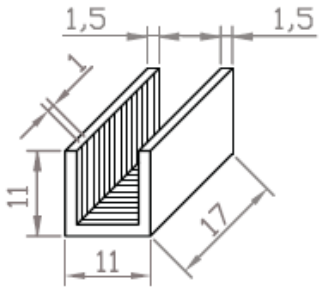

Figure 4.30: Holder for the silicon nitride foils at VERA [67].

1.6 and 3 MV, the 1+ charge state is selected at the exit of the accelerator at 1.7 MV, resulting in a 2400 keV beam energy which is the same of the $^{10}Be^{2+}$ at SARA at 1 MV. According to SRIM simulations, the thickness of a passive absorber based exclusively on silicon nitride foils should range between 2.35 and 2.60 μm (i.e. between 810 and 890 μg/cm^2 mass thicknesses), where a complete ^{10}B suppression is achieved without affecting the ^{10}Be transmission in a relevant way. During the experiments, two 1 μm thickness foils have been inserted in the holder and a 0.5 μm thick membrane has been mounted as a detector entrance window, obtaining a total silicon nitride thickness of 2.5 μm (860 μg/cm^2 mass thickness). All the foils have an area of 10x10 mm^2 to maximize the beam angular acceptance. Results can be directly compared since VERA and SARA's gas ionization chambers are based on the same design from the ETH AMS group [96], with the only difference that the GIC anodes at VERA have a length of 3 cm, i.e. they are slightly shorter than the 5 cm ones at SARA. A schematic representation of the experimental setup used at VERA to test the passive absorber at low energies is given in Figure 4.31.

Despite the lack of time, for which mainly qualitative conclusions have been reached, very promising results have been obtained. By setting a GIC isobutane pressure to about 10 mbar, 2D spectra as the ones given in Figure 4.32 were acquired at VERA, where ^{10}Be can be clearly recognized. The total count rate recorded in the first anode was sufficiently low to suggest that ^{10}B ions were completely stopped in the absorber foils. It is remarkable to point out that the standard material used in these experiments to identify the ^{10}Be peak has the rather low nominal ratio of $(1.70 \pm 0.03) \cdot 10^{-12}$ and that it could not be identified in the absorber setup tested at SARA because of the intense protons background originated by Rutherford scattering of ^{10}B on the silicon nitride foils, as discussed in Section 4.6.3. Scattered protons are obviously produced also at the VERA absorber setup and pass through all the foils, reaching the active volume of the GIC with a maximal energy of about 600 keV. However, because of the low isobutane pressure, they are not stopped into the detector and release a very little energy in the two GIC sections (about 75 keV in both the 3 cm lenght anodes), generating signals at low

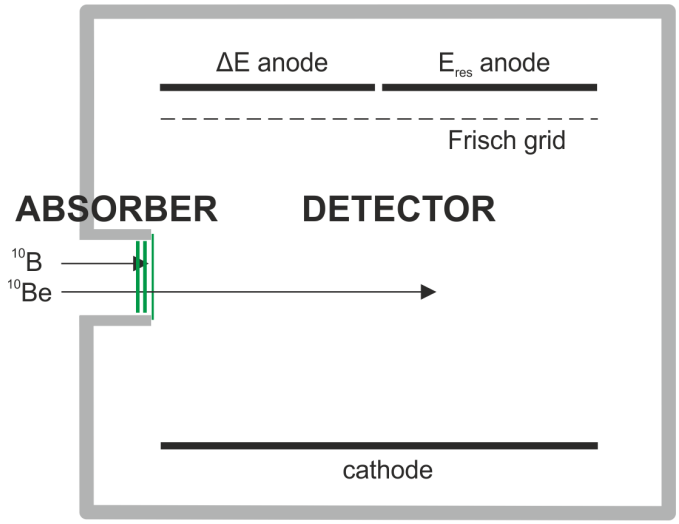

Figure 4.31: Schematic representation of the absorber/GIC setup used during the experiments at VERA.

channels that don't interfere with the ^{10}Be detection.

The intensity of the peak that appears in the spectrum at lower channels than ^{10}Be presents a strong dependency on the stripper pressure, and therefore it is identified as ^{9}Be originating from the break-up of ^{9}Be^{1}H molecules in the first absorber foil. It represents the main background source since some of those events enter the ^{10}Be gate. A full molecular suppression would require the application of too elevate stripper pressures and result in a severe efficiency reduction. At a stripper pressure high enough to remove the most of the molecules but corresponding to a reasonable beam transmission through the accelerator, the background from the ^{9}Be molecular fragments forces to apply strict selections to the accepted signals. In this configuration, a transmission of about 20% through the absorber with a background ^{10}Be/^{9}Be ratio of few 10^{-14} is measured.

Thus, the experiments conducted at VERA demonstrate that ^{10}Be measurements with a stack of foils absorber are actually possible also at SARA's beam energies. The potential of this technique lies in the fact that the transmission through the absorber without applying strict cuts is about 75%. Since ^{9}Be molecular fragments are the main cause of background, the use of silicon nitride foils with a smaller area (i.e. less angular

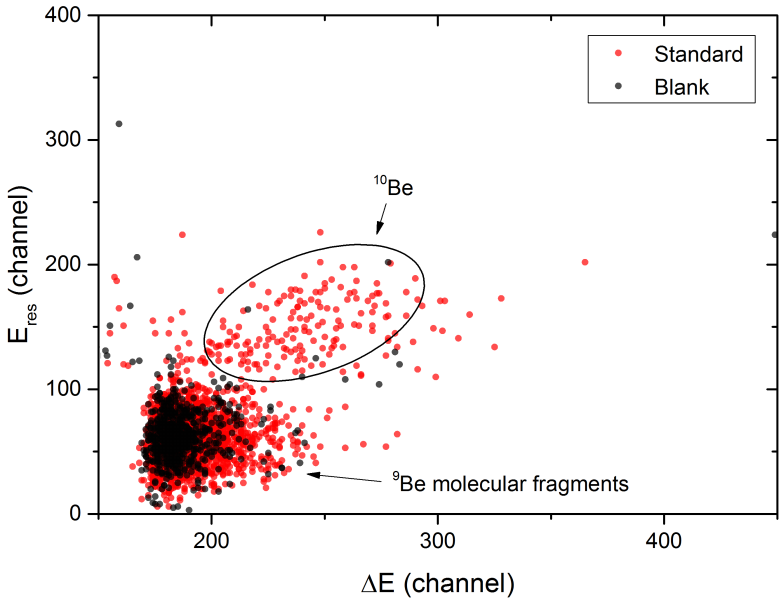

Figure 4.32: 2D ^{10}Be spectra acquired at the VERA facility with an absorber constituted of silicon nitride foils at a beam energy of 2400 keV.

acceptance) is expected to be of benefit. Indeed, molecular fragments result from a break-up with some angle relative to the beam direction and necessarily have a wider angular straggling than ^{10}Be ions. However, further tests and experiments are required to have more quantitative information.

4.7 Conclusions

Different approaches were investigated during the last years at the SARA facility in order to improve ^{10}Be measurements. After the installation of the He stripper and the ETH detector, the degrader and the passive absorber techniques were both studied in order to determine the optimal method with the current setup on BeO samples.

Two parameters play a role in the investigated techniques: the overall efficiency, which depends on the transmission through the accelerator and the HE spectrometer, and the background. The transmission through the accelerator did not present relevant

variations after the replacement of the stripper, having similar values with both Ar and He.

The study developed in Section 4.5 accurately defines the optimal measurement conditions at the upgraded SARA setup with the degrader technique. The 1+2+ and 2+2+ charge state configurations at 1 MV terminal voltage have similar performances and are characterized by the highest efficiencies (5-6%) and the lowest backgrounds ($2 - 4 \cdot 10^{-14}$). Nevertheless, because of its lower background of $2 \cdot 10^{-14}$ and ease of managing, the 2+2+ configuration has been identified as the most suitable for the routine measurements.

The work described in Section 4.6 definitely highlights the passive absorber as a very a promising technique for ^{10}B suppression at beam energies below 3 MeV. The proof-of-concept absorber setup tested at SARA has shown a very good separation between ^{10}Be and its isobar. In this context, the optimal resolution provided by the ETH GIC plays a fundamental role. At 1400 keV beam energy, an overall efficiency of 17% is achieved with a background of few 10^{-13}. Even if the discrimination between ^{10}Be and ^{10}B improved at the beam energy of 2400 keV, further investigations are necessary to remove the background from scattered protons.

The parameters for the ^{10}Be detection conditions with both the degrader and the absorber techniques are recapped in Table 4.10. The overall efficiency provided by the absorber method is 2-3 times higher than the one obtained with the degrader, even if the tested absorber setup was not optimized. Hence, the question arises on how modifying the absorber design in order to reduce the background and make such a technique suitable for ^{10}Be measurements.

The tested absorber at SARA imposes too strict conditions for ^{10}Be detection, since the absorber thickness for ^{10}B suppression is determined by its gas pressure and coincides with the GIC gas pressure. This setup forces to detect ^{10}Be in the first anode of the detector. The experiments conducted at VERA demonstrated that acquiring ^{10}Be signals from the two anodes of the GIC is the key for background improvement at a beam energy of 2400 keV. With an absorber based on a stack of silicon nitride foils, it was demonstrated at

Table 4.10: Measurement parameters with the different ^{10}B suppression techniques.

^{10}B suppression technique	Degrader foil		Passive absorber	
Charge states configuration	1+2+	2+2+	1+	2+
Terminal voltage (kV)	1000	1000	1000	1000
Beam energy (keV)	1400	2400	1400	2400
He stripper thickness (μg/cm^2)	0.03	0.03	0.12	0.12
Accelerator transmission (%)	58	21	52	19
Degrader thickness (nm)	100	100	-	-
HE transmission (%)	10	23	32	≈ 60
Overall efficiency (%)	6	5	17	≈ 11
Background[a](10^{-14})	4.1	2.5	32	≈ 1000

[a] Background levels are measured with an error $\sigma = 20\%$.

VERA that efficient ^{10}Be measurements are possible, with transmission and background values comparable to the ones of the degrader technique. Still, the absorber performance is expected to improve by adjusting the foils dimensions and positions in the dedicated holder.

Even if further studies and experiments are needed to find the optimal absorber design, the work described in this chapter shows the potential of such a tecnhiques at LE-AMS facilities as SARA and opens to new possibilities for more efficient ^{10}Be measurements.

Chapter 5

Conclusions

A detailed analysis has been performed during the course of this PhD project to define the optimal measurements conditions for light ions at the SARA facility, whose recent upgrades consisted in the implementation of He as a stripping gas and a high-resolution rare isotope detector.

After a preliminary study of the general performance of the upgraded facility with different radionuclides, the work focused on the optimization of ^{10}Be and ^{26}Al measurements, which has been accomplished in both cases by dividing the problem in two steps. First, the overall efficiency has been studied, including the transmission through the accelerator equipped with the new stripper and the transmission through the HE spectrometer. Second, the different background sources have been identified. Then, the optimal measurement conditions have been defined, having the necessity of a compromise between high efficiency and low background.

In order to obtain a reasonable suppression against interfering species, the degrader and the passive absorber techniques have been deeply analyzed. The first method consists in the insertion of a thin foil in the beam path before a magnetic or electrostratic deflector, which separates the radionuclide of interest from an isobaric interference by taking advantage of their different energy loss in the membrane. In the second method, an absorber cell is placed at the entrance of the rare isotope gas ionization chamber. The

absorber mass thickness has to be balanced to achieve the desired interference suppression with low losses of the studied radionuclide.

In the following, a short review of the main results described along the thesis and future perspectives will be presented.

5.1 Recent upgrades

The stripping process is a key phase of the AMS technique, as it determines both the molecular interference suppression and the measurement efficiency. After the replacement of the originally installed Ar stripper with one based on He gas, the behaviour of several nuclides through the new stripper has been investigated. In the energy range allowed at SARA, heavy ions such as ^{129}I and actinides benefit from He stripping and present high transmissions through the accelerator in the 3+ charge state. In the case of light ions, instead, no particular improvement has been detected with the new stripper.

The new gas ionization chamber installed at the end of the beam line as the rare isotope detector has a compact design with minimized electronic noise. Its installation improved light ions resolutions and offered the opportunity of testing the passive absorber as an interference suppression technique for both ^{10}Be and ^{26}Al, for which the detector performance was essential.

5.2 ^{26}Al measurement optimization

Concerning ^{26}Al, the 1+, 2+ and 3+ charge states resulted to be the most populated at the exit of the accelerator. The 3+ charge state has been identified as the most suitable for routine measurements, having an efficiency of 17% and a background of few 10^{-14}. The 2+ charge state is characterized by a very high transmission through the accelerator (close to 60%), but unfortunately is affected by the intense ^{13}C interference. Tests carried out with a simple absorber setup were very promising, showing an efficiency of 22% with a background at levels of 10^{-13} and demonstrating the potential of such a technique

for $^{13}C^{1+}$ suppression during $^{26}Al^{2+}$ detection.

5.3 ^{10}Be measurement optimization

^{10}Be AMS has always to deal with the intense ^{10}B presence, which requires dedicated suppression techniques. To remove ^{10}B interference at SARA, the degrader and the passive absorber methods have been both investigated.

The degrader is probably the most conventional way to measure ^{10}Be through AMS. After ions' passage through the degrader, severe beam losses take place in the HE spectrometer, which are caused by the charge state distribution and by the beam energy and angular stragglings after the foil. The different efficiency loss contributions have been quantitatively estimated, taking into account that scattered ^{9}Be is the main cause of background in this context. The 2+2+ charge state configuration turned out as the most adapt for the measurements, with an efficiency of 5-6% and a background of few 10^{-14}.

Different experiments with passive absorbers have been carried out at SARA and VERA at ^{10}Be energy of 2.4 MeV, demonstrating the feasibility of such a technique with a proper detecting system and absorber design. However, further studies are needed to make the application of passive absorbers be routinely usable.

5.4 Outlook

The results obtained in the last years with ^{10}Be and ^{26}Al allow to measure real samples with the current SARA setup in the optimal way. The AMS research line at the CNA is not limited to light ions: indeed, the measurement of other radionuclides such as ^{41}Ca, ^{129}I and actinides is currently undergoing an optimization work similar to the one presented for ^{10}Be and ^{26}Al in this thesis. Even if radiocarbon is measured at the CNA almost exclusively with the ^{14}C-dedicated MICADAS facility, the effects of He stripping on such nuclide are going to be investigated at SARA as well. Preliminary tests haven't shown any particular improvement in this case, but more work is required, which would

complete the study concerning the most common light ions measured through the AMS technique.

Other technical developments are scheduled in the future to improve even more the facility performance. Concerning ^{10}Be and ^{26}Al, the collected information about the absorber technique at SARA's energies definitely encourage towards further studies. Since the results obtained with very simple absorber designs were very promising, other tests and experiments are worth to be carried out in order to reach an improved version capable to pass over the issues of the current setups.

Furthermore, to improve heavy ions measurements, a time-of-flight detector is going to be designed and installed in order to study the actinides background contributions and to measure extremely low-level samples.

Bibliography

[1] R.C. Finkel and M. Suter. *AMS in Earth sciences: technique and applications*. JAI Press Inc., 1993.

[2] A.E. Litherland. Accelerator mass spectrometry. *Nuclear Inst. and Meth. B*, 5(2):100–108, 1984.

[3] L.K. Fifield. Accelerator mass spectrometry and its applications. *Rep. Prog. Phys.*, 62(8):1223–1274, 1999.

[4] M. Suter. 25 years of AMS - A review of recent developments. *Nucl. Instr. Meth. B*, 223-224:139–148, 2004.

[5] W. Kutschera. Progress in isotope analysis at ultra-trace level by AMS. *Int. J. Mass Spectrom.*, 242(2-3):145–160, 2005.

[6] H.-A. Synal and L. Wacker. AMS measurement technique after 30 years: Possibilities and limitations of low energy systems. *Nucl. Instr. Meth. B*, 268(7–8):701 – 707, 2010.

[7] H.-A. Synal. Developments in accelerator mass spectrometry. *Int. J. Mass Spectrom.*, 349–350:192–202, 2013.

[8] C.L. Bennett, R.P. Beukens, and M.R. Clover. Radiocarbon dating using electrostatic accelerators: Negative ions provide the key. *Science*, 198:508–510, 1977.

[9] D.E. Nelson, R.G. Korteling, and W.R. Stott. Carbon-14: Direct detection at natural concentrations. *Science*, 198(4316):507–508, 1977.

[10] M. Suter, St. Jacob, and H.A. Synal. AMS of ^{14}C at low energies. *Nucl. Instr. Meth. B*, 123(1-4):148–152, 1997.

[11] H.-A. Synal, S. Jacob, and M. Suter. New concepts for radiocarbon detection systems. *Nucl. Instr. Meth. B*, 161:29–36, 2000.

[12] M.G. Klein, D.J.W. Mous, and A. Gottang. A compact 1 MV multi-element AMS system. *Nucl. Instr. Meth. B*, 249:764–767, 2006.

[13] M.G. Klein, van Staveren H.J., D.J.W. Mous, and A. Gottang. Performance of the compact HVE 1 MV multi-element AMS system. *Nucl. Instr. Meth. B*, 259:184–187, 2007.

[14] T. Schulze-König, M. Seiler, M. Suter, L. Wacker, and H.-A. Synal. The dissociation of ^{13}CH and $^{12}CH_2$ molecules in He and N_2 at beam energies of 80–250 keV and possible implications for radiocarbon mass spectrometry. *Nucl. Instr. Meth. B*, 269:34–39, 2011.

[15] C. Vockenhuber, A. Alfimov, M. Christl, J. Lachner, T. Schulze-König, M. Suter, and H.-A. Synal. The potential of He stripping in heavy ion AMS. *Nucl. Instr. Meth. B*, 284:382–386, 2013.

[16] S. Maxeiner. *Optimizing the designs of next-generation AMS systems*. PhD thesis, ETH-Zürich, 2016.

[17] M.G. Klein. Personal communication, 2017.

[18] E. Chamizo, J.M. López-Gutiérrez, A. Ruiz-Gómez, F.J. Santos, M. García-León, C. Maden, and V. Alfimov. Status of the compact 1 MV AMS facility at the Centro Nacional de Aceleradores (Spain). *Nucl. Instr. Meth. B*, 266:2217–2220, 2008.

[19] E. Chamizo, F.J. Santos, J.M. López-Gutiérrez, S. Padilla, M. García-León, J. Heinemeier, C. Schnabel, and G. Scognamiglio. Status report of the 1 MV AMS facility at the Centro Nacional de Aceleradores. *Nucl. Instr. Meth. B*, 361:13–19, 2015.

[20] H.-A. Synal, M. Stocker, and M. Suter. MICADAS: A new compact radiocarbon AMS system. *Nucl. Instr. Meth. B*, 259:7–13, 2007.

[21] E. Chamizo. *Medida de isótopos de plutonio, ^{239}Pu y ^{240}Pu, mediante espectrometría de masas con aceleradores de baja energía*. PhD thesis, Universidad de Sevilla, 2009.

[22] M. Arnold, S. Merchel, D.L. Bourlès, R. Braucher, L. Benedetti, R.C. Finkel, G. Aumaître, A. Gottdang, and M. Klein. The French accelerator mass spectrometry facility ASTER: Improved performance and developments. *Nucl. Instr. Meth. B*, 268:1954–1959, 2010.

[23] M.G. Klein and D.J.W. Mous. Technical improvements and performance of the HVE AMS sputter ion source SO-110. *Nucl. Instr. Meth. B*, 2016.

[24] M. Suter, R. Balzer, G. Bonani, and W. Wölfli. A fast beam pulsing system for isotope ratio measurements. *Nucl. Instr. Meth. B*, 5:242–246, 1984.

[25] L. Calcagnile, G. Quarta, M. D'Elia, A. Gottdang, M. Klein, and D.J.W. Mous. Radiocarbon precision tests at the Lecce AMS facility using a sequential injection system. *Nucl. Instr. Meth. B*, 215:561–564, 2004.

[26] D.J.W. Mous, J. Visser, A. Gottdang, and R.G. Haitsma. A new range of high-current Tandetron™ accelerator systems with terminal voltages of 1–6 MV. *Nucl. Instr. Meth. B*, 219–220:480–484, 2004.

[27] M. Döbeli, C. Kottler, M. Stocker, S. Weinmann, H.-A. Synal, M. Grajcar, and M. Suter. Gas ionization chambers with silicon nitride windows for the detection and identification of low energy ions. *Nucl. Instr. Meth. B*, 219:415–419, 2004.

[28] FAST ComTec Communication Technology GmbH. MPA-NT Multiparameter System Software. `http://www.fastcomtec.com/fwww/datashee/mpa/mpant.pdf`, 2015.

[29] R. Middleton. *A Negative-Ion Cookbook*. 1989.

[30] M. Grajcar. *New concepts of ^{10}Be Accelerator Mass Spectrometry at low energies*. PhD thesis, ETH-Zürich, 2005.

[31] M. López Lora. PhD thesis, Universidad de Sevilla, ongoing.

[32] J. Lachner, M. Christl, C. Vockenhuber, and H.-A. Synal. Detection of UH^{3+} and ThH^{3+} molecules and ^{236}U background studies with low-energy AMS. *Nucl. Instr. Meth. B*, 294:364–368, 2013.

[33] H.-A. Synal, T. Schulze-König, M. Seiler, M. Suter, and L. Wacker. Mass spectrometric detection of radiocarbon for dating applications. *Nucl. Instr. Meth. B*, 294:349–352, 2013.

[34] M. Seiler, S. Maxeiner, L. Wacker, and H.-A. Synal. Status of mass spectrometric radiocarbon detection at ETHZ. *Nucl. Instr. Meth. B*, 361:245–249, 2015.

[35] S.R. Winkler, P. Steier, J. Buchriegler, J. Lachner, J. Pitters, A. Priller, and R. Golser. He stripping for AMS of ^{236}U and other actinides using a 3 MV tandem accelerator. *Nucl. Instr. Meth. B*, 361:458–464, 2015.

[36] A. Wittkower and H. Betz. Equilibrium-charge-state distributions of 2-15 MeV tantalum and uranium ions stripped in gases and solids. *Phys. Rev. A*, 7:159–167, 1973.

[37] J. Lachner, M. Christl, M. Döbeli, P.W. Kubik, M. Suter, and H.-A. Synal. ^{10}Be and ^{26}Al low-energy AMS using He-stripping and background suppression via an absorber. *Nucl. Instr. Meth. B*, 331:209–214, 2014.

[38] A. Wittkower and H. Betz. Equilibrium-charge-state distributions of energetic ions (Z>2) in gaseous and solid media. *Atomic Data*, 5:113–166, 1973.

[39] A. Ruiz-Gómez, E. Chamizo, J.M. López-Gutiérrez, M. García-León, A.M. Müller, and M. Christl. On the measurement of ^{10}Be on the 1 MV compact AMS system at the Centro Nacional de Aceleradores (Spain). *Nucl. Instr. Meth. B*, 268:733–735, 2010.

[40] S. Padilla. *Medidas de ^{10}Be y ^{26}Al en Espectrometría de Masas con Acelerador de Baja Energía en el Centro Nacional de Aceleradores*. PhD thesis, Universidad de Sevilla, 2015.

[41] C. Vivo Vilches. PhD thesis, Universidad de Sevilla, ongoing.

[42] M. Knudsen. *Ann. Phys.*, 28:75, 1909.

[43] A. Roth. *Vacuum Technology*. North Holland, 1982.

[44] M. Suter, M. Döbeli, M. Grajcar, A. Müller, M. Stocker, G. Sun, H.-A. Synal, and L. Wacker. Advances in particle identification in AMS at low energies. *Nucl. Instr. Meth. B*, 259:165–172, 2007.

[45] Cremat Inc. `http://cremat.com/`.

[46] A.M. Müller. Personal communication, 2015.

[47] M. Döbeli. Parametrisierung der gemessenen Straggling-Daten in SiN in "BohrKoordinaten". *LIP ETH Zürich*, 2006.

[48] G. Sun, M. Döbeli, A.M. Müller, M. Stocker, M. Suter, and L. Wacker. Energy loss and straggling of heavy ions in silicon nitride in the low MeV energy range. *Nucl. Instr. Meth. B*, 256:586–590, 2007.

[49] N. Bohr. *K. Dan. Vidensk. Selsk. Mat-fys. Medd.* 18, 1948.

[50] K. Nishiizumi. Preparation of ^{26}Al AMS standards. *Nucl. Instr. Meth. B*, 223–224:388–392, 2004.

[51] K.J.R. Rosman and P.D.P. Taylor. Report of the IUPAC Subcommittee for Isotopic Abundance Measurements. *Pure Appl. Chem.*, 71:1593–1607, 1999.

[52] C. Hohl, P. Gerisch, G. Korschinek, and E. Nolte. Medical applications of ^{26}Al. *Nucl. Instr. Meth. B*, 92:478–482, 1994.

[53] K.U. Miltenberger, A.M. Müller, M. Suter, H.-A. Synal, and C. Vockenhuber. Accelerator mass spectrometry of ^{26}Al at 6 MV using AlO^- ions and a gas-filled magnet. *Nucl. Instr. Meth. B*, 2017.

[54] A. Arazi, T. Faestermann, J.O. Fernández Niello, D. Frischke, K. Knie, G. Korschinek, H.J. Maier, E. Richter, G. Rugel, and A. Wallner. Magnesium suppression for ^{26}Al measurements using AlO^- ions. *Nucl. Instr. Meth. B*, 223–224:259–262, 2004.

[55] L.K. Fifield, S.G. Tims, L.G. Gladkis, and C.R. Morton. ^{26}Al measurements with ^{10}Be counting statistics. *Nucl. Instr. Meth. B*, 259:178–183, 2007.

[56] M. Martschini, J. Pitters, T. Moreau, P. Andersson, O. Forstner, D. Hanstorp, J. Lachner, Y. Liu, A. Priller, P. Steier, and R. Golser. Selective laser photodetachment of intense atomic and molecular negative ion beams with the ILIAS RFQ ion beam cooler. *Int. J. Mass Spectrom.*, 2017.

[57] J. Lachner. Personal communication, 2016.

[58] V.S. Nikolaev, I.S. Dmitriev, L.N. Fateeva, and Ya.A. Teplova. Equilibrium Distribution on Charges in a Beam of Ions of Light Elements. *Zh. Eksp. Teor. Fiz.*, 39:905, 1960.

[59] P. Hvelplund, E. Lægsgaard, and E Horsdal Pedersen. Equilibrium charge distributions of light ions in helium, measured with a position-sensitive open electron multiplier. *Nucl. Instr. Meth.*, 101:497–502, 1972.

[60] A.M. Müller, M. Christl, J. Lachner, H.-A. Synal, C. Vockenhuber, and C. Zanella. ^{26}Al measurements below 500 kV in charge state 2+. *Nucl. Instr. Meth. B*, 361:257–262, 2015.

[61] J. Klein, R. Middleton, and H. Tang. Modifications of an FN tantem for quantitative ^{10}Be measurement. *Nucl. Instr. Meth.*, 193:601–616, 1982.

[62] P.W. Kubik and M. Christl. ^{10}Be and ^{26}Al measurements at the Zurich 6 MV Tandem AMS facility. *Nucl. Instr. Meth. B*, 268:880–883, 2010.

[63] M. Ješkovský, P. Steier, A. Priller, R. Breier, P.P. Povinec, and R. Golser. Preliminary AMS measurements of ^{10}Be at the CENTA facility. *Nucl. Instr. Meth. B*, 361:139–142, 2015.

[64] L.K. Fifield, T.R. Ophel, G.L. Allan, J.R. Bird, and R.F. Davie. Accelerator mass spectrometry at the Australian National University's 14UD accelerator: experience and developments. *Nucl. Instr. Meth. B*, 52:233–237, 1990.

[65] A. Priller, T. Brandl, R. Golser, W. Kutschera, S. Puchegger, W. Rom, P. Steier, C. Vockenhuber, A. Wallner, and E. Wild. Extension of the measuring capabilities at VERA. *Nucl. Instr. Meth. B*, 172:100–106, 2000.

[66] S.R. Winkler, L.K. Fifield, S.G. Tims, and C.R. Morton. Improving the detection limit for ^{182}Hf. *Nucl. Instr. Meth. B*, 259:256–259, 2007.

[67] E. Schmidt. AMS detection of ^{10}Be with a SiN foil stack. Master's thesis, Universität Wien, 2013.

[68] M. Christl, C. Vockenhuber, P.W. Kubik, L. Wacker, J. Lachner, V. Alfimov, and H.-A. Synal. The ETH Zurich AMS facilities: Performance parameters and reference materials. *Nucl. Instr. Meth. B*, 294:29–38, 2013.

[69] Goodfellow. `http://goodfellow.com/`.

[70] Silson. `http://silson.com/`.

[71] J.F. Ziegler. SRIM. `http://www.srim.org/`.

[72] K. Nishiizumi, M. Imamura, M.W. Caffee, J.R. Southon, R.C. Finkel, and J. McAninch. Absolute calibration of ^{10}Be AMS standards. *Nucl. Instr. Meth. B*, 258:403–413, 2007.

[73] K. Nishiizumi, C.P. Kohl, E.M. Shoemaker, J.R. Arnold, D. Lal, J. Klein, D. Fink, and R. Middleton. In situ ^{10}Be-^{26}Al exposure ages at Meteor Crater, Arizona. *Geochim. Cosmochim. Acta*, 55:2699–2703, 1991.

[74] K. Nishiizumi, J.R. Kohl, C.P. andand Arnold, J. Klein, D. Fink, and R. Middleton. Cosmic ray produced ^{10}Be and ^{26}Al in Antarctic rocks: exposure and erosion history. *Earth Planet. Sci. Lett.*, 104:440–454, 1991.

[75] D. Bourlès, G.M. Raisbeck, and F Yiou. ^{10}Be and ^{9}Be in marine sediments and their potential for dating. *Geochim. Cosmochim. Acta*, 53:443–452, 1989.

[76] M. Segl, A. Mangini, G. Bonani, H.J. Hofmann, M. Nessi, M. Suter, W. Wöfli, G. Friedrich, W.L.. Plüger, A. Wiechowski, and J. Beer. ^{10}Be-dating of a manganese crust from Central North Pacific and implications for ocean palaeocirculation. *Nature*, 309:540–543, 1984.

[77] J.G. Ryan and C.H. Langmuir. Beryllium systematics in young volcanic rocks: implications for beryllium-10. *Geochim. Cosmochim. Acta*, 52:237–244, 1988.

[78] L. Brown. ^{10}Be: recent applications in earth sciences. *Phil. Trans. R. Soc. Lond.*, A323:75–86, 1987.

[79] G.M. Raisbeck, F. Yiou, M. Fruneau, J.M. Loiseaux, M. Lieuvin, J.C. Ravel, and C. Lorius. Cosmogenic ^{10}Be concentrations in antarctic ice during the past 30,000 years. *Nature*, 292:825–826, 1981.

[80] J. Beer, U. Siegenthaler, G. Bonani, R.C. Finkel, H. Oeschger, M. Suter, and W. Wölfi. Information on past solar activity and geomagnetism from ^{10}Be in the Camp Century ice core. *Nature*, 331:675–679, 1988.

[81] K. Nishiizumi, M. Imamura, C.P. Kohl, H. Nagai, K. Kobayashi, K. Yoshida, H. Yamashita, R.C. Reedy, M. Honda, and J.R. Arnold. ^{10}Be profiles in lunar surface rock 68815. *Proc. Lunar Planet. Sci. Conf. 18th*, 1988.

[82] X.-L Zhao, A.E. Litherland, J.P. Doupé, and W.E. Kieser. The potential for AMS analysis of ^{10}Be using BeF^-. *Nucl. Instr. Meth. B*, 223:199–204, 2004.

[83] M. Grajcar, M. Döbeli, P.W. Kubik, H.-A. Synal, L. Wacker, and M. Suter. New concepts of ^{10}Be AMS at low energies. *Nucl. Instr. Meth. B*, 259:173–177, 2007.

[84] G.M. Raisbeck, F. Yiou, D. Bourles, J. Lestringuez, and D. Deboffle. Measurement of ^{10}Be with a tandetron accelerator operating at 2 MV. *Nucl. Instr. Meth. B*, 5:175–178, 1984.

[85] M. Seiler. Personal communication, 2016.

[86] H.D. Betz. Heavy Ion Charge States. In *Condensed Matter*, volume 4 of *Applied Atomic Collision Physics*, pages 1–42. Academic Press, 1983.

[87] J. Lindhard and M. Scharff. Energy Dissipation by Ions in the keV Region. *Phys. Rev.*, 124:128, 1961.

[88] H. Weick. GICOSY. `https://web-docs.gsi.de/~weick/gicosy/`.

[89] D.P. Rodrigues Ferreira Maltez, A. Arazi, J. Fernández Niello, G. Martí, D. Abriola, O. Capurro, M. Cardona, D. Abriola, E. de Barbará, F. Gollan, D. Hojman, A. Pacheco, N. Samsolo, M. Togneri, and D. Villanueva. AMS measurement of ^{10}Be concentrations in marine sediments from Chile Trench at the TANDAR Laboratory. *Nucl. Instr. Meth. B*, 2017.

[90] F. Ajzenberg-Selove. Energy levels of light nuclei A = 11-12. *Nucl. Phys. A*, 1–158:506, 1990.

[91] J. Szabó, J. Csikai, and M. Várnagy. Low-energy cross sections for $^{10}B(p,\alpha)^7Be$. *Nucl. Phys. A*, 195:527–533, 1972.

[92] G.G. Bach and Livesey D.J. The cross section for the reaction $^{10}B(p,\alpha)^{7}Be$ at proton energies below 200 keV. *Philos. Mag.*, 46:824, 1955.

[93] W.E. Burcham and J.M. Freeman. The emission of short-range alpha particles from light elements under proton bombardment. II. Further observations on the reaction $^{10}B(p,\alpha)^{7}Be$. *Philos. Mag.*, 41:337, 1950.

[94] Amptek. `http://amptek.com/`.

[95] A.M. Müller. *Entwicklung von universellen AMS Anlagen bei tiefen Energien*. PhD thesis, ETH-Zürich, 2009.

[96] A.M. Müller, M. Döbeli, M. Suter, and H.-A. Synal. Performance of the ETH gas ionization chamber at low energy. *Nucl. Instr. Meth. B*, 287:94–102, 2012.